Integration and Optimisation of Sensitive Bolometric Detectors with Pulse-Tube Cryocoolers

Gareth Robert Walker

August, 2007

A thesis submitted to
the School of Physics and Astronomy,
Cardiff University
for the degree of
Doctor of Philosophy

ProQuest LLC
789 East Eisenhower Parkway
P.O. Box 1346
Ann Arbor, MI 48106-1346

Declaration

This work has not previously been accepted in substance for any degree and is not concurrently submitted in candidature for any degree.

Signed G Wylley (candidate) Date 20/8/07

Statement 1

This thesis is being submitted in partial fulfillment of the requirements for the degree of PhD.

Signed G Wylley (candidate) Date 20/8/07

Statement 2

This thesis is the result of my own independent work/investigation, except where otherwise stated. Other sources are acknowledged by explicit references.

Signed G Wylley (candidate) Date 20/8/07

Statement 3

I hereby give consent for my thesis, if accepted, to be available for photocopying and for inter-library loan, and for the title and summary to be made available to outside organisations.

Signed G Wylley (candidate) Date 20/8/07

"The most merciful thing in the world, I think, is the inability of the human mind to correlate all its contents. We live on a placid island of ignorance in the midst of black seas of infinity, and it was not meant that we should voyage far... But some day the piecing together of dissociated knowledge will open up such terrifying vistas of reality, and of our frightful position therein, that we shall either go mad from the revelation or flee from the light into the peace and safety of a new dark age."

H.P. Lovecraft, *The Call of Cthulhu*

Acknowledgements

First of all, thank you to PPARC and QMC Instruments for funding my studies and allowing me to live the youthful student life a little while longer. Thank you also to my supervisor 'A', Lucio Piccirillo and also Peter Ade and Ravinder Bhatia for taking me on at short notice and arranging the program of work in collaboration with ESTEC.

During my study I have directly benefitted from the wisdom, experience, and products of several people that I would like to thank. These include (apologies if I have missed anyone): Rob Tucker with his seemingly unlimited patience when assisting me with the construction of electronics, as well as solving endless problems and answering endless questions; Rashmi Sudiwala and Phil Mauskopf with their assistance on how to best use the said electronics; Simon Melhuish and his help with all things TINI; Angiola Orlando for providing a bolometer for me to work with; Simon Chase for building me a fridge; Jens Höhne for providing technical support for the VeriCold PTC; Kate Isaak for becoming supervisor 'B' at the eleventh hour, getting my writing-up on track, and improving my English. Okay, it's still not perfect...

Finally, thank you to my parents for not pressuring me to finish and get a job *too* much. This is for them.

Abstract

The integration of 300 mK semiconductor bolometers and 4 K hot-electron bolometers with commercial pulse tube cryocooler (PTC) systems has been investigated. The process also involved the integration of a two-stage ^{4}He-^{3}He adsorption refrigerator with the PTC to produce a cryogen free sub-Kelvin system. Thermometry electronics with an onboard computer and an internet interface have been developed that allow for remote and/or automatic operation.

Methods to reduce excess noise seen in the 300 mK bolometer have been investigated to demonstrate the possibility of using high sensitivity bolometric detectors in this system for astrophysics and Earth observation instruments. In order to minimise the microphonic induced noise and thermal fluctuations from the pulse tube operation an AC biasing circuit was used. The origin of excess noise components in the bolometer readout have been identified and quantified as a function of both mechanical and electrical configurations of the cold components. With the optimum configuration thermal fluctuation noise, rather than microphonic induced noise dominates, reducing the bolometer sensitivity by approximately two times compared to the same device operated in a liquid helium cooled cryostat. Clearly the performance could be improved by increasing the thermal isolation of the sorption refrigerator from the pulse tube temperature oscillations.

The hot-electron bolometer behaved nominally up to 6 kHz when operated in the cryogen free cryostat. Dynamic audio frequency noise deteriorated the detector's performance above 6 kHz and has been attributed to the movement of the helium gas through the PTC's valves and orifices during its thermodynamic cycle. Restrictions of the signal analyser mean that it is unclear whether this microphonic noise is present above 1 MHz.

CONTENTS

List of Figures xvi

List of Tables xvii

Nomenclature xix

1 Introductory Background 1

1.1 The Need For Low Temperatures 1

1.2 The Need For Closed-Cycle Cryocoolers 2

1.3 Astronomy At Sub-Kelvin Temperatures 4

1.3.1 A Very Concise History Of The CMB 4

1.4 Theoretical Operation Of A Pulse Tube Cryocooler 5

1.4.1 The Carnot Cycle 5

1.4.2 Regenerative Cycles 7

1.4.3 The Stirling Cycle 9

1.4.4 The Orifice Pulse Tube Cooler 11

1.4.5 Summary of Regenerative Cryocoolers 16

1.5 Methods For Obtaining Sub-Kelvin Temperatures 17

1.5.1 Helium-3 Evaporation 18

1.5.2 Adiabatic Demagnetisation Refrigeration 19

1.5.3 Dilution Refrigeration 20

1.5.4 Summary of Sub-Kelvin Refrigerators 21

1.6 Bolometric Detectors And Potential Noise Sources 21

1.6.1 Bolometers In General 22

1.6.2 Bolometer Responsivity 24

1.6.3 Noise Contributions 25
1.6.4 NTD-Ge Bolometers 26
1.6.5 InSb Hot Electron Bolometers 29
1.6.6 TES Bolometers 30
1.7 Scope Of This Thesis 30

2 Previous Investigations... **32**
2.1 POLATRON 33
2.1.1 POLATRON Cryogenics 33
2.1.2 POLATRON Detectors And Readout 33
2.1.3 POLATRON Feasibility Testing 34
2.1.4 POLATRON Conclusions 35
2.2 General Study 36
2.2.1 Photoconductor Testing 36
2.2.2 Bolometer Testing 38
2.2.3 General Study Conclusions 47
2.3 Previous Investigation Conclusions 48

3 Experimental Setup **49**
3.1 Cryogenics 49
3.1.1 Pulse Tube Cryocoolers 50
3.1.2 Helium-3 Sorption Refrigerator 52
3.1.3 Overall Performance 55
3.2 Electronics 59
3.2.1 Cryogenic Control and Thermometry 60
3.2.2 NTD-Ge Bolometer Readout 62
3.2.3 Grounding 67

4 300 mK NTD-Ge Bolometer Tests **69**
4.1 Bolometer Description 69
4.2 Baseline Characterisation 71
4.3 Characterisation Using PTC System 74
4.3.1 Modelled and Measured DC Load Curves 76

4.3.2 AC Load Curves 76
4.3.3 Electrical Time Constant 78
4.3.4 Baseline PTC Noise Measurement 82
4.4 Dummy Resistor Testing 85
4.4.1 0.3 K Resistor Chain 85
4.4.2 3 K Resistor Chain At JFET Input 87
4.5 High Impedance Wiring Configurations 89
4.6 Reducing Thermal Noise Using a Passive Thermal Filter 93
4.6.1 Identifying the Thermal Noise 93
4.6.2 Implementing the Thermal Filter 97
4.7 Electrical Isolation 100
4.8 High Frequency Microphonics 101
4.9 300 mK NTD-Ge Bolometer Conclusions 102

5 3–4 K InSb Hot Electron Bolometer Tests **104**
5.1 Wet Cryostat Baseline Testing 104
5.2 Cryomech PTC Testing 105
5.3 VeriCold PTC Testing 106
5.3.1 Thermal Buffer Tests 108
5.4 InSb Hot Electron Bolometer Conclusions 109

6 Thermal Fluctuation Measurements **112**
6.1 PTC-Sorption Refrigerator Coupling Model 113
6.2 PTC With 2-Stage Sorption Refrigerator 114
6.2.1 PTC Cold-Head Measurements 114
6.2.2 Sorption Cold-Head Measurements 115
6.2.3 Comparison to Model 116
6.3 CLOVER Prototype Cryostat With 3-Stage Sorption Refrigerator . . . 116
6.3.1 PTC Cold-Head Measurements 118
6.3.2 Sorption Cold Head Measurements 118
6.3.3 Comparison to Model 120
6.4 Thermal Fluctuations Conclusions 120

7 Discussion And Conclusions **122**

7.1 Summary Of Results 122

7.2 Implications 124

7.3 Future Work 125

Appendices **127**

A Thermodynamics **128**

A.1 Ideal Stirling and Ericsson Cycles 128

A.2 Dependence of Cooling Power on Phase Angle 130

B Bolometric Detectors **132**

B.1 Basic Model for the Responsivity of a Semiconductor Bolometer 132

B.1.1 Absorbed Power Responsivity, S_A 132

B.1.2 Electrical Responsivity, S_E 134

B.2 Dynamic Bolometer Model 135

C Example TINI Code **144**

D Circuit Diagrams **150**

Bibliography **159**

List of Figures

1.1 Carnot Thermodynamic Cycle. 6

1.2 Pressure-Volume diagrams for the Stirling and Ericsson cycles. 8

1.3 Carnot, Stirling, and Ericsson cycle Temperature-Entropy diagram . . . 9

1.4 Stirling piston motions 10

1.5 Schematic of an orifice pulse tube cooler. 12

1.6 Carnot, Stirling, and Pulse Tube cycle energy exchange schematics. . . 13

1.7 Enthalpy flow within a pulse tube. 14

1.8 Bolometer Schematic 23

1.9 Basic current biased bolometer readout. 28

1.10 Current biased differential bolometer readout using a matched JFET pair. 28

2.1 *Polatron*: Bolometer noise with cooler turned on 35

2.2 Bhatia: Photoconductor measurements 37

2.3 Bhatia: 350 mK Bolometer noise 39

2.4 Bhatia: 350 mK Resistor noise 41

2.5 Bhatia: 350 mK optically loaded bolometer 42

2.6 Bhatia: *SCUBA* detector response in ADR system 43

2.7 Bhatia: Optically loaded 100mK bolometer 44

2.8 Bhatia: Blanked 100 mK prototype bolometer in ADR system 45

2.9 Bhatia: Bolometer, thermistor and resistor in dilution system 46

3.1 Cryomech PT405 thermal load diagram. 52

3.2 VeriCold PRK4 thermal load diagram. 53

3.3 Two-stage sorption refrigerator. 53

3.4 Sorption refrigerator cooling power. 54

3.5 Cryomech PTC with sorption refrigerator mounted. 55

3.6 Precooling of the PTC-Sorption refrigerator system. 56

3.7 Sorption refrigeration cycle. 57

3.8 Sorption refrigeration cycle from 'cold'. 58

3.9 Cryogenic performance under inclination. 59

3.10 Schematic of the cryostat data acquisition system. 60

3.11 Cryogenic Control and Thermometry unit front panel. 60

3.12 Stages of NTD-Ge bolometric detector readout. 63

3.13 Cryostat mounted bolometer readout box. Contains the bias generator, bias monitors, JFET power supplies, and the room temperature preamplifiers. 64

3.14 Input shorted warm amplifier and LIA noise. 65

3.15 Cold electronics for NTD-Ge bolometer readout. 66

3.16 JFET module 67

3.17 Grounding schematic for the PTC cryostat. 68

4.1 The 300 mK NTD-Ge bolometer 70

4.2 NTD-Ge bolometer V-I characteristics 'wet' cryostat 71

4.3 NTD-Ge bolometer's linear resistance-temperature plot 72

4.4 NTD-Ge bolometer resistance versus heat sink temperature curve . . . 73

4.5 Fitted NTD-Ge load curves 'wet' cryostat 73

4.6 Average thermal conductance against heat sink temperature 74

4.7 NTD-Ge bolometer optical time constants measured in the 'wet' cryostat [1]. 75

4.8 NTD-Ge bolometer DC noise response in a 'wet' cryostat [1]. 75

4.9 Load curves for the NTD-Ge bolometer with data taken in the PTC system and fitted with the thermal model characterised in the 'wet' cryostat for a range of temperatures. 77

4.10 AC and DC load curve comparison. 78

4.11 NTD-Ge bolometer's AC and DC responsivity comparison and NEP. . 79

4.12 Electrical measurement of the NTD-Ge bolometer response time. 80

4.13 NTD-Ge bolometer response to a square wave bias voltage fitted with the dynamic bolometer model. 81

4.14 Path of the NTD-Ge bolometer's signal on its load curve in response to a square wave bias, at a T_S of 294 mK. 82

4.15 Initial NTD-Ge bolometer noise for DC biasing at 300 mK with the PTC turned on and off. 83

4.16 Initial NTD-Ge bolometer noise for AC biasing (80 Hz) at 300 mK with the PTC turned on and off. 84

4.17 Initial noise spectra from the 15 MΩ fixed resistor at 300 mK, DC biased. 86

4.18 Initial noise spectra from the 15 MΩ fixed resistor at 300 mK, AC biased at 80 Hz. 86

4.19 PTC on/off noise spectra from the 15 MΩ fixed resistor at 300 mK, AC biased at 142 Hz. 87

4.20 3 K, 1.5 MΩ resistor noise spectra showing the limited dynamic range of the signal analyser. 88

4.21 PTC on/off noise spectra from the 1.5 MΩ fixed resistor at 3 K, AC biased at 135 Hz. 89

4.22 Single cryogenic coaxial cable setup 90

4.23 NTD-Ge bolometer response using a single coaxial cable. 90

4.24 0.3 K. 15 MΩ resistor response using a single coaxial cable. 91

4.25 NTD-Ge bolometer response using twin coaxial cables. 92

4.26 0.3 K, 15 MΩ resistor response using an aluminised Mylar shielded twisted pair of Constantan wires. 92

4.27 Improved 0.3 K, 15 MΩ, resistor response using an aluminised Mylar shielded twisted pair of Constantan wires. 93

4.28 NTD-Ge bolometer response using an aluminised Mylar shielded twisted pair of Constantan wires. 94

4.29 0.3 K, 15 MΩ resistor response using twin coaxial cables. 94

4.30 NTD-Ge bolometer's thermal noise peaks dependence on PTC operating frequency. 95

4.31 Comparison of the NTD-Ge bolometer's DC response and LIA output. 96

4.32 NTD-Ge bolometer response with and without the 2 × 25 μm Mylar thermal buffer. 98

4.33 Best NTD-Ge bolometer response with the 2 × 25 μm Mylar thermal buffer. 99

4.34 NTD-Ge bolometer response with the 4 × 25 μm Mylar thermal buffer. 99

4.35 NTD-Ge bolometer response with the 185 μm Mylar thermal buffer plus electrical isolation. 100

4.36 Snap shots of the 0.3 K, 15 MΩ resistor noise spectra at high frequencies with the PTC turned on. 101

4.37 Snap shots of the NTD-Ge bolometer noise spectra at high frequencies with the PTC turned on. 102

5.1 The InSb hot electron bolometer 'toaster' element mounted on a quartz substrate. 105

5.2 HEB response while mounted in the Cryomech PTC. 106

5.3 HEB response in the VeriCold PTC up to 6 kHz. 107

5.4 HEB response in the VeriCold PTC up to 12 kHz. 107

5.5 HEB response in the VeriCold PTC up to 100 kHz. 108

5.6 Average of 100 HEB noise spectra compared to a single trace taken in the 'quiet' gap between PTC pulses. 109

5.7 HEB response in the VeriCold PTC with and without the 185 μm Mylar thermal buffer. 110

5.8 Relative InSb signal — buffered/unbuffered. 110

6.1 PTC second stage temperature fluctuations. 114

6.2 2-stage sorption refrigerator cold head temperature fluctuations. 115

6.3 The measured temperature fluctuations compared to the theoretical model in the original test bed. 117

6.4 *Clover* prototype cryostat's flexible thermal links and base plate support structure, plus the 3-stage sorption refrigerator. 118

6.5 Cryomech PTC second stage temperature fluctuations in *Clover* prototype cryostat. 119

6.6 3-stage sorption refrigerator cold head temperature fluctuations in *Clover* prototype cryostat. 119

6.7 The measured temperature fluctuations compared to the theoretical model in the *Clover* test bed. 120

List of Tables

1.1 Maximum COP for 300 K Ambient Temperature. 7

1.2 Summary of regenerative mechanical cooler methods. 17

1.3 Summary of sub-Kelvin cooling methods. 21

1.4 Summary of bolometric detectors. 22

2.1 Prototype 100 mK spider-web bolometer optically loaded NEP 45

4.1 Table showing the voltage noise components for the bolometer operating at 360 and 300 mK 76

Nomenclature and Abbreviations

A	Cross-sectional area of the pulse tube
ADR	Adiabatic Demagnetisation Refrigerator
C	Heat capacity
c_p	Specific heat capacity at constant pressure
C_p	Molar (specific) heat capacity at constant pressure
CMB	Cosmic Microwave Background
COP	Coefficient Of Performance
CPU	Central Processing Unit
EMI	Electromagnetic Interference
ESA	European Space Agency
FTS	Fourier Transform Spectrometer
G	Dynamic conductance
$\bar{G}$	Average (static) thermal conductance
$\bar{G}_S$	Average thermal conductance when $T_B = T_S$
G-M	Gifford-MacMahon (cryocooler)
GRT	Germanium Resistance Thermometer
$\langle \dot{H} \rangle$	Net enthalpy flow from cold to hot end of the pulse tube
$\langle \dot{H}_r \rangle$	Net enthalpy flow through the regenerator
^{3}He	Helium-3 isotope
^{4}He	Helium-4 isotope
HEB	Hot-Electron Bolometer
I	Current through the detector
I^{2}C	Inter-Integrated Circuit
JFET	Junction Field Effect Transistor
J-T	Joule-Thompson
k_B	Boltzmann constant ($= 1.38 \times 10^{-23}$ [J K^{-1}])
LCD	Liquid Crystal Display
LIA	Lock-In Amplifier
$\dot{m}$	Mass flow rate
$\dot{m}_0$	Mass flow rate amplitude
m_a	Atomic mass
n	Parameter for the $R(T)$ curve for an NTD-Ge chip
NEP	Noise Equivalent Power
NTD-Ge	Neutron Transmutation Doped Germanium
P	*Pulse Tubes* — Pressure
	Bolometers — Electrical power dissipated in the detector
ΔP	Pressure oscillation amplitude
PCB	Printed Circuit Board
PID	Proportional-Integral-Derivative
PTC	Pulse Tube Cryocooler
PTR	Pulse Tube Refrigerator
Q	Radiation power incident on a detector
Q_a	Heat rejected to the ambient surroundings

Q_c	Heat lift from the cold source
$\langle \dot{Q}_c \rangle$	Net rate of heat lift from the cold source (cooling power)
Q_H	Heat rejected at the hot end of a pulse tube
R	*Pulse Tubes* — Gas constant (= 8.31 [J K^{-1} mol^{-1}])
	Bolometers — Resistance
R_L	Load resistance
R_*	Parameter for the $R(T)$ curve for an NTD-Ge chip
RAL	Rutherford Appleton Laboratory
RF	Radio Frequency
RTD	Resistance Temperature Detector
S	*Pulse Tubes* — Entropy
	Bolometers — Optical responsivity
S_A	Absorbed power responsivity
S_E	Electrical responsivity
Si_3N_4	Silicon-nitride
SQUID	Superconducting Quantum Interference Device
STP	Standard Temperature and Pressure
SZ	Sunyaev-Zel'Dovich
T	Temperature
t	Time
T_a	Ambient temperature
T_B	Bolometer temperature
T_c	Cold temperature
T_g	Parameter for the $R(T)$ curve for an NTD-Ge chip
T_S	Bolometer heat sink temperature
TES	(superconductor) Transition Edge Sensor
TINI	Tiny InterNet Interfaces
u	Working fluid velocity
u_0	Working fluid velocity amplitude
V	Voltage drop across the detector
V_n	Voltage noise
W	*Pulse Tubes* — Net mechanical work
	Bolometers — Total power dissipated in the detector
W_a	Work done by ambient compression piston
W_c	Work done by cold expansion piston
Z	Dynamic impedance
α	Temperature coefficient
β	Material parameter describing the thermal conductivity's variation with temperature
η	Absorptivity
ρ	Density
τ	*Pulse Tubes* — Time period for a thermodynamic cycle
	Bolometers — Physical time constant
ϕ	Phase angle between the mass flow and the pressure oscillations
ω_s	Optical modulation frequency

Chapter 1

Introductory Background

The subject of this thesis is the study of the integration of bolometric detectors with pulse tube cryocooler systems for the purposes of astrophysical instrumentation. There are many astrophysical sources that are too cool in temperature for them to be visible to the naked eye, or enshrouded in gas and dust clouds that cannot be penetrated by visible wavelengths. Infrared, submillimetre, and millimetre wavelengths must be used to observe these sources instead. The detectors used for these wavelengths usually require cryogenic cooling in order to meet the required sensitivities to detect the weak astrophysical sources, and in the past this has been achieved using liquid cryogens. This chapter looks at the motivation behind wanting to use mechanical coolers as part of astrophysical experiments, the advantages and disadvantages of doing so, their basic operation, and the bolometric detectors used in such experiments.

Although the project is funded for astrophysical purposes, it does have wider applications since many detectors of different types of system require cryogenic cooling. Electron microscopes, spectrometers for Earth observations [2] and night vision units [3] are but a few. The detectors themselves may differ but the principles of minimising the induced noise remain the same. First, the reasons for needing low temperatures at all must be considered.

1.1 The Need For Low Temperatures

There are fundamentally two reasons for needing and using low temperatures to operate detectors covering the electromagnetic spectrum from infrared to millimetre wave-

lengths. The first is to increase sensitivity, and the second is to make use of superconducting technologies. Arguably the second is just a means to achieving the first however. Although there are now superconducting materials and even Superconducting Quantum Interference Devices[1] (SQUIDs) that can operate at liquid nitrogen temperatures (77 K), the very low temperature materials and devices still remain the most sensitive.

Sensitivity increases with lower temperatures because many sources of noise follow the fluctuation dissipation theorem, which describes macroscopic behaviour as a result of microscopic fluctuations, and scale with the factor k_BT, where k_B is the Boltzmann constant and T is temperature. The classic example is the electrical noise first observed by Johnson [4] for which Nyquist first deduced the theorem [5] (see subsection 1.6.3 for details and other examples). As such, it is desirable to operate detectors on instruments at several Kelvin or even a fraction of a Kelvin.

Superconducting materials used in the construction of bolometric detectors include, but are not limited to, niobium for electrical leads, and indium for solder joints. In bulk, niobium has a superconducting transition temperature of about 9 K, this decreases for thin films with thicknesses below 1000 Å, while for indium it is 3.4 K, also decreasing for thin films. It is apparent then, that to make use of their superconducting properties, liquid helium temperatures are required for niobium while even lower temperatures are required for indium in its raw form.

1.2 The Need For Closed-Cycle Cryocoolers

Until fairly recently the only way to cool a detection system down to 4.2 K was to use a liquid helium cryostat, usually with an additional liquid nitrogen stage for precooling. Mechanical coolers were considered too complex and required cold moving parts that reduce reliability. This is especially true for space missions where reliability is of even more importance due to the general expense of such missions and the difficulties of servicing instruments in space. Mechanical coolers also introduced additional noise to the system because of their vibration. Experimentalists have therefore had to suffer with liquid cryogens, their expenses and hazards.

Pulse tube cryocoolers (PTCs) represent a key technology for achieving temperatures down to about 4 K; the temperature usually achieved by using liquid helium at at-

[1] Sensitive magnetometers.

mospheric pressure. A number of instruments are proposing to make use of these coolers. The key factors which distinguish the pulse tube cooler from the more commonly-used Gifford-MacMahon (G-M) or Stirling cryocoolers, is that they have no cold moving parts and are therefore more reliable, whilst generating less vibration and electromagnetic interference (EMI). It is also beneficial to use closed-cycle coolers in general because liquid Helium is a limited natural resource. Unfortunately there is little field experience of using pulse tubes with bolometers and the deleterious effects of cryocooler vibration, thermal stability and EMI on sensitive bolometric detectors are not fully understood. While higher temperature (55 K) pulse tube cryocoolers (referred to in this work as pulse tube refrigerators, PTRs) operating at a higher thermodynamic cycle frequency (45 Hz) are currently being flown on satellites, on the *AIRS* instrument [6] for example, it is the lower frequency, lower temperature variety that are necessary for adequate precooling of sensitive bolometric detectors to meet scientific objectives such as measurements of the cosmic microwave background (CMB). This work serves as a preliminary investigation into the system level sensitivity problems experienced with a bolometric detector cooled via a combination of ^{3}He adsorption refrigeration and commercial PT coolers.

There are associated problems with using PTCs, however. Currently, pulse tubes do not provide as much cooling power at 4.2 K as a conventional liquid helium cryostat. However, the performance of PTCs is continuously being improved upon and the gap is closing. More of a concern is the additional microphonic noise that they introduce to the electronic readout of the system. Vibration is minimal since there are no moving parts at low temperatures, however some motion is produced by the pressure oscillations in the pulse tube. As well as increasing the noise of the detector directly, this motion also induces EMF's within the wiring. This can be minimised by using twisted pairs of wires in order to cancel out the motion of the wires relative to one another. Temperature stability is also a concern when compared to liquid helium; however, this is also continuously being improved upon.

Closed-cycle systems also make cryogenic temperatures more accessible to the wider community since they require less experience to operate than handling liquid cryogens. Integration of a sub-Kelvin refrigerator, and provision of automated electronics, creates a truly 'turn-key' operated system that can be utilised across many fields from low temperature physics to magnetic resonance imaging systems used for medical and psychological applications.

1.3 Astronomy At Sub-Kelvin Temperatures

As previously mentioned, there are many astrophysical sources that are too cool for them to be visible to the naked eye. Instead, the peak of their emission is at longer wavelengths as described by Wien's displacement law; $\lambda_{max}T \approx 2.90 \times 10^{-3}$ [Km]. For example: The peak of the black body spectrum of the cosmic microwave background (CMB), which has a mean temperature of approximately 3 K, is at a wavelength of approximately 1 mm; Cold interstellar medium (molecular clouds) at a few tens of Kelvin emits at 100–200 μm; The UV radiation from newly formed stars is absorbed and re-emitted at infrared and longer wavelengths by surrounding dust and gas. The infrared, sub-millimetre, and millimetre detectors needed to perform observations of these cool sources often require cold shielding from their warm environments to cut down on background thermal radiation. This makes the source object of interest more visible. The strength of the source determines just how cold the protection needs to be. Continuing the previous examples, observations of star forming regions can be done with detectors operating at liquid helium temperatures (4.2 K) [7], whereas to detect the comparatively weak anisotropies of the CMB the detectors need to be at 350 mK or below. The advent of CMB polarisation experiments further requires these extreme low temperatures.

1.3.1 A Very Concise History Of The CMB

Originally discovered by accident, the CMB now provides us with the earliest possible picture of the Universe in electro-magnetic radiation. The photons making up the CMB originate at the surface of last scattering, the time of recombination of protons and electrons that left photons free to travel the length of the visible Universe, and as a result have an imprint of the distribution of matter at that time. Astronomers wish to study it then to find out about the formation, structure and evolution of the Universe.

Current cosmological models require the use of several parameters such as the relative abundances of different types of matter and the Hubble 'Constant'. This sort of information can only be gained by looking closer at the CMB since overall it is very uniform, because of the homogeneous nature of the Universe at the time of Recombination, and tells us not much more than how long ago it formed. So over the years the temperature anisotropies have been mapped out with increasing resolution, from which power spectra are produced telling us how much information there is at each angular

scale. The positions and sizes of peaks in these spectra are what hold the information of the cosmological parameters.

Anisotropies of the CMB's temperature can only reveal so much however, and there are many parameters. To break down the inevitable degeneracy in the various cosmological models we need to observe with more precision and in more detail. Measuring the polarisation of the anisotropies will further constrain current parameters and give new information altogether. This involves detecting even smaller temperature variations only achievable with advances in bolometer technology and giving greater need for low temperature surroundings. In order to become sensitive enough to detect these micro-Kelvin temperature fluctuations we need to cool the detectors to sub-Kelvin temperatures; this increases their sensitivity by several orders of magnitude. Conventionally, to keep the detectors at these low temperatures a ^{3}He sorption refrigerator [8] (for 300 mK) or ADR (for 100 mK) is operated from a liquid helium bath.

1.4 Theoretical Operation Of A Pulse Tube Cryocooler

Before presenting an overview of how a pulse tube cryocooler works we must first consider mechanical coolers in general. In particularly I will be focusing on those with *regenerative* thermodynamic cycles since it is these that are most efficient when used on the sorts of scales that we are concerned with. It is also the family that PTCs belong to. While cryogenic liquefaction plants use cryocoolers based on Linde-Hampson or Brayton cycles, these *recuperative* cycles, using counter-flow heat exchangers, become very inefficient when miniaturised.

1.4.1 The Carnot Cycle

I will start by looking at the most efficient of cycles, the Carnot cycle, and how this needs to be modified to make something more practical for use. The Carnot cycle consists of an isothermal compression and expansion separated by an adiabatic compression and expansion. The cycle is shown schematically in Figure 1.1 on a Pressure-Volume diagram (Figure 1.1(a)) and a Temperature-Entropy diagram (Figure 1.1(b)), where the lines 1–2 and 3–4 depict the isotherms, and 2–3 and 4–1 depict the adiabatic stages of the cycle, operating between an ambient temperature, T_a, and a cold temperature,

T_c.

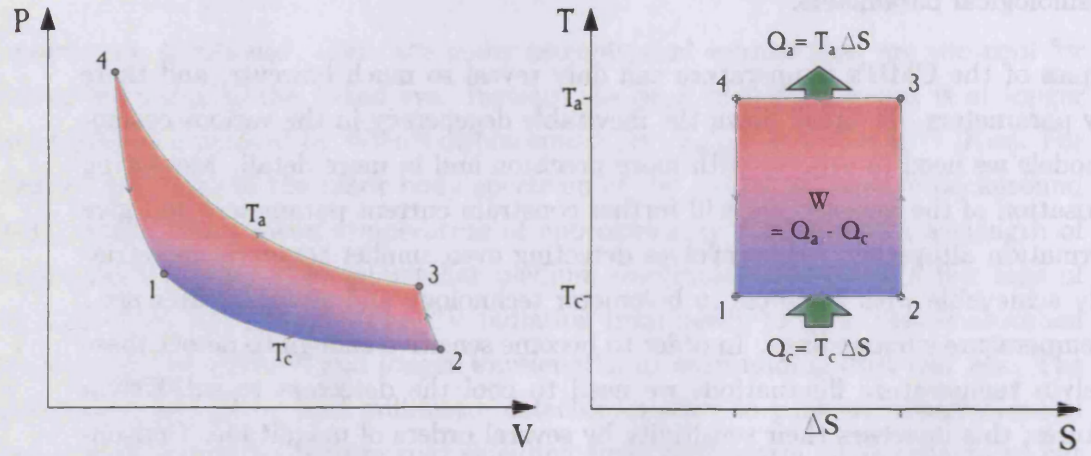

(a) Pressure - Volume (b) Temperature - Entropy

FIGURE 1.1: Carnot Thermodynamic Cycle. The enclosed shaded area indicates the net work done during the cycle.

During the isothermal expansion 1–2, an amount of heat, Q_c, is taken into the working fluid from the cold source and is represented by the area beneath the line in Figure 1.1(b). This is true for reversible processes where $q = \int TdS$. The working fluid undergoes an adiabatic compression, 2–3, bringing it up to ambient temperature. The isothermal compression 3–4 results in an amount of heat, Q_a, being rejected to the ambient surroundings. Again, this is represented by the area beneath the 3–4 line in Figure 1.1(b), and you have a pictorial representation of the relationship $W = Q_a - Q_c$, *ie.* the mechanical work input is the area enclosed by the cycle. Finally, the adiabatic expansion 4–1 takes the working fluid back to its starting state.

Because the heat transfer occurs isothermally and reversibly, and the compression and expansion stages are adiabatic and also reversible (isentropic), the efficiency of the cycle can be parametrised using only the two extreme temperatures involved. The coefficient of performance (COP) is defined as the ratio of the heat extracted from the cold source, Q_c, to the work provided to operate the system, W (In other words the useful cooling power divided by the input power). In this case it is the maximum possible COP because we are considering the Carnot cycle.

$$COP = \frac{Q_c}{W} \tag{1.1}$$

Using the relation $W = Q_a - Q_c$ and substituting in for Q_a and Q_c we get

$$\begin{aligned} COP &= \frac{T_c \Delta S}{T_a \Delta S - T_c \Delta S} \\ &= \frac{T_c}{T_a - T_c} \end{aligned} \tag{1.2}$$

Assuming an ambient temperature of 300 K, the COP can be calculated for a range of target low temperatures, as indicated in Table 1.1. This table shows the maximum COP for several approximate benchmark target low temperatures — Liquid nitrogen, liquid helium, and a pumped liquid ^{3}He bath.

Temperature (K)	77	4	0.3
COP_{max}	0.345	0.014	0.001

TABLE 1.1: Maximum COP for 300 K Ambient Temperature.

Problems arise in practice because the high pressure required (at point 4 in Figure 1.1), or more specifically the pressure ratio needed, cannot be achieved with present day technology. The Stirling and Ericsson cycles address this issue by shifting points 3 and 4 in Figure 1.1 to higher entropy and lower pressure.

1.4.2 REGENERATIVE CYCLES

For the Stirling and Ericsson cycles to reduce the maximum required pressure, the adiabatic compression and expansion stages are replaced with constant volume (Stirling) or constant pressure (Ericsson) processes, as illustrated in Figure 1.2. The resulting temperature-entropy diagrams are compared to the Carnot cycle in Figure 1.3.

Assuming ideal reversible isochoric and isobaric processes, the resulting enclosed area, and therefore work input, is the same as that for the Carnot cycle, $W = W' = W''$. Hence the maximum COP is retained. See section A.1 for details on how the area remains the same when considering reversible processes. However, in both cases you now have heat transfer at a variable temperature, given by the areas beneath 2–3′(′) and 4′(′)–1 in Figure 1.3. As explained in section A.1 and indicated by the simplified Figure 1.3, in the ideal case each process is equal and opposite to the other, and so there is no net contribution to the heat entering or leaving the system from these two phases — the energy is simply stored somewhere temporarily. The device employed to achieve this temporary storage of energy is called a *regenerator*.

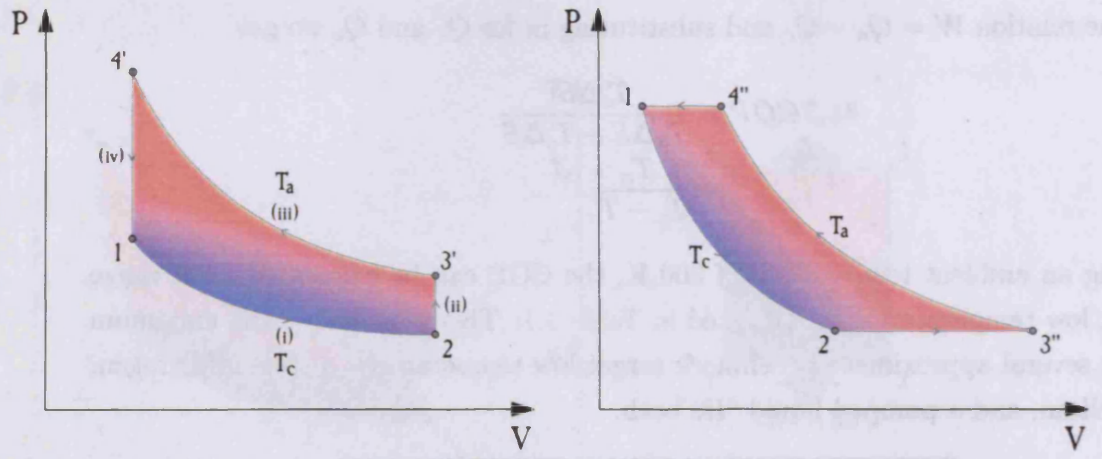

(a) Stirling Cycle. The lower case roman numbers refer to the piston movements in Figure 1.4.

(b) Ericsson Cycle

FIGURE 1.2: Pressure-Volume diagrams for the Stirling and Ericsson thermodynamic cycles. The enclosed shaded area indicates the net work done during the cycle.

In the design of mechanical cryocoolers, the regenerator essentially becomes both a heat exchanger and energy bank, and is a crucial component of the system. The efficiency of the cooler is largely determined by the regenerator's performance. Ideally it has:

- Large heat capacity,
- Low thermal conductivity,
- Small internal volume,
- Low flow impedance,
- Large internal surface area.

They are typically made up from a composite matrix of metal alloys either as a series of meshes, or spherules packed together. Often the alloys are made up from rare-earth metals whose magnetism helps provide the large heat capacity, and new, more efficient materials are always being researched. Low thermal conductivity is necessary because the regenerator often provides the main structural link between the hot and cold ends of the cooler. The small internal volume and low flow impedance minimise the pressure drop across the regenerator, which reduces the efficiency of the cooler. The large surface area, together with the large heat capacity, increase the efficiency of the heat transfer to and from the working fluid. The large heat capacity also ensures that the temperature gradient along the regenerator is approximately constant. Note

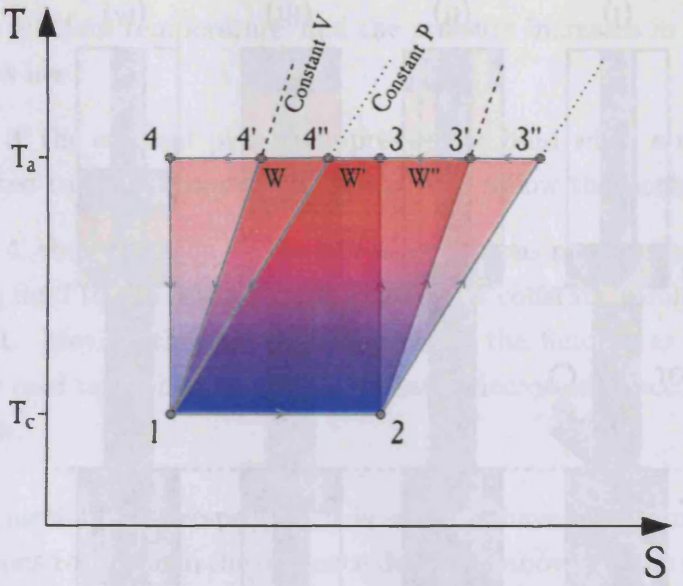

FIGURE 1.3: Temperature-Entropy diagram comparing the Carnot (1–2–3–4), Stirling (1–2–3′–4′) and Ericsson (1–2–3″–4″) thermodynamic cycles. The enclosed shaded area indicates the net work done during the cycle.

that the requirements for a minimal pressure drop and an efficient heat transfer conflict with each other when designing a regenerator. More details of the materials and design principals of regenerators can be found in the collection edited by Weisend II [9].

The Stirling cycle is utilised by Stirling cryocoolers by using a pressure oscillator to drive the compression. Frequencies for the oscillation tend to be around 40–50 Hz. The Ericsson cycle meanwhile, is utilised by Gifford-MacMahon (G-M) cryocoolers using a compressor and check valves to alternately connect the high and low pressure sides to the system. They tend to operate at lower frequencies than Stirling type coolers, up to about 10 Hz. PTCs fit somewhere in between the two cycles depending on the driving method. The thermodynamic cycle of higher temperature, higher frequency PTCs driven by a pressure oscillator, resembles that of the Stirling cycle. Low temperature, low frequency PTCs driven by a compressor and rotary valve combination have cycles resembling the Ericsson cycle.

1.4.3 THE STIRLING CYCLE

The Stirling cycle is described here in more detail to provide an analogy for the pulse tube in the following subsection 1.4.4. The Stirling cycle was first developed and patented by Rev. Robert Stirling in 1816 as a replacement for the hazardous steam engines of the time. It never became popular commercially as an engine, despite being

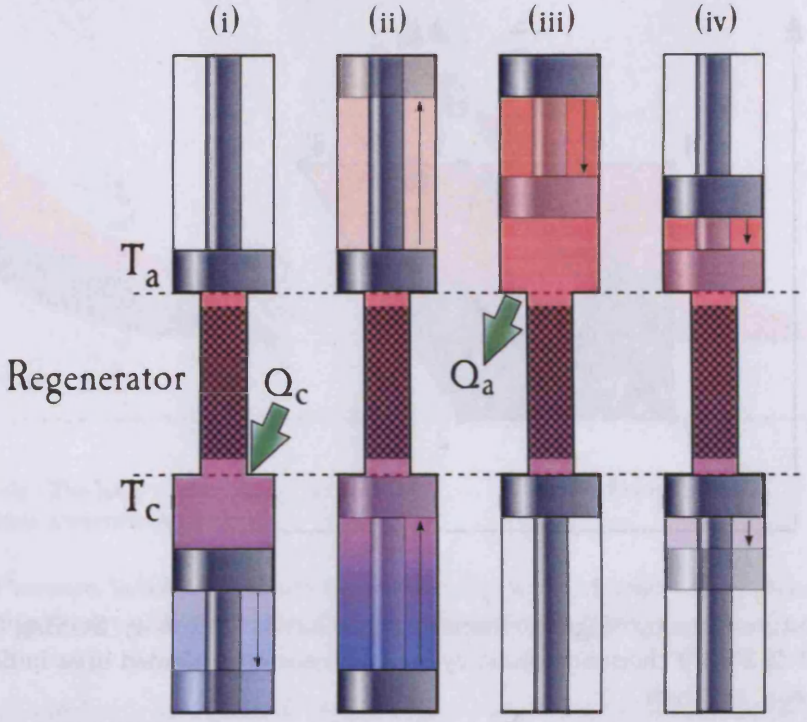

FIGURE 1.4: Stirling piston motions to produce the ideal Stirling cycle shown in 1.2(a) and Figure 1.3.

able to operate from any source of heat, and was dominated by the internal combustion engine after the steam age. Instead, it was tried out in reverse as the basis for some of the first mechanical coolers. However, later Joule-Thompson expansion [10] became the favoured method for attaining low temperatures and liquefying gases [11, 12] because of its simplicity. The first Stirling cycle based cryocoolers were developed by Philips during the 1950's.

The basic setup to operate a Stirling thermodynamic cycle is shown in Figure 1.4, and consists primarily of an ambient compression piston, a cold expansion piston, and a regenerator separating the two. The piston motions necessary to produce the idealised cycle in Figure 1.2(a) and Figure 1.3 are also illustrated.

The cycle is carried out with the following four steps:

(i) Starting at **1** the cold piston expands the working fluid while a quantity of heat, Q_c, is taken in causing it to follow the isotherm **1–2**.

(ii) Starting at **2** the expansion and compression pistons move in unison to transfer the working fluid to the warm end of the system at constant volume, following the isochor **2–3′**. Moving through the regenerator, the fluid receives heat to bring

it up to the ambient temperature, and the pressure increases in accordance with the ideal gas law.

(iii) Starting at **3′** the ambient piston compresses the fluid while a quantity of heat, Q_a, is rejected to the surroundings causing it to follow the isotherm **3′–4′**.

(iv) Starting at **4′** the expansion and compression pistons move in unison to transfer the working fluid to the cold end of the system at constant volume, following the isochor **4′–1**. Moving through the regenerator, the fluid gives heat to bring it down to the cold temperature, and the pressure decreases in accordance with the ideal gas law.

In reality, from a mechanical perspective, it is easier to have pistons moving in simple harmonic oscillations rather than the sequence described above. These simple harmonic motions are far from ideal, however, and the thermodynamic cycle varies accordingly. Also note that in the conventional Stirling cycle there is a piston at the cold end of the system. Keeping this lubricated at low temperatures causes problems in other mechanical coolers but the pulse tube has a novel way to get around it.

1.4.4 The Orifice Pulse Tube Cooler

The cooling effect of what is now known as the basic pulse tube, essentially a hollow tube closed off at one end and driven with pressure oscillations at the other, was first discovered and reported by Gifford and Longsworth in 1964 [13]. Intuitively, there should be no cooling because the mass flow and pressure in the tube would be 90° out of phase, this is analogous to an RC circuit that has no real power unless the current and voltage are in phase. A Stirling cooler brings mass flow and pressure into phase by using an expansion piston 90° out of phase with the compression piston. However, there is no expansion piston in a pulse tube and so the cooling mechanism of the basic pulse tube was, at first, a mystery. After further investigation of this phenomenon the cooling effect was found to be caused by surface heat pumping between the working fluid and the tube walls [14]. This produces a small phase shift between the pressure and mass flow in the the pulse tube, which is necessary for cooling to occur. However, the phase shift is so small that this method of cooling was too inefficient for it to be useful, and the idea was dismissed by the majority as a curiosity rather than being something that could have practical applications.

A major breakthrough took place about two decades later when Mikulin *et al.* introduced the orifice [15] with the intention of increasing the phase shift and therefore the

refrigeration power. Instead of being completely blocked off at the warm end of the pulse tube, Mikulin *et al.* had a narrow orifice restriction valve and a large reservoir, or buffer volume. This setup is now called the *orifice* pulse tube cooler and is illustrated in Figure 1.5. It is shown in the common 'U' configuration which keeps the coldest parts at the bottom and the warmest parts at the top.

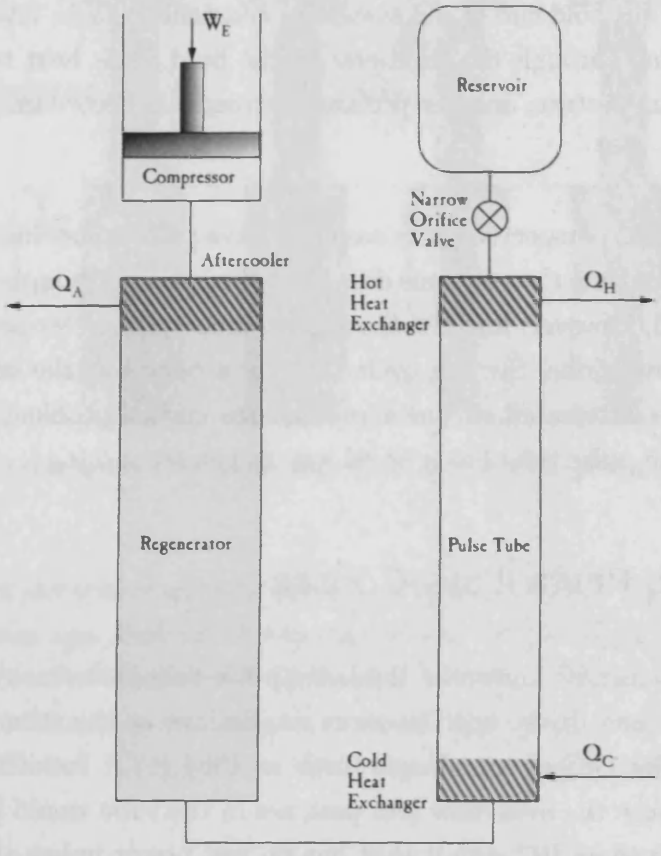

FIGURE 1.5: Schematic of an orifice pulse tube cooler in a 'U' configuration. The 'hot' end is shown at the top. See text for details.

During operation, a shock front forms in the pulse tube which can be thought to serve as the expansion piston of a conventional Stirling cooler. The gas entering the pulse tube from the regenerator does work on the gas already in the pulse tube, producing cooling. This work is transferred to the hot end of the pulse tube and rejected as heat, Q_H. The slug of gas also prevents heat transfer from the hot end to the cold end provided that convection currents can be avoided.

Ideal Efficiency

There is a fundamental inefficiency compared to coolers using active phase shifting mechanisms, such as the Stirling's expansion piston, because of this passive phase shifting method. The expansion work in a Stirling cooler is recovered, whereas the work in a pulse tube is dissipated and lost into the ambient heat sink [16]. This is illustrated in Figure 1.6 which shows schematics of the energy exchange in a Carnot, Stirling and Pulse Tube thermodynamic cycle.

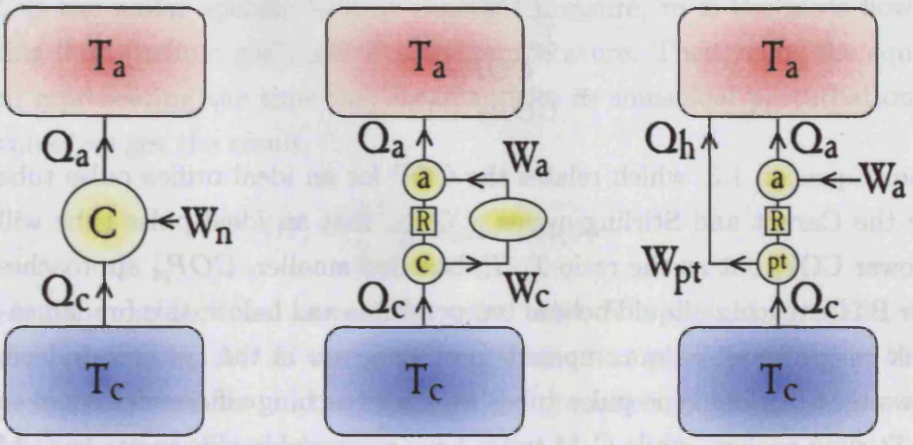

(a) Carnot. *C* — Hypothetical Carnot refrigerator.

(b) Stirling. *a* — ambient compression piston, *c* — cold expansion piston, *R* — regenerator.

(c) Pulse Tube. *a* — ambient compression piston, *pt* — pulse tube, *R* — regenerator.

FIGURE 1.6: Carnot, Stirling, and Pulse Tube cycle energy exchange schematics.

For the Stirling cycle in Figure 1.6(b) the net work is $W = W_a - W_c$ and assuming an ideal regenerator, $W_a = Q_a$ and $W_c = Q_c$. Therefore, the COP for the Stirling cycle remains the same as for the Carnot cycle (as stated previously). From the definition of COP, Equation 1.1,

$$\begin{aligned} COP &= \frac{Q_c}{W} \\ &= \frac{Q_c}{W_a - W_c} \\ &= \frac{Q_c}{Q_a - Q_c} \\ &= \frac{T_c}{T_a - T_c} \end{aligned}$$

Which is identical to the result for a Carnot cycle, Equation 1.2.

However, for the Pulse Tube cycle in Figure 1.6(c) the expansion work is lost as heat, Q_h, and so the net work is $W = W_a$ and this is equal to Q_a for the ideal regenerator case. The COP is therefore,

$$\begin{aligned} COP_{pt} &= \frac{Q_c}{W} \\ &= \frac{Q_c}{W_a} \\ &= \frac{Q_c}{Q_a} \\ &= \frac{T_c}{T_a} \\ &= \frac{COP_C}{COP_C + 1} \end{aligned} \tag{1.3}$$

You can see from Equation 1.3, which relates the COP for an ideal orifice pulse tube to the COP for the Carnot and Stirling cycles, COP_C, that an ideal pulse tube will always have a lower COP, but as the ratio T_c/T_a becomes smaller, COP_{pt} approaches COP_C. Thus for PTCs reaching liquid helium temperatures and below, this fundamental inefficiency is insignificant when compared to other losses in the system. Indeed, Radebaugh shows that Stirling type pulse tubes are now reaching efficiencies equal to or greater than Stirling coolers, while G-M types have comparable efficiencies to G-M coolers [17].

Ideal Cooling Power and it's Relation to Phase Angle

Treating the pulse tube as an open adiabatic device [18], we see that the ideal cooling power stems from the net enthalpy flow within the tube. A schematic for this representation of a pulse tube is shown in Figure 1.7. The dots signify the usual time derivatives and the angled brackets the time averaged quantities over one thermodynamic cycle, in other words $\langle \dot{X} \rangle \equiv \frac{1}{\tau} \oint \frac{dX}{dt} dt$ with τ being the time period for one thermodynamic cycle and t being time.

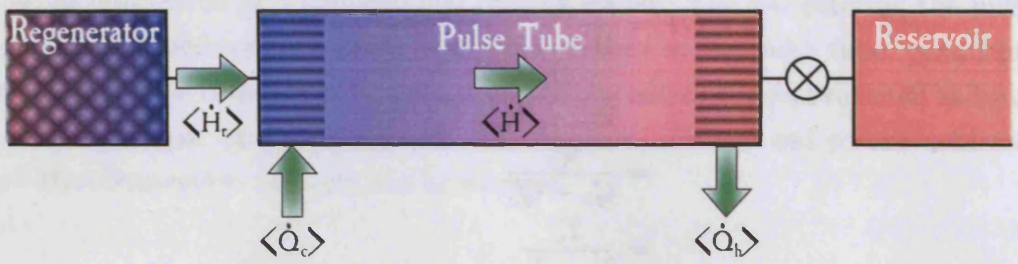

Figure 1.7: Enthalpy flow within a pulse tube.

From energy conservation we get $\langle \dot{Q}_c \rangle = \langle \dot{H} \rangle - \langle \dot{H}_r \rangle$ and $\langle \dot{H} \rangle = \langle \dot{Q}_h \rangle$. The net enthalpy flow from the regenerator, $\langle \dot{H}_r \rangle$, is equal to 0 for an ideal regenerator, so the cooling power for the ideal case is simply $\langle \dot{Q}_c \rangle = \langle \dot{H} \rangle$.

For an ideal gas we can use the relation between enthalpy and the specific heat at constant pressure to write,

$$\langle \dot{H} \rangle = \frac{C_p}{\tau} \int_0^\tau \dot{m} T \, dt \qquad \text{[W]} \tag{1.4}$$

where C_p is the molar specific heat at constant pressure, $\dot{m}$ is the mass flow rate of the working fluid (helium gas), and T is the temperature. Then, using the equation of state, and representing the time varying quantities as sinusoidal perturbations about a mean value, we get the result,

$$\langle \dot{H} \rangle = \frac{1}{2} \frac{C_p A}{R} u_0 \Delta P \cos(\phi) \qquad \text{[W]} \tag{1.5}$$

where A is the cross-sectional area of the pulse tube, R is the gas constant, u_0 is the gas velocity amplitude, ΔP is the pressure variation amplitude, and ϕ is the phase angle between the mass flow in the tube and the pressure oscillations (see section A.2 for a full derivation of this result).

Further Advancements

The ideal cooling power is at a maximum for $\phi = 0$ in Equation 1.5, which is what the introduction of the orifice moves towards. The orifice pulse tube still has a phase angle of around 30° however [18]. Another problem with the system is that the mass flow through the regenerator is large and results in significant losses within the regenerator (a large $\langle \dot{H}_r \rangle$). The next major development designed to address these problems was reported in 1990 by Zhu *et al.* who introduced a bypass between the warm end of the pulse tube and the warm end of the regenerator [19, 20]. In addition to creating a larger phase shift and smaller phase angle, the bypass reduces the flow through the regenerator and the resulting losses. It also drives the compression and expansion of the portion of gas within the pulse tube that always remains at the warm temperature. PTCs with these bypasses are referred to as 'double-inlet' (orifice) pulse tubes.

Although the bypass solves one problem it also raises another potential problem — DC flow, also called streaming. The bypass provides a link for a possible circuit of working fluid which will result in a significant loss of refrigeration power. Even though the DC

component of flow is very small compared to the AC flow, because the temperature difference is so large, the enthalpy carried from the warm end to the cold end by this DC component is still very large. To counteract the natural tendency for DC flow that exists, the bypass is usually asymmetric to restrict flow in one direction. This can be achieved using needle valves for example.

There have been other developments in pulse tube design, one of which is a network of bypass valves at the warm end. As well as counteracting DC flow, these allow for some fine tuning in the phase relationships to obtain the best possible performance and come as close as possible to an idyllic thermodynamic cycle by being actively controlled [21]. Alternatives to the orifice valve have also been looked at and developed, the main example being the inertance tube [17].

1.4.5 Summary of Regenerative Cryocoolers

The major advantage of PTCs over G-M and Stirling cryocoolers is that they have no cold moving parts that need sophisticated methods to prevent seizure, and hence PTCs are more reliable. Another consequence of this is that they produce a lot less unwanted vibration on their cold tip. As touched upon previously in this section, PTCs can be generally grouped into two types — G-M types, and Stirling types. The difference between the two types is simply down to the method used to drive the compression stage of the cycle. G-M types use compressor units with check valves or a rotary valve to alternately connect the high and low pressure sides to the top of the regenerator, usually at a frequency between one and ten Hz. Stirling types use a pressure oscillator and no valve system, usually at frequencies up to 100 Hz. The lower frequency of the G-M types allows them to reach lower temperatures but with lower efficiencies. For single stage systems G-M type PTCs are now reaching below 30 K while Stirling types reach around 60 K.

In the majority of cases the compression is supplied with a separate unit attached to the main assembly using flexible lines. This means that there can be no moving parts at all in the cryostat assembly, and vibrations from the compression unit can be damped out as necessary in the open. Now the only movement that you have to consider within the cryostat is that produced by pressure variations in the cooler.

Table 1.2 summarises the differences between the three types of cryocoolers discussed. Radebaugh [22] also provides a good discussion on the development of PTCs and how they fit into the family of mechanical coolers.

Method	Advantages	Disadvantages
Stirling	Uses a small volume (single cold finger).	Cold moving parts. Low eficiency compared to Stirling type PTRs.
G-M	High efficiency compared to G-M type PTCs.	Cold moving parts. Large amount of vibration from displacer.
Pulse tube	No cold moving parts (better reliability, lower vibration, lower cost). High efficiencies for Stirling types.	Relatively new and not fully understood (requires costly experimental optimisation). Low efficiencies for commercial G-M types. Susceptible to convection (limits orientation).

TABLE 1.2: Summary of regenerative mechanical cooler methods.

1.5 METHODS FOR OBTAINING SUB-KELVIN TEMPERATURES

Sub-K refrigerators can be further categorised into above 300 mK and below 300 mK. Above 300 mK there is no reason not to use a ^{3}He refrigerator as it is simple and reliable. It is also reasonably straight forward to adapt them to operate in any orientation and even in "zero" gravity.

Below 300 mK experimenters are faced with more decisions. Traditionally, dilution refrigerators have dominated the 100 mK range while Adiabatic Demagnetisation Refrigerators (ADRs) were used only for the lowest temperatures (nuclear demagnetisation). However, space applications and advances in ADR technology, particularly the magnets, have elevated interest in them to a level where they now compete with dilution refrigeration. No special adaption is necessary for an ADR to operate onboard a satellite whereas dilution refrigerators are more tricky to adapt than ^{3}He refrigerators, especially if continuous operation is desired.

All of the methods mentioned above require some form of precooling and traditionally operate from a base temperature of 4 K; that given by a liquid helium bath at atmospheric pressure. The methods themselves are summarised in the following sections and there are many books that describe these methods in more detail, see for example

[23, 24, 25].

1.5.1 HELIUM-3 EVAPORATION

The simplest method of obtaining sub-K temperatures is to lower the vapour pressure above a liquid ^{3}He bath, thus causing ^{3}He to evaporate from the liquid and lowering its temperature. The ^{3}He isotope has a much higher vapour pressure than ^{4}He for a given temperature, which allows the condensed liquid to reach lower temperatures with the same available pumping efficiency. This difference comes about because of the lower zero point energy of the ^{3}He atoms compared to the ^{4}He atoms.

In order to condense the ^{3}He (which has a boiling point of 3.2 K at atmospheric pressure) efficiently, a pumped bath of ^{4}He is used providing a condensation point of around 1 K. This stage is often incorporated into the refrigerator resulting in a two stage system. Once condensed, the liquid ^{3}He bath is pumped on, resulting in a final temperature around 0.3 K.

Physisorption, short for 'physical adsorption' and also referred to as cryopumping, rather than external rotary/turbo pumps is used to create a vibrationless system. Physisorption is the process where He atoms stick to surfaces at low temperatures via Van de Waal forces [26]. A large surface area is provided by activated charcoal 'zeolite' pellets[2] so that the pumping efficiency is not reduced during the pumping stages of the refrigeration cycle. Activation of the charcoal is necessary to remove any contaminating particles such as water molecules, and involves heating the charcoal to release such contaminates.

The operation of a ^{3}He refrigerator essentially comes down to the controlling of the cryopumps. The cryopump is heated up to 40 K or more to release gas for it to be condensed, and it is held at this temperature while the gas condenses. To pump on the liquid the cryopump is cooled rapidly by turning on a heat switch that connects it to the precooling system (PTC, liquid ^{4}He bath *etc.*), hence causing the ^{3}He vapour to become adsorbed once more. An additional benefit of using cryopumps is that it means the system is self contained and can therefore be designed to be transferable between different cryostats if necessary.

There are several types of heat switches that can be used to control the cryopump's temperature. Those used during this work, and that are also popular in general, are

[2] These are also used in room temperature filtering systems, to remove oil vapour for example.

gas gap heat switches [27]. These use their own small cryopump, with a weak passive thermal link to the precooler, to release/remove gas from a small gap between two conductors. When turned on, the gas filling the gap conducts heat between the two ends. When turned off, there is only a small amount of conduction through the stainless steel walls of the heat switch housing.

1.5.2 Adiabatic Demagnetisation Refrigeration

ADRs use the entropy of a magnetised paramagnetic salt pill to cool down to temperatures below 0.1 K. The salt pill is first magnetised using a strong magnetic field, often provided by a superconducting coil, and then as the field is gradually relaxed the salt pill absorbs heat from the load and becomes demagnetised as its entropy increases. In quantum mechanic terms, the energy levels of the electrons are split and further separated for increasingly strong magnetic fields (Hyperfine splitting). The energy levels are manipulated to produce cooling in a way that is analogous to the compression and expansion of an ideal gas. Some examples of the salts used in ADRs include Cerium Magnesium Nitrate, Ferric Ammonium Alum (Sulfate) and Chromium Potassium Alum.

The refrigeration cycle for an ADR is as follows. The magnetic field is ramped up to full strength to magnetise the salt pill. This raises the temperature of the salt pill as electrons in the split energy levels have their energy raised. This unwanted heat of magnetisation is removed by having the salt pill placed in contact with a heat sink provided by the precooler. The electrons move down to the lower of the split energy levels and the system is thus more ordered, and therefore has a lower entropy. This stage is equivalent to an isothermal compression of a gas.

The link to the heat sink is now broken so that the salt pill is isolated and therefore at constant entropy. The magnetic field strength is decreased and the energy levels begin to converge. Since the distribution of electrons does not change, the overall energy and temperature decreases. This is equivalent to an adiabatic expansion of a gas.

The salt pill can now be used as a refrigerant by pacing it in contact with the load that is to be cooled. There is naturally a limit to the amount of cooling available since zero field means that there is no hyperfine splitting and therefore no heat capacity available for cooling. Also, at low field strengths, electron spin interactions become significant and this self magnetisation limits the minimum temperature achievable for individual paramagnetic salt materials, typically several mK. Salt based ADRs therefore tend to

operate in the 100 mK range.

Once the magnetic field has reached its minimum, the process can be repeated to continue cooling the load or maintain its low temperature. The process is therefore a single-shot process like that of a ^{3}He evaporation refrigerator.

Temperatures below 1 mK can be achieved by applying the technique to the nuclear spin system of certain metals (Copper, Platinum or Platinum-Iron alloy for example). Such refrigerators are not of direct concern for the purposes discussed in this thesis, but discussion of the differences between using the nuclear and electron subsystems is available in the aforementioned references ([23, 24, 25]).

1.5.3 Dilution Refrigeration

Dilution refrigerators make use of the properties of ^{4}He-^{3}He mixtures at very low temperatures. The mixture separates into two phases below about 0.7 K, the exact temperature depending on the concentration of the ^{3}He[3], one made up of almost pure ^{3}He and the other consisting of dilute ^{3}He in ^{4}He. As the temperature decreases further the concentrated ^{3}He layer becomes more pure and the dilute ^{3}He approaches a definitive concentration of 6.6%.

The differing number of nucleons in ^{3}He and ^{4}He atoms means that ^{4}He follows Bose-Einstein statistics (integer spin) while ^{3}He follows Fermi-Dirac statistics (half-integer spin). This means that the ^{4}He in the dilute layer undergoes Bose-Einstein condensation and the atoms have a tendency to all sit in the lowest energy level. The ^{3}He atoms meanwhile, cannot occupy the same energy levels as each other and so there is a limited amount 'allowed' in the dilute layer, hence the definite concentration.

Dilution cooling is achieved by freeing up energy levels in the dilute layer for ^{3}He atoms in the concentrated layer to cross into — their energy level is lowered and cooling occurs. To free up energy levels the ^{3}He in the dilute layer is boiled off in a still at around 0.6 K. The much higher vapour pressure of ^{3}He compared to ^{4}He means that more than 99% of the liquid boiled off in the still is made up of the ^{3}He isotope. This means that it is actually possible for the ^{3}He to be collected and recycled if desired.

Dilution refrigerators compete with ADRs for 100 mK temperatures and applications.

[3] A typical concentration for a dilution refrigerator has a separation temperature around 0.4 K.

1.5.4 Summary of Sub-Kelvin Refrigerators

A summary of the sub-K cooling processes is provided in Table 1.3.

Method	Advantages	Disadvantages
^{3}He Evaporation	Very simple. Reliable. Light weight.	Limited to above 250 mK. Low efficiency. "One shot" cooling cycle.
ADR	Can reach below 100 mK. Unaffected by orientation and "zero" gravity.	Large magnetic fields within cryostat. Heavy. "One shot" cooling cycle.
Dilution	Can reach below 100 mK. Large cooling power even at lowest temperatures. Can be continous.	Relatively complex. Needs to be rigourously leak tight due to superfluidity of ^{4}He. This can take a lot of time to get right.

Table 1.3: Summary of sub-Kelvin cooling methods.

1.6 Bolometric Detectors And Potential Noise Sources

Bolometric detectors are the most sensitive detector type for far-infrared/submillimetre wavelengths, although they can be designed for and used at many different wavelengths. The advantages and disadvantages for a variety of technologies are summarised in Table 1.4 and are explained in more detail in the following sections. An overview of bolometric detectors, their operation, and the sources of noise that are encountered during their operation and optimisation is given.

Bolometer theory has been covered in great detail elsewhere in the past and so my aim here is only to highlight the points of main concern and the relevant equations. I will start with the general idea of bolometric detectors and then go on to describe the semiconductor variety that has been at the heart of this research, and also touch upon the superconducting types that the latest experiments are using or at least moving towards.

The first comprehensive general theory of bolometric detectors was first published by Jones in 1953 [28]. Further developments of the theory have since been added to

Type	Advantages	Disadvantages
NTD-Ge Composite	Well understood and reproducible. Most sensitive of the semiconductor variety.	Difficult to produce. Slow. Fragile - can be unreliable.
InSb Hot-electron	Very fast - gives large bandwidth. Robust. 'High' operating temperatures. Easy to read out.	Comparatively low sensitivity. Unstable - characteristics can change over time.
TES	Fast. High sensitivity. Easy to produce in large arrays.	Relatively complex read out. SQUID amplifiers susceptible to stray magnetic fields.

TABLE 1.4: Summary of bolometric detectors.

extend coverage to non-equilibrium [29], and to study certain effects such as that of background power loading [30]. For a more current review of bolometric detectors see Richards [31].

1.6.1 BOLOMETERS IN GENERAL

A bolometric detector works by absorbing radiation, which causes a rise in temperature that is subsequently detected by a change in resistance. It is therefore an incoherent, or total power, detector in that it does not retain any information on the phase of the incident photons. The basic components of a bolometer are an absorber, an attached thermistor, and a heat sink connected by an appropriate thermal link. This is illustrated in Figure 1.8. Quite often bolometers consist of a separate absorber and thermistor (as depicted in Figure 1.8), for example, a silicon-nitride mesh with a bonded NTD-Germanium chip. However, these functions can also be carried out by a single monolithic structure in some designs. Also, the absorber may have to be placed on a supporting substrate for structural support. The thermal link is usually provided by the electrical leads that are used to read out the resistance of the thermistor.

The total power dissipated in the bolometer, W, is the sum of the incident radiation

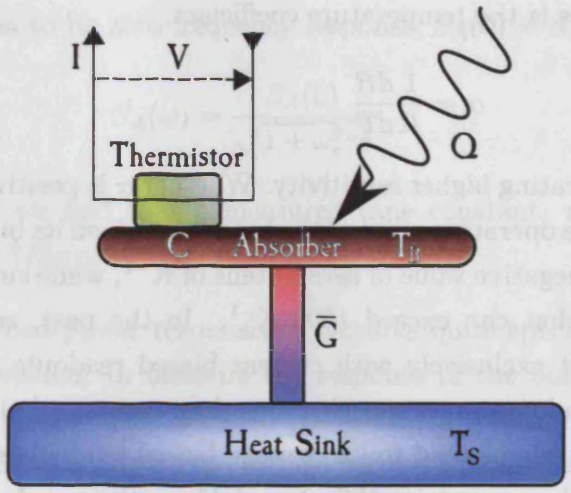

FIGURE 1.8: Schematic of the main components of a composite bolometric detector. See text for description.

power, Q, and the electrical power $P = IV$, where I is the bias current and V is the signal voltage drop across the bolometer. Some of this power is dissipated through the thermal link with average conductance $\bar{G}$ to the heat sink at temperature T_S, whilst the remainder raises the bolometer temperature to T_B as determined by the bolometer's heat capacity, C. By considering the steady state energy balance equation it is easily shown that the temperature of the bolometer is,

$$T_B = T_S + W/\bar{G} \quad \text{[K]} \tag{1.6}$$

and if you consider the case where the incident radiation is initially turned on, the physical time constant for the response of the bolometer is shown to be,

$$\tau = \frac{C}{\bar{G}} \quad \text{[s]} \tag{1.7}$$

You can see from Equation 1.6 and Equation 1.7 that there is a conflict of interests when designing a bolometer for a particular application: For maximum sensitivity we would like the changes in T_B, due to the changes in incident radiation, to be as large as possible, which means having a small $\bar{G}$. On the other hand, we would generally like the bolometer to be as fast as possible with it's response, which means having a large $\bar{G}$. Therefore, compromises need to be made that suit the requirements of the experiment being designed.

The sensitivity of the thermistor fundamentally depends on how rapidly its resistance varies with temperature, at the operating temperature. The quantity introduced by

Jones [28] to characterise this is the temperature coefficient,

$$\alpha = \frac{1}{R}\frac{dR}{dT} \qquad [\mathrm{K}^{-1}] \tag{1.8}$$

with a larger magnitude indicating higher sensitivity. Whether α is positive or negative determines the stability of the operating point of the bolometer given its biasing system. For semiconductors α has a negative value of several tens of K^{-1}, while superconductor TESs have positive values that can exceed 1000 K^{-1}. In the past, semiconductor bolometers were used almost exclusively with current biased readouts since voltage amplifiers were available with lower noise specifications than current amplifiers. Today, superconducting bolometer systems tend to use voltage biased readouts as technology has advanced enough to make current amplifiers a viable option, and using current biasing would have resulted in thermal runaway.

1.6.2 Bolometer Responsivity

It is important when using any optical detector to know how it will respond to changes in incident radiation – either the change in output voltage, or change in output current, depending on the readout method. During calibration the optical responsivity, S, is measured for the instrument as a whole, but it is desirable to calculate the absorbed power responsivity, S_A, before hand. The two are related by the absorptivity, η, through $S = \eta S_A$.

The absorbed power responsivity for optical radiation with modulation frequency ω_s is,

$$S_A = \frac{\alpha V}{G_e(1 + i\omega_s \tau_e)} \qquad [\mathrm{VW}^{-1}] \tag{1.9}$$

Where $G_e = G - \alpha P$ is defined as the effective thermal conductance, and $\tau_e = C/G_e$ is the measured effective time constant. The derivation of this and the other results summarised here can be found in section B.1. The effective thermal conductance, G_e, represents the effect of the electrothermal feedback that takes place in a bolometer; an increase in the optical power causes a rise in temperature, but this causes a drop in resistance (for a negative α) and therefore electrical power. Taking the magnitude of Equation 1.9 gives us an expression for the bolometer's sensitivity to signals of varying

frequencies in relation to its zero frequency response, $S_A(0) = \alpha V/G_e$.

$$S_A(\omega) = \frac{S_A(0)}{\sqrt{1+\omega_s^2\tau_e^2}} \qquad [\mathrm{VW}^{-1}] \tag{1.10}$$

From Equation 1.10 we find that a measured time constant, τ_e, gives a half-power (-3 dB) frequency of $1/2\pi\tau_e$.

Measuring the absorbed power responsivity requires quite specific apparatus, and so it is often more convenient to measure the response of the bolometer to changes in dissipated electrical power. This is called the electrical responsivity, S_E. To measure the electrical responsivity a load curve (voltage-current characteristics) of the bolometer is taken, from which S_E can be calculated using,

$$S_E = \frac{Z-R}{2IR} \qquad [\mathrm{VW}^{-1}] \tag{1.11}$$

where $Z = dV/dI$ is the dynamic impedance. Many data points must be collected over the range where the output voltage changes rapidly with bias current for accurate values of S_E to be calculated. Care must also be taken for low bias currents since both the numerator and denominator of Equation 1.11 approach zero as I approaches zero.

1.6.3 Noise Contributions

An ideal bolometer is subject to three noise sources, and only two of these are intrinsic to the bolometer itself.

Johnson noise arises from the random motion of thermally excited electrons within a resistive material. The voltage noise resulting from this is,

$$V_{nJohnson} = (4k_BTR)^{1/2} \qquad [\mathrm{VHz}^{-1/2}] \tag{1.12}$$

where k_B is the Boltzmann constant. The voltage noise is referred to a noise equivalent power (NEP) by the bolometer responsivity.

$$NEP_J = \frac{V_{nJohnson}}{|S|} \approx \frac{(4k_BTR)^{1/2}}{|S_E|} \qquad [\mathrm{WHz}^{-1/2}] \tag{1.13}$$

The NEP contribution due to Johnson noise is reduced by making the responsivity as large as possible. There is also a Johnson noise contribution from the load resistor(s), R_L, however this is made negligible by choosing $R_L \gg R$.

Phonon noise arises due to the quantised nature of heat transport through the thermal link from absorber to heat sink. It has an NEP contribution,

$$NEP_P = (4k_B T^2 G)^{1/2} \quad [\mathrm{WHz}^{-1/2}] \tag{1.14}$$

Photon noise arises from the random arrival of photons to the detector. Naturally it depends on the optical throughput of the instrument design, however since this work was carried out on bolometers 'blanked off', *ie.* the detector only sees the surrounding heat sink temperature, it is neglected.

Additionally, when reading a bolometer there are also noise contributions from the readout electronics, namely the preamplifier current and voltage noise. The current noise contributes to the overall voltage noise through the load resistor-detector potential divider. The overall voltage noise for the amplifier is

$$V_{nPreamp} = \sqrt{e_n^2 + \left(i_n \frac{R_L R}{R_L + R}\right)^2} \quad [\mathrm{VHz}^{-1/2}] \tag{1.15}$$

where i_n and e_n are the preamplifier input noise current and noise voltage respectively, and R_L is the load resistance. This overall voltage noise is again referred to a corresponding NEP by the responsivity (*cf.* Equation 1.13). The preamplifier input current and voltage noise depend on the design of the amplifier.

The overall NEP is found by adding the contributions from each source in quadrature, since these sources are uncorrelated;

$$NEP^2 = NEP_J^2 + NEP_P^2 + NEP_{Preamp}^2 \quad [\mathrm{W}^2\mathrm{Hz}^{-1}] \tag{1.16}$$

1.6.4 NTD-Ge Bolometers

The particular type of detector used for the majority of this investigation was a composite NTD-Ge (Neutron Transmutation Doped Germanium) mesh bolometer. It is a design that later evolved into the spider web bolometer, like those being used for the non polarisation sensitive part of the *Planck* mission [32], and its major components are essentially the same while its construction is less sophisticated. Following the schematic in Figure 1.8, the thermistor is an NTD-Ge chip bonded to a silicon-nitride (Si_3N_4) mesh that acts as the absorber, and has two superconducting niobium wires attached with indium solder which read the resistance of the NTD-Ge chip and pro-

vide the dominant component of the thermal link's conductance. An additional small component of the thermal conductance comes from several strands of the Si_3N_4 that suspend the mesh.

Bolometers based upon semiconductor technology became popular because of the exponential dependence of their resistance on temperature. The NTD process became useful in producing large quantities of uniform material in a controlled way, from which many chips that behaved the same way could be made. During characterisation of an NTD-Ge chip the resistance-temperature curve is fitted to the relationship,

$$R(T_B) = R_* exp\left(\frac{T_g}{T_B}\right)^n \qquad [\Omega] \tag{1.17}$$

The parameters R_* and T_g are found by plotting $\ln R$ against $1/T_B{}^n$. n is usually taken to be 0.5, but for high precision modelling and characterisation, such as that developed by Sudiwala *et al.* [33], it is left as a free parameter.

The model fit of the load curve implicitly characterises the average, also referred to as static, thermal conductance, $\bar{G}_S(T_S)$, where the subscript 'S' signifies a bolometer temperature equal to the heat sink temperature, and material parameter, β, for each heat sink temperature, T_S. For a given value of $\bar{G}_S$ at some temperature T'_S, $\bar{G}_S$ can be calculated for *any* heat sink temperature using the relation,

$$\bar{G}_S(T_S) = \bar{G}_S(T'_S)\left(\frac{T_S}{T'_S}\right)^\beta \qquad [\mathrm{WK}^{-1}] \tag{1.18}$$

This assumes that β is independent of the heat sink temperature, as is the case for an ideal bolometer, but in practice it usually has a small amount of variation [34]. Note that in the full model presented by Sudiwala *et al.* [33], it is the thermal conductivity that is modelled as a power law and not the conductance. Therefore the relation shown in Equation 1.18 is only applicable for values of $\bar{G}$ where the bolometer temperature is equal to the heat sink temperature. However, in the case of no optical loading and given $R(T_B)$, $\bar{G}$ can be obtained from the load curve using,

$$\bar{G} = \frac{IV}{T_B - T_S} \qquad [\mathrm{WK}^{-1}] \tag{1.19}$$

which stems directly from Equation 1.6.

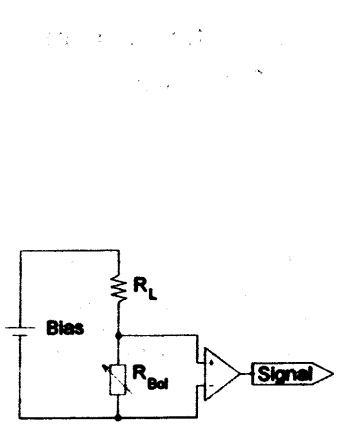

FIGURE 1.9: Basic current biased bolometer readout.

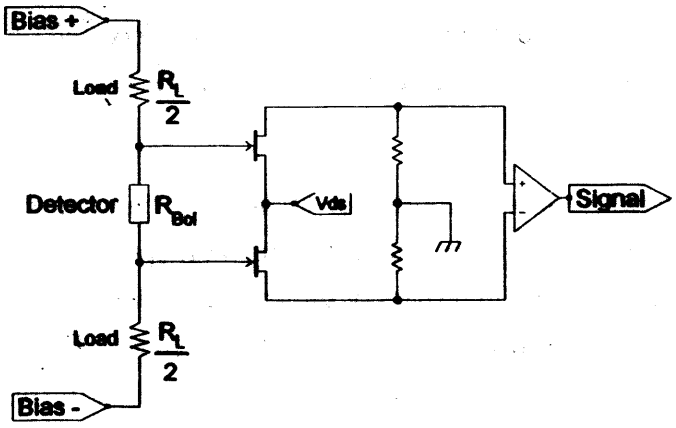

FIGURE 1.10: Current biased differential bolometer readout using a matched JFET pair.

NTD-Ge Bolometer Readout Electronics

The basic readout for a current biased bolometer is shown in Figure 1.9. A battery supplies a bias voltage and a load resistance acts with the detector as a potential divider. The potential drop across the detector is then amplified. The load resistor has a value much larger than the impedance of the detector so that the current through the detector is approximately constant.

A differential readout scheme can be used to remove the effects of environmental noise; for example, noise resulting from changes in the electronic's ambient temperature or stray magnetic fields. By using a symmetrical readout, the schematic of which is shown in Figure 1.10, and taking the difference of the the two signal lines, any common noise component is rejected. The fully differential readout scheme is discussed in more detail by Naylor *et al.* [35].

JFETs are the amplifiers of choice for NTD-Ge bolometers because the high detector impedance necessitates a low preamplifier current noise (*cf.* Equation 1.15). As the active component of the amplifier the JFETs characteristics determine the amplifier noise component of the bolometer performance. The JFET voltage noise is given by

$$e_{nJFET} = \sqrt{4k_B T R_N} \qquad [\mathrm{VHz^{-1/2}}] \tag{1.20}$$

where $R_N \approx 0.67/g_{fs}$ is the noise equivalent resistance which is a characteristic of the JFET with its forward transconductance, g_{fs}. The JFET current noise is given by

$$i_{nJFET} = \sqrt{\frac{4k_B T}{R_{GS}} + 2eI_G} \qquad [\mathrm{AHz^{-1/2}}] \tag{1.21}$$

where e is the electron charge. The first term is the 'thermal' noise (depending on the gate-source resistance, R_{GS}) and the second is the 'shot' noise (depending on the reverse gate current, I_G).

1.6.5 InSb Hot Electron Bolometers

The applications of InSb hot-electron bolometers include mixers for sub-mm line astronomy as well as direct detectors for spectroscopy purposes, plasma diagnostics and so on. As a semiconductor the free electrons in a sample of InSb tend to 'freeze out' at liquid helium temperatures. However, the electrons are only weakly bonded to the crystal lattice and the valence band overlaps the conduction band for an InSb crystal, therefore the electrons are easily excited into the conduction band by an applied electric field, *ie.* when a bias is applied. The free electrons form a thermalised electron gas that can be described by the Fermi function using a single temperature, T_e. This temperature is greater than or equal to the lattice temperature, T_l, hence the name 'hot-electron'.

The components necessary for the operation of an InSb sample as a bolometric detector are all intrinsic. The electron gas serves both as the absorber and as the thermistor. The crystal lattice serves as the heat sink and is connected to the electron gas through electron-phonon interactions. Radiation absorbed by the electron gas raises the Fermi temperature of the electron gas. This increases the mobility of the electrons, $\mu \propto T_e^{2/3}$. The decrease in resistance of the InSb sample leads to nonlinear load curves (voltage-current characteristics) thus allowing the device to be used as a bolometer. The timescales for the electron-phonon interactions together with the low mass of the charge carriers which are doing the absorbing means that such a detector is relatively fast. At 4.2 K the relaxation timescale is approximately 0.3 μs, corresponding to a -3 dB instantaneous bandwidth of approximately 1 MHz.

InSb HEBs are also current biased for their readout, however the amplifier and load resistance do not need to be mounted close to the detector because their impedance is a lot lower than an NTD-Ge bolometer. Instead, they are are typically mounted in an RF shielded box mounted on the cryostat at room temperature.

1.6.6 TES Bolometers

Superconducting technologies are in the process of replacing semiconductor bolometers and this is partly made possible because of the advances in current amplifiers; in particular, the superconducting quantum interference devices (SQUIDs). Although no such detectors have been used during the course of this study, they are mentioned here as an indication of where progress is going.

Transition edge sensors (TESs) operate at the transition between their normal and superconducting states, as their name suggests. The positive α for this resistance-temperature slope requires a voltage bias for it to be stable, via electrothermal feedback, and hence the requirement of a current amplifier. The benefit of overcoming this technological obstacle is a thermistor that has an α of several hundred K^{-1} (*cf.* 5–10 K^{-1} for a semiconductor bolometer) and therefore a very sensitive detector. Not only are TES bolometers sensitive but the strong electrothermal feedback results in a very fast detector. Therefore the result is a combination of sensitivity and speed that was previously only available individually.

TES devices are also relatively simple to produce using only thin film deposition, and their operating temperatures can be controlled through differing thicknesses of these films and combinations of superconducting metals. Naturally a TES bolometer can be manufactured as a composite device with a TES thermistor on an absorbing substrate, but refined deposition and etching techniques allow for large monolithic arrays of TES detectors to be produced. Such an array of over 10,000 pixels is to be used on the *SCUBA-2* instrument for the James Clerk Maxwell telescope [36]. This will be the first instance of a 'CCD-like' device being used for submillimetre astronomy and will almost certainly revolutionise the field.

1.7 Scope Of This Thesis

The next chapter provides background context of some of the work previously carried out and related to the study. The third chapter gives the details of the apparatus used for the investigations and its setup. The fourth chapter gives details of the tests carried out on a 300 mK NTD-Ge bolometer, and the fifth chapter gives those for the tests on a 4 K InSb HEB. The sixth chapter describes the measurements of the temperature fluctuations performed on the PTC and sorption refrigerator cold heads. The seventh and final chapter contains a summary of the main results and discusses

the investigations in relation to each other. In chapter seven I also make some suggestions for future study in this field, such as further investigation into increasing the temperature stability of the detector platform, and investigating the use of voltage biased superconducting bolometers with pulse tube systems.

Chapter 2

Previous Investigations Into Detector Performance In Mechanical Cooler Systems

There have been a large number of independent investigations into closed-cycle cooler systems, their effects on detector performance, and designs and modifications to reduce their vibration at the detector stage. Most studies are directed at particular experiments and so a lot of information unfortunately remains hidden within internal project documents. A few studies are more general, with a view to increasing our understanding for the benefit of future experiment design.

In this chapter I describe two of the studies that have been done to provide more context and highlight important points of consideration for my own work. *Polatron* is an instrument which demonstrated that not all types of mechanical cooler are suitable for every application. The general study of Bhatia *et al.* shows the importance of the detector readout electronics as well as the technology of the detector itself, and has an underlying implication that thermal effects could be just as important as microphonics. It also shows that the use of mechanical coolers for high photon background applications, those using photoconductors, is very feasible.

2.1 POLATRON: An Example Of A Study Specific To An Experiment

Polatron was a polarisation sensitive bolometric instrument designed to study the Sunyaev-Zel'Dovich (SZ) effect and the CMB, and was the subject of a feasibility study by Rossinot as part of his PhD thesis [37]. As well as aiming to resolve features in the CMB polarisation spectrum, the experiment was a proof of concept for future experimental designs utilising mechanical coolers. In this section I will briefly describe the cryogenic design of *Polatron*, the detectors and readout system used, and then go on to summarise the results of the tests carried out by Rossinot *et al.*

2.1.1 POLATRON Cryogenics

Polatron was designed to be cryogen free, with the cooling from room temperature to 4.2 K provided by two Gifford-McMahon (G-M) coolers and a Joule-Thompson[1] (J-T) expansion valve. The two G-M stages are necessary to pre-cool the He gas to below its maximum inversion temperature, approximately 51 K for ^{4}He, so that cooling can occur when it undergoes isenthalpic expansion at the 4.2 K J-T stage [38].

The G-M coolers produce much more vibration than a Pulse Tube cooler and are therefore more susceptible to causing microphonic noise because of their cold displacers. On the plus side, the J-T stage does not have any moving parts and is very reliable and easily controlled in its temperature and cooling power by adjusting the aperture size.

The sub-Kelvin cooling that is required for operating semiconductor bolometers is provided by a three stage sorption cooler. The first stage uses ^{4}He to reach a temperature of around 1 K, and then two ^{3}He stages take this to below 300 mK. See subsection 1.5.1 and subsection 3.1.2 for more details of sorption cooler operation.

2.1.2 POLATRON Detectors And Readout

The bolometric detectors proposed for use in the *Polatron* experiment were NTD-Ge chips mounted on a Si_3N_4 'spider web' mesh absorber. In this case there were two

[1] Sometimes called Joule-Kelvin expansion from before he changed his name, or isenthalpic expansion.

bolometers for each channel; one to detect each orthogonal component of the incoming polarized radiation. An AC bridge along with JFETs in a differencing scheme was used to read out the pair of detectors to reject the common mode signal between the two bolometers. This differencing scheme gives an output voltage proportional to the difference of the two polarisations but in many respects is very similar to an AC readout of a single bolometer. Again, a more detailed description of such a readout is described in subsection 3.2.2.

2.1.3 POLATRON FEASIBILITY TESTING

Noise measurements were carried out on high impedance resistors, a thermistor, and finally the bolometer itself in order to analyse the cryocooler's microphonic affects on *Polatron*. The testing started with the resistors and worked up to the bolometer with increasing susceptibility to thermal fluctuations and microphonics.

The noise measurements of a 3.7 MΩ resistor were carried out at three different temperatures — 300 K, 5 K, and 300 mK. The resistor's noise was dominated by Johnson noise (Equation 1.12) which has a significant dependance on temperature, and so the noise of the resistor was seen to decrease. At the coldest temperature the Johnson noise was low enough to be able to see the microphonic pickup caused by the cryocooler. This range of sharp peaks were attributed by Rossinot to the cryocooler and instrument resonant frequencies. The results were still encouraging and the resistor was replaced with a thermistor since there was a quiet region in which to operate the bolometer between 0.3 and 2 Hz.

The thermistor noise measurements were again carried out at 300 K, 5 K, and 300 mK. Additional noise was seen to be present only in the 300 mK measurements. The expected peaks caused by the cryocooler were evident as well as some additional $1/f$ noise due to temperature instability of the sorption cold-head during the measurements. Nevertheless the results were encouraging enough to move onto the bolometer.

First of all, the bolometer performance with the cryocooler turned off momentarily was measured to represent conditions in a conventional 'wet' cryostat. A noise floor of 13.8 $nV_{rms}Hz^{-0.5}$ was measured at a cold head temperature of 270 mK. Measurements were then taken at 5 K and 270 mK with the cryocooler switched on. These results are shown in Figure 2.1. The noise at 5 K was lower than at 270 mK due to the NTD-Ge chip's lower impedance at this temperature and reduced responsivity. However, it was immediately apparent that the noise was greatly increased with the cryocooler

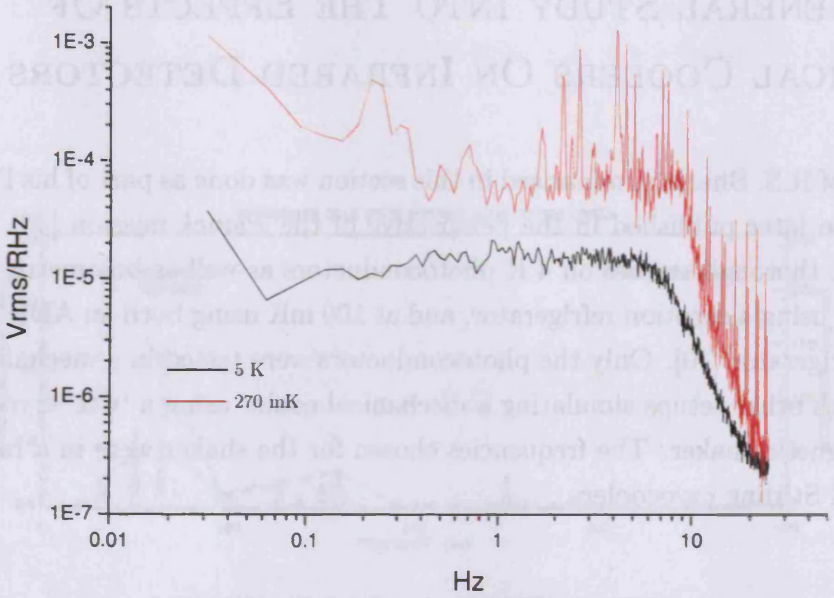

FIGURE 2.1: *Polatron* noise measurements of the bolometer with the cooler turned on (Rossinot [37]). Note that the baseline noise level of 13.8 $nV_{rms}Hz^{-0.5}$ is off the bottom of the y-axis scale.

turned on, even at 5 K. In the proposed operating frequency range the noise level was 56.7 $\mu V_{rms}Hz^{-0.5}$ at 270 mK, compared to about 15 $\mu V_{rms}Hz^{-0.5}$ at 5 K.

2.1.4 POLATRON CONCLUSIONS

The bolometer noise performance was inadequate to perform the science goals that *Polatron* was designed for, despite having sophisticated vibration isolation apparatus in place in the instrument, consisting of pneumatic bellows at the top of the cryocooler and flexible thermal links to the cold stages. It was concluded by Rossinot that only with fundamental changes to the instrument design, such as using an alternative mechanical cooler, could any further improvement be made to the detector performance. It was proposed that a pulse tube cooler could possibly have the necessary cooling power while not compromising the detector.

2.2 General Study Into The Effects Of Mechanical Coolers On Infrared Detectors

A lot of the work of R.S. Bhatia summarised in this section was done as part of his PhD thesis [39] but also later published in the perspective of the *Planck* mission [40, 41]. Bhatia carried out thorough studies on 4 K photoconductors as well as bolometric detectors at 350 mK using a sorption refrigerator, and at 100 mK using both an ADR [39] and a dilution refrigerator [40]. Only the photoconductors were tested in a mechanical cooler system[2] with other setups simulating a mechanical cooler using a 'wet' cryostat and an electromagnetic shaker. The frequencies chosen for the shaker were in a range typical of J-T and Stirling cryocoolers.

2.2.1 Photoconductor Testing

The photoconductor[3] tests were aimed at determining the microphonic effects of cryocoolers on FTS (Fourier Transform Spectrometer) instruments that typically use such detectors, often for Earth observations. Baseline measurements were obtained in an electromagnetically quiet 'wet' cryostat before moving the detector block into the RAL 4 K prototype cryocooler. The tests were then repeated using momentum compensation on the Stirling displacers. An illuminator[4] was used to ensure that the detector was photon noise limited.

The acceleration levels at the 4 K plate were measured (top panel in Figure 2.2) in the longitudinal direction and it can be seen that the momentum compensator has a great affect on the results, particularly at the 32 Hz fundamental frequency of the Stirling stages. The lower two panels in Figure 2.2 compare the photoconductor noise in the mechanical cooler to its noise in the 'wet' cryostat, the middle panel showing 0–200 Hz and the bottom panel 0–3.2 kHz. Also note that the Stirling harmonic frequencies are marked with a $\diamond$, and the J-T harmonic frequencies are marked with a +. Above about 500 Hz the cryocooler seemed to degrade the noise performance very little; below 500 Hz the main features introduced were peaks at the cooler's harmonic frequencies, plus some $1/f$ type noise at 25 Hz and below. When repeated with the momentum compensation in place, the detector noise did not show any improvement. In his paper, [40], Bhatia remarks that this may have been because of some saturation effect. Regardless, the

[2] A 2-stage Stirling system with a 4 K J-T expansion stage.
[3] In this case Ge:Ga detectors for 50–120 μm wavelengths.
[4] A calibrated black body source.

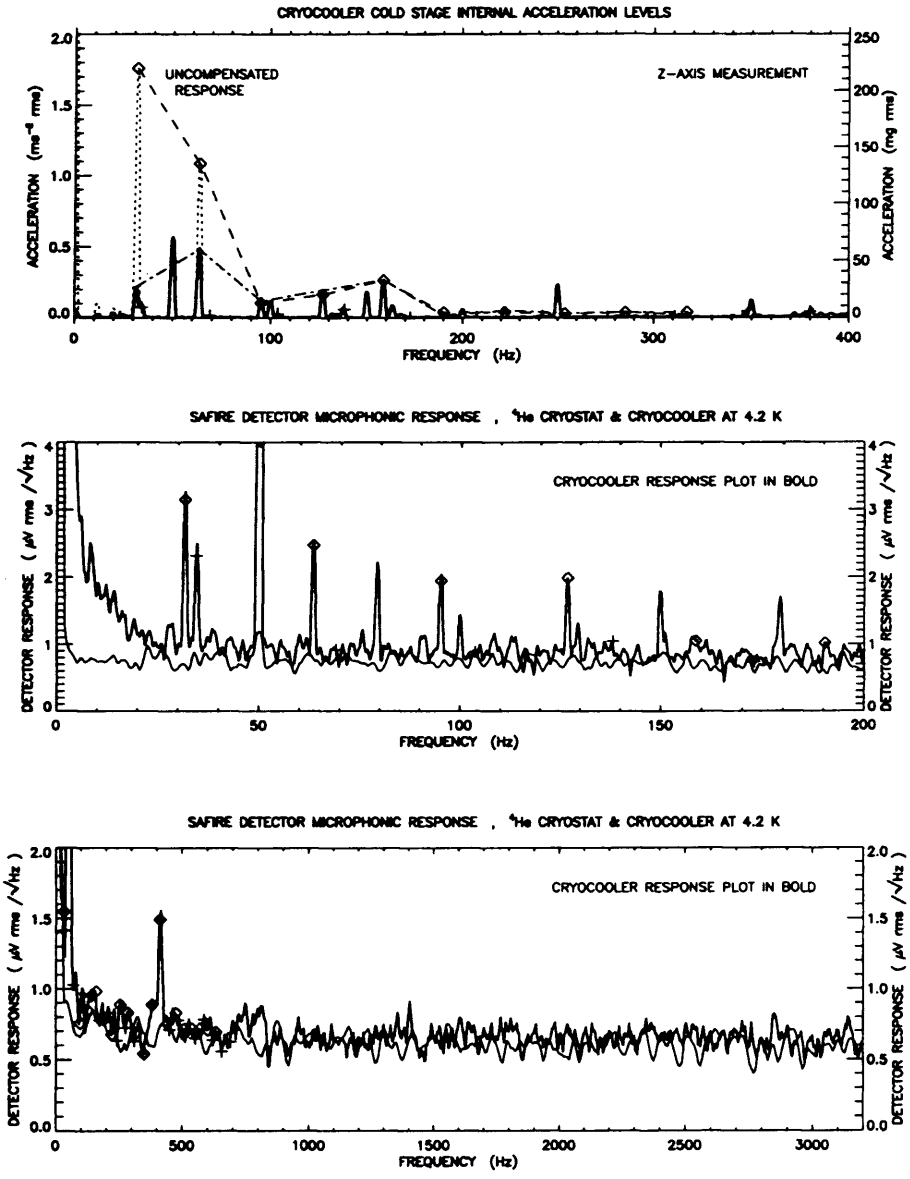

FIGURE 2.2: Photoconductor noise and acceleration measurements. The top panel shows the acceleration levels within the cryostat with and without the momentum compensation, the lower panels show the detector noise in a 'wet' cryostat and the RAL 4 K cryocooler, *without* compensation, for two different frequency ranges. [40]

tests have shown that using cryocoolers for high photon background experiments is very feasible, given that the tests were performed in an unoptimised system.

2.2.2 Bolometer Testing

All tests carried out on the bolometric detectors had microphonics simulated using a 'wet' cryostat and external shaker rather than an actual mechanical cooler. The main disadvantage of this method is that although it provides the vibration associated with mechanical coolers, the experiment is still carried out in a liquid He cryostat that has very good temperature stability and cooling power. Bhatia's ultimate aim with these tests was to get the first microphonic noise tests for 100 mK bolometers in a system that replicates *Planck* as closely as possible. I therefore present them in chronological order as the details of the *Planck* mission became better defined.

350 mK Sorption Refrigerator Tests [39]

For the initial tests a comparatively simple 350 mK system was set up with a ^{3}He sorption cooler built into a liquid ^{4}He cryostat. The bolometer was an NTD-Ge chip mounted on a 25 μm sapphire absorber substrate. This has a lower resonant frequency than a spider web bolometer, due to its higher mass, making it more susceptible to microphonic induced noise.

Tests were performed with the bolometer blanked off so that optical modulation would not produce any additional features in the noise spectra. The amplitude of the external shaker vibration was increased at frequencies of 10, 18, 32, and 72 Hz until the driving signal became noisy (non-sinusoidal). These tests were then repeated with the bolometer replaced by flat-pack resistors of equivalent resistance, with the wiring to the JFET stage changed to twisted pairs, and finally with the bolometer optically loaded. Note that the readout was a single ended DC system, using one JFET, and with one side of the bolometer connected to the cryostat ground.

The bolometer and resistor responded differently to the changing shaker frequency. Bhatia reports that at 10 Hz the resistor was much less prone to microphonics than the bolometer. At 18 Hz they were comparable, and at higher frequencies the resistor became *more* prone to microphonics.

The performance of the bolometer with and without twisted pair wiring between the bolometer and the JFET stage, and using a shaker frequency of 18 Hz is shown in

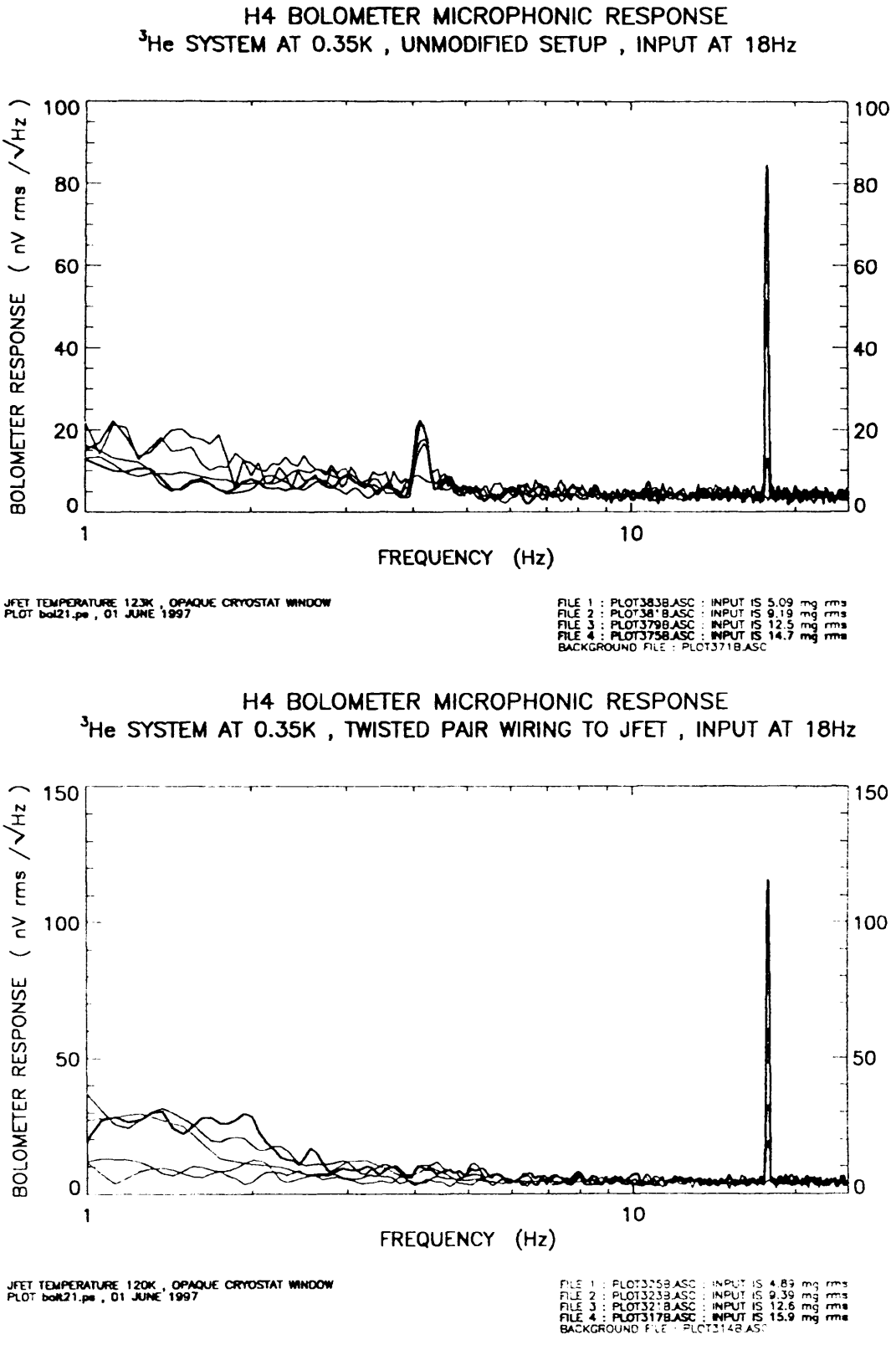

FIGURE 2.3: Bolometer response to increasing levels of 18 Hz excitation, with and without twisted pairs wiring. [39]

Figure 2.3. A peak at the 18 Hz shaker frequency increases monotonically with the vibration magnitude, thus showing that the system is prone to microphonic pickup. The low frequency noise, below about 4 Hz, does not show any correlation with the vibration magnitude. Above 4 Hz, around the shaker frequency, the noise level seems to be largely unaffected by the shaker's excitation.

A similar behaviour was seen for the resistor, as shown in Figure 2.4. Generally speaking, the fundamental peak at 18 Hz was suppressed significantly by using twisted pair wiring. This can be clearly seen for the resistor noise plots at 18 Hz excitation, however, in this instance for the bolometer it is not the case. It was also noted by Bhatia that the twisted pairs wiring had more effect at the higher frequencies, and that mains pickup was increased compared to the original setup because a second ground wire was needed for the twisted pair configuration. Because the same effects were seen with the resistor output it can be concluded that they are not thermal in origin but are problems with the wiring or readout system. A differential readout using a matched JFET pair, for example, would have helped reject any pickup. Again, I will stress at this point that only small thermal effects, to do with reduced cooling power in the sorption refrigerator due to vibrations, can be expected when simulating a mechanical cooler with an external shaker.

Optically loaded tests of the bolometer were performed with it observing a sheet of Eccosorb®[5] at 300 K through a 2 mm bandpass filter to avoid overloading the bolometer. Figure 2.5 compares the response of the bolometer when optically loaded to that when it is blanked off. The bolometer's responsivity is reduced and it is therefore less susceptible to microphonics because it is optically loaded. This is shown by the overall lower noise level in the lower plot of Figure 2.5, and the lower peak heights at the fundamental frequency. However, there is some optical modulation effect seen at the second harmonic frequency, 32 Hz, which displays a peak higher than the blanked off noise plot. This set of results therefore highlights an important consideration for 'real' systems viewing sources external to the cryostat.

100 mK ADR Tests [39]

The *Planck* mission will utilise bolometers operating at 100 mK and so the next step for Bhatia was to carry out microphonic tests at this temperature. At the time, 100 mK spider web bolometers were still under development and so the first tests at this temperature were performed on a bolometer that was already well characterised, in this

[5] Available from Emerson & Cuming Microwave Products

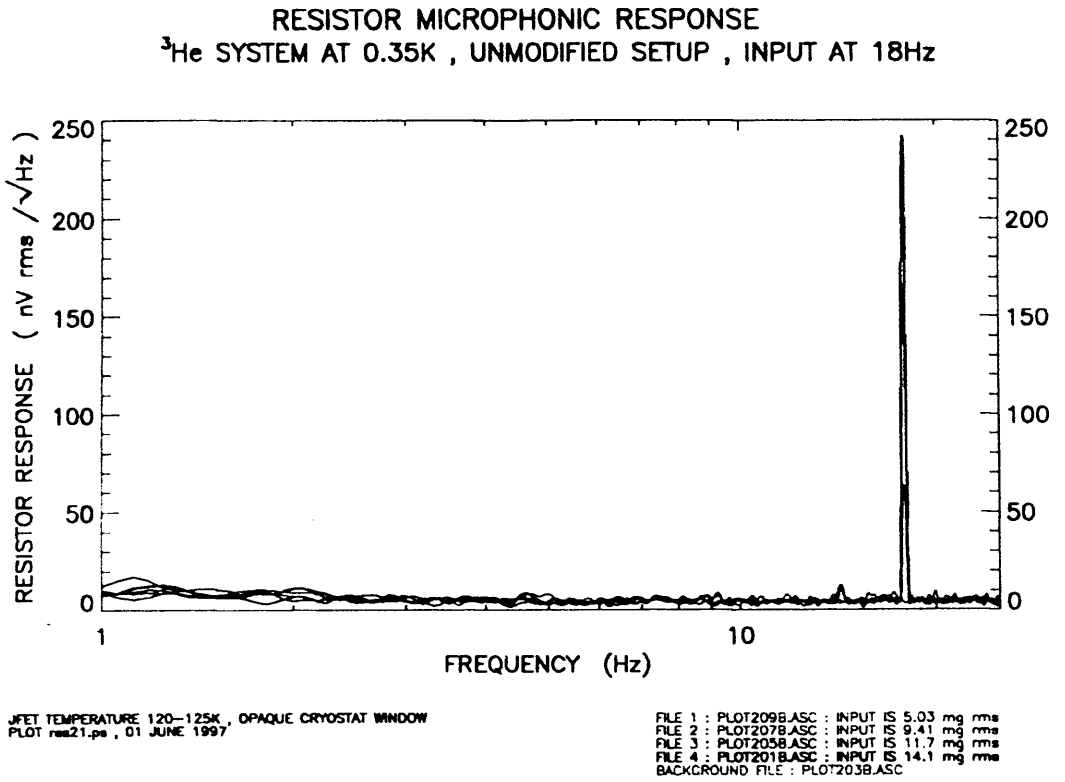

FIGURE 2.4: Resistor response to increasing levels of 18 Hz excitation, with and without twisted pairs wiring. [39]

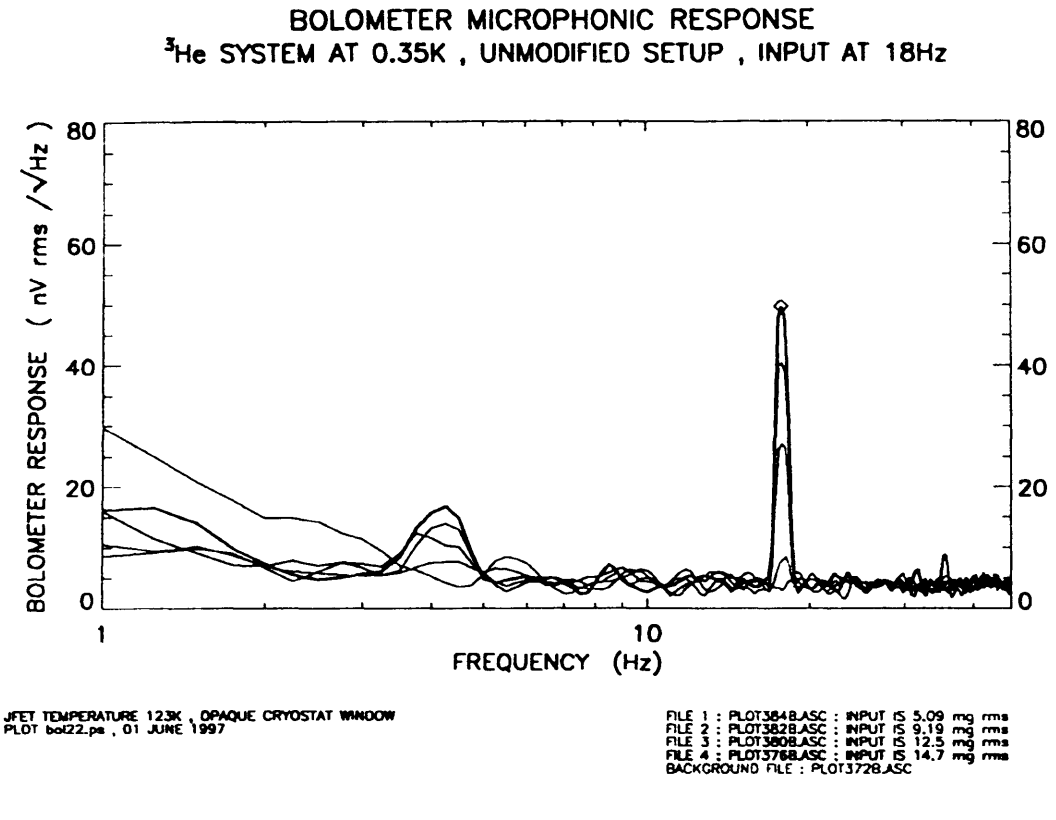

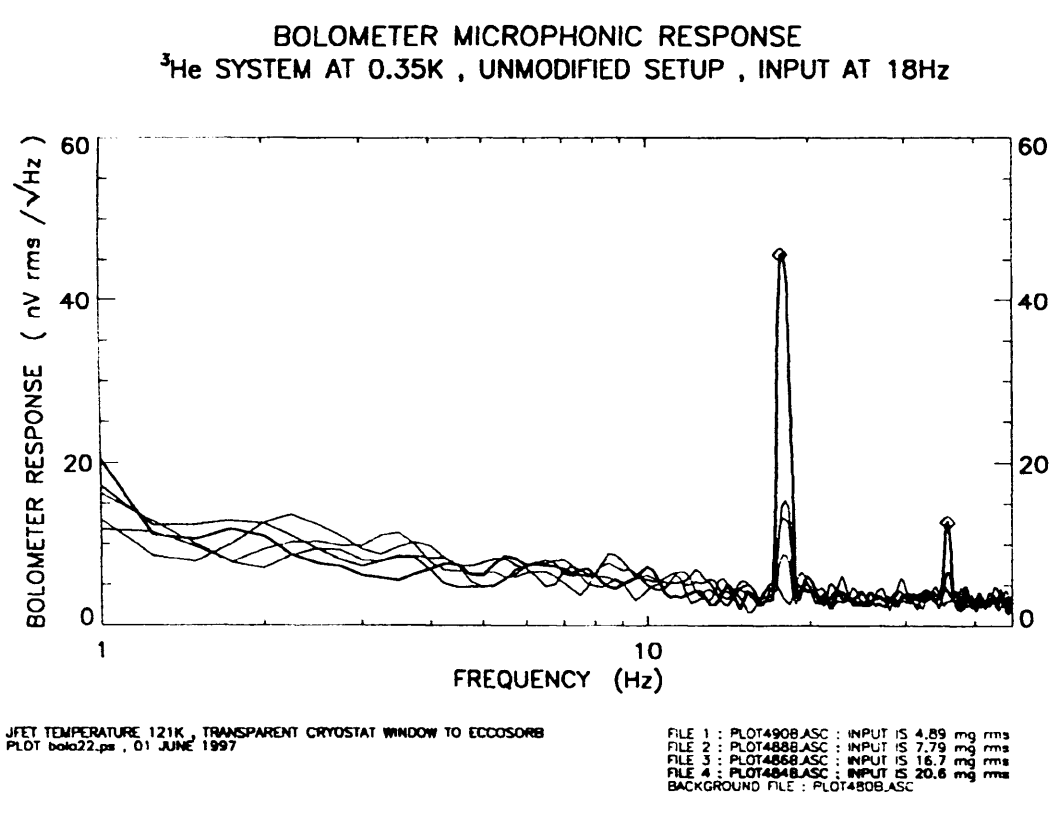

FIGURE 2.5: Bolometer repsonse when optically loaded (lower) compared to being blanked off (upper). [39]

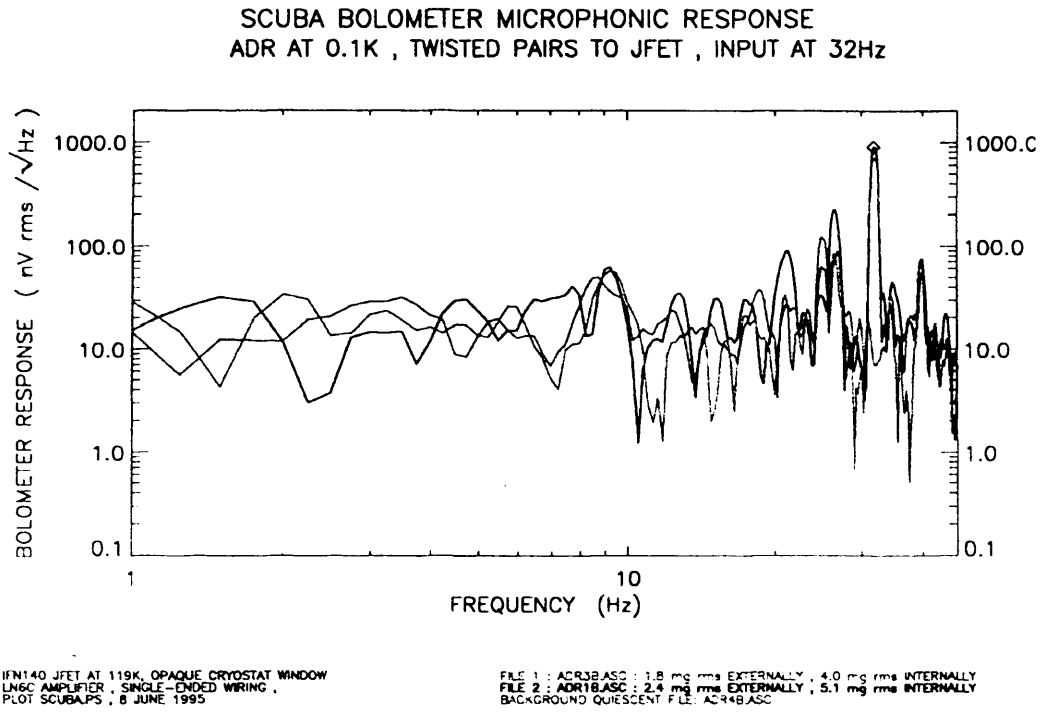

FIGURE 2.6: Microphonic response of a *SCUBA* bolometer in an ADR system [39].

case a detector design that was implemented on the *SCUBA* array. The ADR system was chosen because it had optical access that would be needed to fully characterise the 100 mK spider web bolometers. It does provide more cooling power (10 μW) than that available to *Planck* ($\sim$100 nW) however, and so does not give a wholly realistic representation of the instrument. The ADR system was again used in conjunction with the external shaker. Some modification to the way the shaker was set up had to be made, however, due to the greater mass of the ADR system compared to the ^{3}He adsorption cryostat.

The readout for the *SCUBA* detector during these tests was the same as for the 350 mK tests, and also used twisted pair wiring to the JFET stage. The frequency chosen for the shaker was 32 Hz and after measurements were taken with no input, the amplitude was increased until the shaker drive became distorted. A sample of the results can be seen in Figure 2.6. The response under excitation was similar to the quiescent spectrum and the expected total noise level of 17.4 $nV_{rms}Hz^{-0.5}$, except for some features at certain frequencies above 10 Hz; most notably the shaker frequency of 32 Hz. Some important effects may have been masked however, because of the detector's relatively high NEP ($\geq 1\times10^{-16}$ $W_{rms}Hz^{-0.5}$) compared to the more recent spider-web bolometers. These results show that the readout system continued to be prone to microphonic pickup even with the newer bolometer technology.

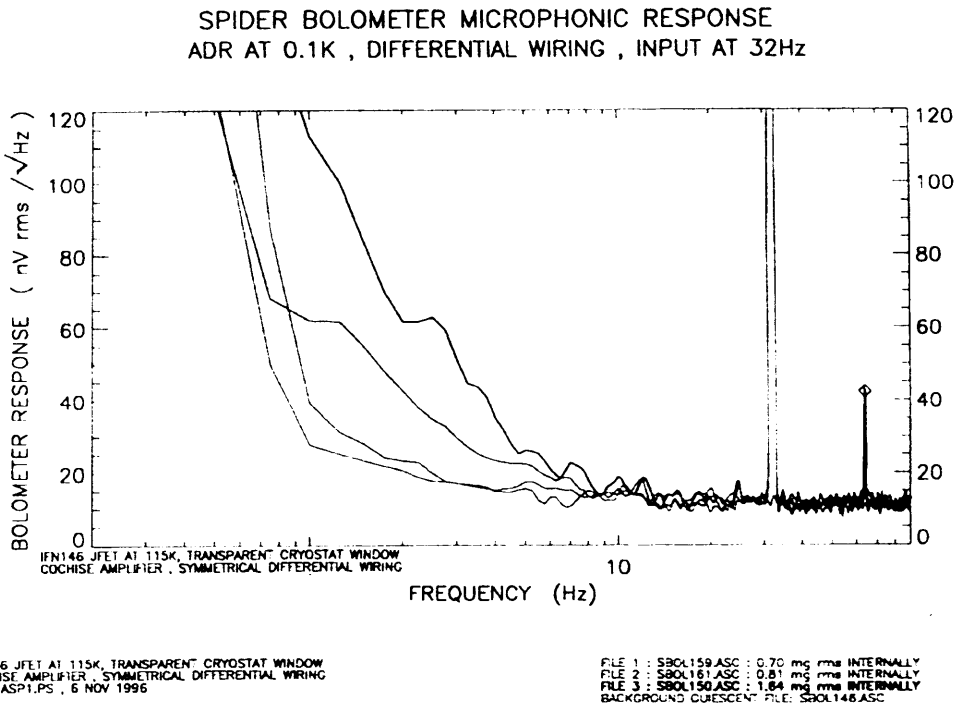

FIGURE 2.7: Optically loaded bolometer microphonic response in an ADR system [39].

Bhatia *et al.* characterised a prototype 100 mK spider-web bolometer, once it became available, and repeated the previous tests. This device was designed to have the lowest NEP without paying attention to any needs for speed of response. The readout was modified to be a differential readout using a matched JFET pair, and with one bias line grounded. After load curve and speed of response measurements, the same tests as before were carried out. The results for the spider-web bolometer viewing 300 K can be seen in Figure 2.7. Again, there is a strong peak at the shaker frequency of 32 Hz and its harmonic, but the detector response remained close to the quiescent response apart from some increase in the $1/f$ noise below 8 Hz.

The noise levels for the quiescent spectrum at 1, 3 and above 10 Hz, were 26, 18, and 13 $nV_{rms}Hz^{-0.5}$ respectively. Values for the optical NEP, shown in Table 2.1, were obtained using the measured optical responsivity and the electrical responsivity calculated from the detector's load curve.

The tests were repeated with the bolometer blanked off at the ^{4}He shield and these noise responses are shown in Figure 2.8. The results are very similar to the optically loaded tests with the exception that the second harmonic peaks are larger and the $1/f$ noise lower for comparable levels of shaker excitation. Taking into account the photon noise at lower frequencies the quiescent noise levels at 1, 3 and above 10 Hz, were 21,

Frequency (Hz)	Optical NEP ($W_{rms}Hz^{-0.5}$)		Blanked off NEP ($W_{rms}Hz^{-0.5}$)
	Optical Responsivity (1.2×10^{9} VW^{-1})	Electrical Responsivity (3.4×10^{9} VW^{-1})	
1	2.2×10^{-17}	7.6×10^{-18}	9.3×10^{-18}
3	1.5×10^{-17}	5.2×10^{-18}	7.4×10^{-18}
Above 10	1.1×10^{-17}	3.8×10^{-18}	5.2×10^{-18}

TABLE 2.1: Prototype 100 mK spider-web bolometer optically loaded NEP

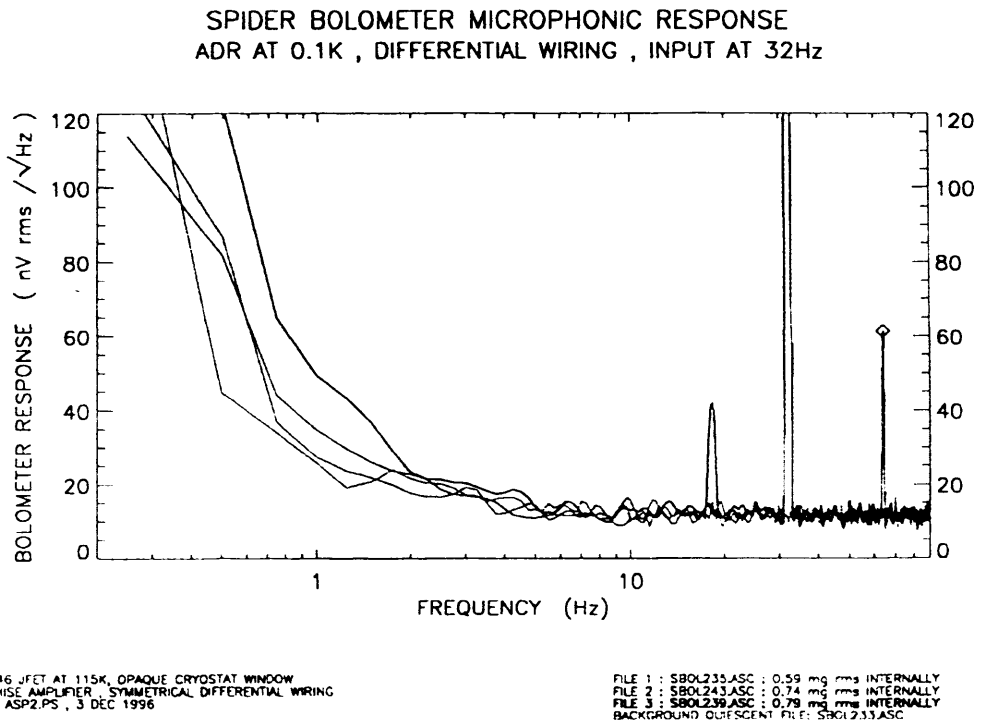

FIGURE 2.8: Blanked bolometer microphonic response in an ADR system [39].

17, and 12 $nV_{rms}Hz^{-0.5}$ respectively. The corresponding NEP's, gained from using an electrical responsivity calculated from load curves taken under blanked off conditions (2.3×10^{9} V/W), are also shown in Table 2.1 for comparison to the optically loaded case.

100 mK DILUTION REFRIGERATOR TESTS [39, 40]

The final set of tests saw more progression towards a test-bed representative of the *Planck* flight system. It used a modified version of the dilution refrigerator proposed for *Planck*, designed to give 100 nW of cooling power at 100 mK. This dilution refrigerator was again pre-cooled using a conventional ^{4}He cryostat with the microphonic

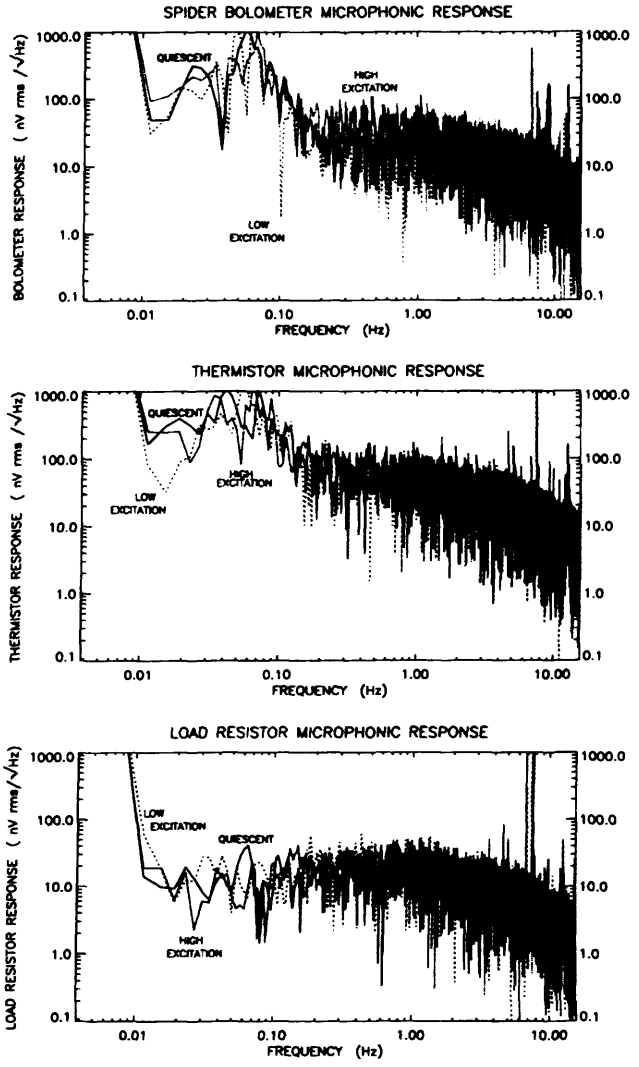

FIGURE 2.9: Bolometer, thermistor, and resistor response to shaker excitation in the dilution system [40].

vibrations being provided by the external shaker operating at 32 Hz. Also, the spider-web bolometer used was a second generation 100 mK type with characteristics aimed towards those of *Planck*'s specifications. The readout was differential and used a JFET pair similarly to that used for the ADR tests. This time it was AC biased and had lock-in detection in the post amplification stage however. All of the measurements were made with the bolometer blanked off at the 100 mK stage.

Figure 2.9 shows the responses of the spider-web bolometer, a thermistor, and a 10 MΩ resistor, to two levels of shaker excitation compared to their quiescent responses. The 'low' and 'high' excitations were measured at the 100 mK stage to be equivalent to 21 and 37 mg_{rms} respectively. The upper panel of Figure 2.9 displaying the bolometer noise spectra shows no noticeable increase in noise for 'low' excitation, and a small

increase in noise level over the 17 $nV_{rms}Hz^{-0.5}$ baseline for frequencies above 0.15 Hz, for 'high' excitation. This increase in noise level for 'high' excitation is not seen in the resistor response shown in the lower panel of Figure 2.9 indicating that it is a thermal effect and not an electrical one. Bhatia suggests that this is because of increased thermal fluctuations due to loss of cooling power of the dilution refrigerator, caused by the microphonic vibrations. The noise floor of the thermistor (middle panel of Figure 2.9) is too high to clearly show this effect. The peak in the bolometer spectra between 0.01 and 0.08 Hz, however, is present in the thermistor spectra as well, whilst being absent from the resistor's. Again, this indicates that it is a thermal effect. This peak was attributed to the limitations of the PID temperature control that was being used.

For the measured electrical responsivity of 1.0×10^{9} V/W the noise level of 17 $V_{rms}Hz^{-0.5}$ gives an electrical (blanked) NEP of 2×10^{-18} $W_{rms}Hz^{-0.5}$. It was estimated by Bhatia that the optical NEP would therefore be approximately 6×10^{-18} $W_{rms}Hz^{-0.5}$, about a factor of two better than the prototype previously tested.

2.2.3 General Study Conclusions

The series of tests carried out by Bhatia *et al.* on different systems clearly show the importance of readout, wiring and detector design. Older bolometer technologies are more susceptible to microphonic effects at lower frequencies, while twisted pair wiring and matched JFET pair amplifiers help reject microphonic noise.

Using a shaker to represent mechanical cooler vibrations produced a high Q peak in all detector responses at the designated shaker frequency. These peaks scaled monotonically with the shaker input amplitude. Some setups also displayed increasing levels of $1/f$ noise but this could arguably be caused by a loss in cryogenic performance in the sub-Kelvin refrigerator rather than a direct microphonic effect. A more noticeable manifestation of this effect was seen in the last series of tests carried out in the dilution refrigerator system. During these tests the whole noise floor of the bolometer was raised when under high shaker excitation. However, the effect was still very small and remained undetectable by the thermistor. Of course a mechanical cooler will create greater temperature instabilities than a shaker, and so there is a limited amount you can learn about these thermal effects from this series of tests.

2.3 Previous Investigation Conclusions

Studies by Bhatia carried out on bolometers with a shaker have shown that vibrations alone are not necessarily a problem for their operation provided that a suitable wiring and readout system is used. Peaks at the fundamental shaker frequency appearing in the detector response range retained a high Q factor, but it must be considered that when using a mechanical cooler it is unlikely to produce clean sinusoidal oscillations at a single frequency. Mechanical coolers also come with other sources of vibration, for example a compressor package, not represented in shaker tests. This is seen in the results from Rossinot's *Polatron* investigation where the detector, thermistor, and resistor responses did not show a single peak, but were contaminated with a series of "cryocooler and instrument resonant frequencies".

Thermal effects were beginning to be seen in the shaker tests when using the more sensitive bolometers and lower noise readouts. Using an actual cryocooler, the *Polatron* system displayed much stronger thermal effects in its bolometer response that no amount of vibration isolation and tweaking of bias settings could rectify.

Chapter 3

Experimental Setup

The overall approach of my own study was to compare bolometric detector performance in a conventional 'wet' cryostat, using liquid helium and nitrogen, with that in a 'dry' cryostat using a mechanical cooler, in this case a PTC. The work therefore involved successfully installing and operating a two-stage ^{4}He-^{3}He adsorption refrigerator in conjunction with the PTC to establish a 300 mK test bed. This hybrid system is the subject of the first half of this chapter.

Two major electronic units were required for the study and are the subject of the second half of this chapter. The first was to operate and monitor the cryogenic system and was developed with the objective of 'turn-key' operation in mind. The second unit was required for the read out of the NTD-Ge bolometer and was built and adapted from several sources.

3.1 Cryogenics

A test bed was set up for the testing and characterisation of 300 mK bolometric detectors in a cryogen free cryostat. The mechanical cooler chosen for this purpose was a PTC. PTCs are becoming the state of the art for obtaining temperatures of 4 K and below because of their reliability due to having no cold moving parts. The final cold head temperature of 300 mK was provided by a two-stage ^{4}He-^{3}He adsorption refrigerator; a self contained unit that condenses and evaporates each isotope in turn after precooling down to approximately 4 K. The two sub systems are completely independent and are described as such in the following sections. Sorption refrigerator-pulse

tube integration has also been reported by Devlin and Dicker *et al.* [42] who achieved a final temperature below 286 mK for 72 hours with 15 μW of thermal load.

3.1.1 Pulse Tube Cryocoolers

Two different makes of commercially available PTCs were used during the investigation; a Cryomech PT405[1], and an equivalent PRK4 model from VeriCold[2]. Both are two-stage double inlet orifice pulse tubes (see subsection 1.4.4) providing around 400 mW of cooling power at 4 K. Each stage forms a 'U' shape with the second stage working off the cold head of the first stage. Each stage of the PTC is used to cool a radiation shield to reduce the thermal input into the sorption refrigerator. The first stage, equivalent to the liquid nitrogen bath of a 'wet' cryostat, operates at a base temperature of 40–60 K depending on the model used (*cf.* 77 K for a liquid nitrogen bath at atmospheric pressure). The second stage, equivalent to the liquid helium bath of a 'wet' cryostat, operates at a base temperature of around 3 K (*cf.* 4.2 K for a liquid helium bath at atmospheric pressure).

The main difference between the two models of PTC is the rotary valve which alternates the connection to the high and low pressure helium lines from the compressor unit. The Cryomech's rotary valve is built into the top of the main PTC assembly and uses a digital stepper motor, while the VeriCold uses an 'external' rotary valve driven by an analogue motor, taking in the high and low pressure lines and then attaching to the main assembly via a single flexible line approximately 30 cm in length. This provides better isolation for the cryostat from the vibrations originating in the compressor.

Theoretical Ideal Cooling Power

An estimate for the cooling power of the two PTCs can be obtained by using Equation 1.5 and estimates for the fluid velocity amplitude, u_0, and the pressure oscillation amplitude, ΔP. When testing PTCs it is easier to measure the mass flow rate at the orifice rather than the gas velocity, so in this case we need to use the alternate form of

[1] Cryomech Inc., 113 Falso Drive, Syracuse, New York, 13211, USA. Email: cryosales@cryomech.com, Web: http//www.cryomech.com

[2] VeriCold Technologies GmbH, Bahnhofstraße 21, 85737, Ismaning, Germany. Telephone: +49 (89) 9699 8560, Email: info@vericold.com, Web: http//www.vericold.com

Equation 1.5,

$$\langle \dot{H} \rangle = \frac{1}{2}\frac{C_p}{m_a}\dot{m}_0\frac{\Delta P}{\bar{P}}T_c\cos(\phi) \quad [\mathrm{W}] \tag{3.1}$$

where the relations $u_0 = \dot{m}_0/(\rho A)$ and $\rho = P/(RT)$ have been used to eliminate u_0 and put the expression in terms of quantities that can be measured directly. The atomic mass of the working fluid, m_a, is used to convert the density from units of [mol m^{-3}] to [g m^{-3}]. For the result to be in S.I. units, the mass flow rate amplitude, $\dot{m}_0$, therefore needs to be in [g s^{-1}].

For PTCs using helium working fluid, $C_p = 5R/2$ (a monatomic gas) and $m_a = 4$. So for the ideal case where $\phi = 0$ (mass flow-pressure phase angle),

$$\langle \dot{H} \rangle \approx 2.60\dot{m}_0\frac{\Delta P}{\bar{P}}T_c \quad [\mathrm{W}] \tag{3.2}$$

Note that the pressure differential decreases with decreasing temperature, since the cold head draws in more helium, so Equation 3.2 is *not* linear with T_c. $\dot{m}_0$ is largely determined by the setup of the orifice and bypass valve(s) and is therefore unique to a particular PTC. For this demonstration we take $\dot{m}_0 \sim 1$ gs^{-1} in the case of a single stage PTR. Without access to detailed measurements of mass flow rates for a two stage system, we simply approximate that 50% of the gas flows through each stage.

For the VeriCold PTC operating at 4 K, the high pressure is 20 bar, and the low pressure is 18 bar. Hence, $\langle \dot{H} \rangle \approx 547$ mW. This is naturally an upper estimate since ϕ tends to be around 30° (which gives $\langle \dot{H} \rangle \approx 473$ mW), and there are no losses considered such as those that occur in the regenerator because of friction and pressure gradient.

For the Cryomech PTC operating at 4 K, the high pressure is 17.5 bar, and the low pressure is 15.5 bar. Hence the upper estimate is $\langle \dot{H} \rangle \approx 630$ mW, and for $\phi = 30°$ $\langle \dot{H} \rangle \approx 546$ mW.

The supplied information for the performances of the two PTCs can be found below.

Cryomech PT405 Specifications

To give an indication of scale, the Cryomech's cold head assembly weighs 14 kg and is 56 cm tall (33 cm cold finger length). The thermal load diagram for the PT405 is shown in Figure 3.1. The load diagram shows the first and second stage temperatures for a range of applied heat loads on both stages. Hence the cooling power of the second

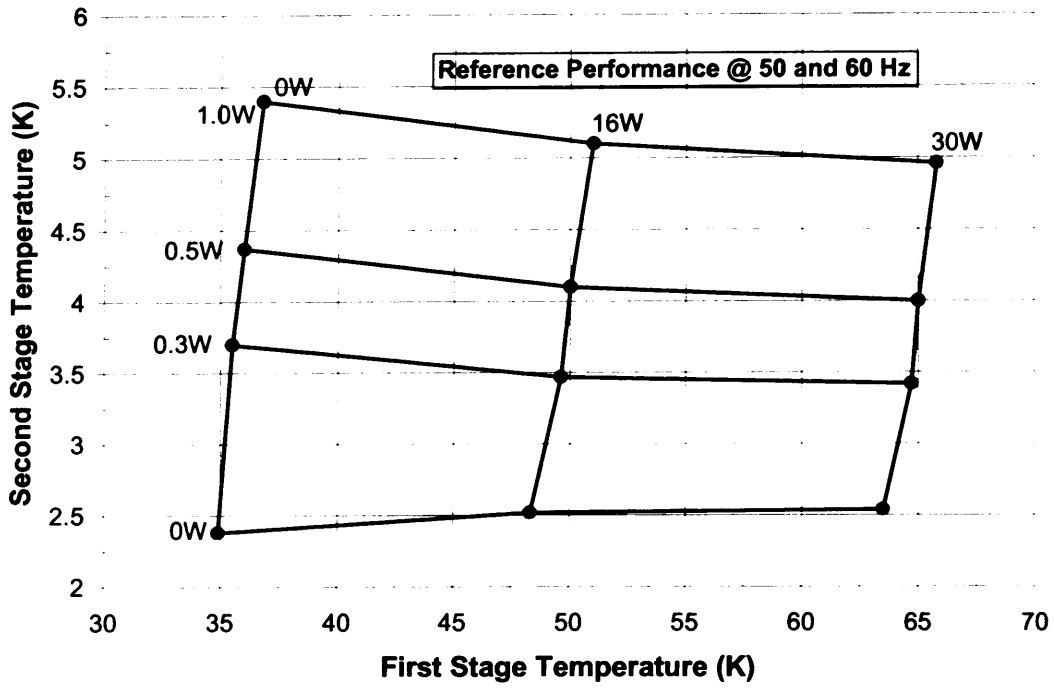

FIGURE 3.1: Cryomech PT405 cooling power for varying 1st and 2nd stage temperatures/heat loads.

stage can be estimated if the load or temperature is known for the first stage and vice versa.

VERICOLD PRK4 SPECIFICATIONS

The VeriCold's cold head weighs 13.6 kg and is 59 cm tall (36 cm cold finger length) and is therefore very similar in size to the Cryomech model. The thermal load diagram for the PRK4 is shown in Figure 3.2.

3.1.2 HELIUM-3 SORPTION REFRIGERATOR

The sorption refrigerator is pictured in Figure 3.3 with the main components labelled. The cold head is divided into two chambers so that the ^{4}He and ^{3}He never mix and the refrigerator is charged with 8 litres STP of ^{3}He and 20 litres STP of ^{4}He. With hindsight this is more than enough ^{4}He gas as is described below in subsection 3.1.3. The operation of the refrigerator follows the description in subsection 1.5.1. In addition, the heat exchanger precools the ^{3}He gas using the enthalpy of the ^{4}He vapour, during the ^{3}He condensing/^{4}He pumping stage of the cycle.

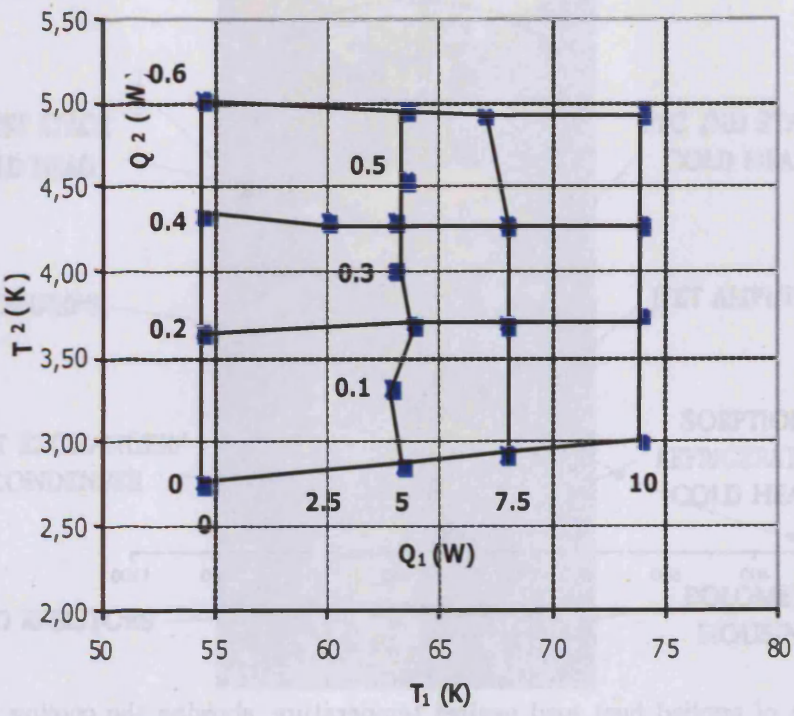

FIGURE 3.2: VeriCold PRK4 cooling power for varying 1st and 2nd stage temperatures/heat loads.

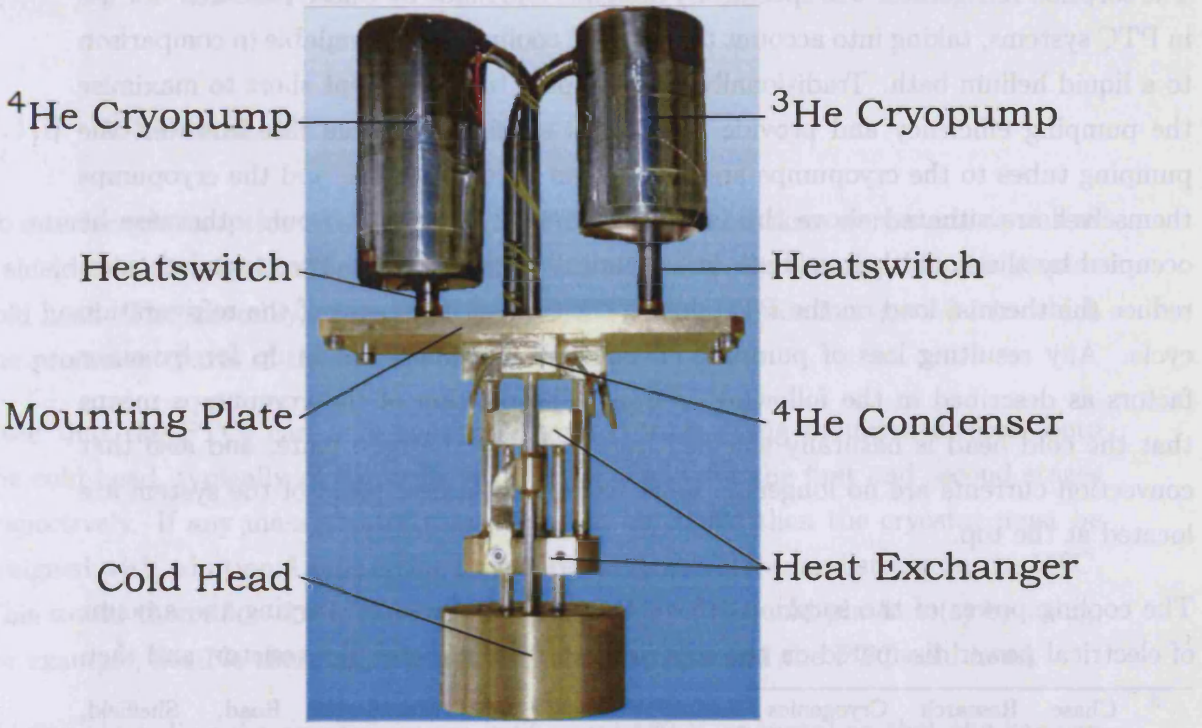

FIGURE 3.3: Two-stage sorption refrigerator. See text for details.

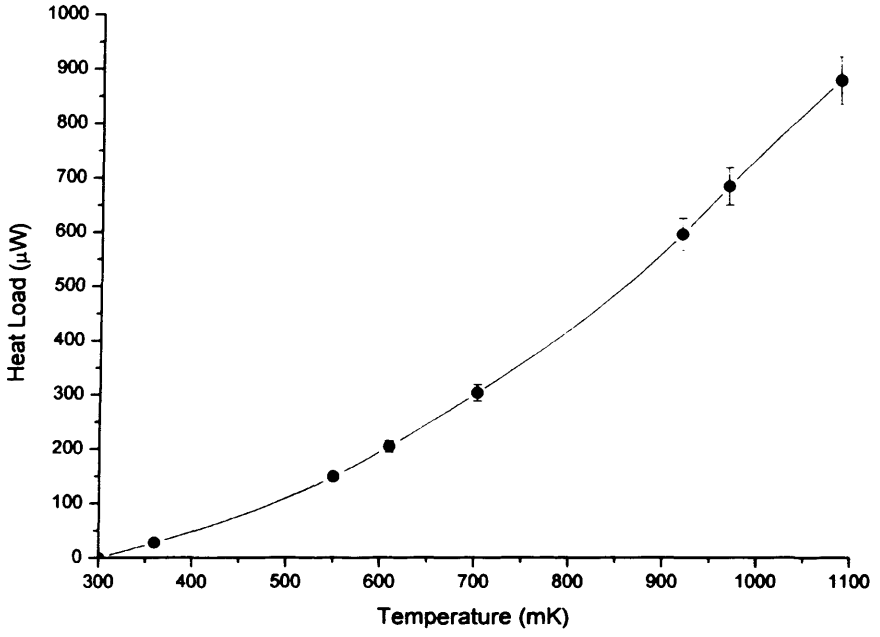

FIGURE 3.4: A plot of applied heat load against temperature, showing the cooling power for the two-stage sorption refrigerator cold head. Errors in the heat load arise from the uncertainty in the value of the metal film resistor used as a heater.

The sorption refrigerator was specifically designed and made by Chase Research[3] for use in PTC systems, taking into account the reduced cooling power available in comparison to a liquid helium bath. Traditionally, the pumping tubes are kept short to maximise the pumping efficiency and provide mechanical strength. In this case however, the pumping tubes to the cryopumps are longer than is conventional, and the cryopumps themselves are situated above the mounting plate in space that would otherwise be occupied by the liquid helium bath in a standard 'wet' cryostat. The extended tubes reduce the thermal load on the PTC during the condensing stages of the refrigeration cycle. Any resulting loss of pumping efficiency is more than made up for by other factors as described in the following section. The position of the cryopumps means that the cold head is naturally shielded from them by the base plate, and also that convection currents are no longer an issue since the warmest parts of the system are located at the top.

The cooling power of the sorption refrigerator was measured by varying the amount of electrical power dissipated on the cold head through a metal film resistor, and then

[3] Chase Research Cryogenics Ltd., Uplands, 140 Manchester Road, Sheffield, S10 5DL, UK. Telephone: +44 (0)114 268 0672, Email: info@chasecryogenics.com, Web: http://www.chasecryogenics.com

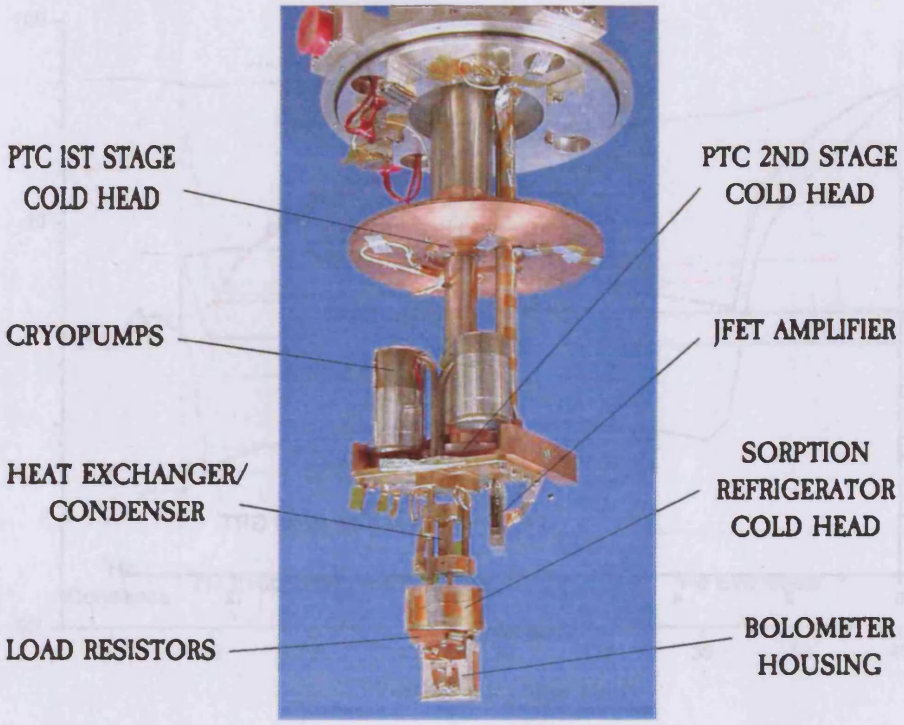

FIGURE 3.5: Cryomech PTC with sorption refrigerator mounted.

allowing the temperature to stabilise for each heat load. The results are shown in Figure 3.4.

3.1.3 OVERALL PERFORMANCE

To interface the sorption refrigerator to the PTCs, simple brackets were made as well as a shield that attached to the refrigerator's base plate to cover the sorption refrigerator cold head. The assembly, using the Cryomech PTC, can be seen in Figure 3.5 in which the prominent parts of the system have been labelled.

Note that the PTCs can only support a limited mass being mounted directly onto the cold head, typically of the order of 10 kg and 5 kg for the first and second stages respectively. If any mass greater than this is to be cooled then the cryostat must be designed with additional supporting structures to relieve stress and strain on the PTC. This would then allow for further vibration isolation of the cold platform(s) by using, for example, flexible thermal links between the platform and the PTC cold head.

During precooling the cryopumps are kept warm (30 K or more) so that the gas can circulate within the sorption refrigerator, helping the otherwise thermally isolated cold

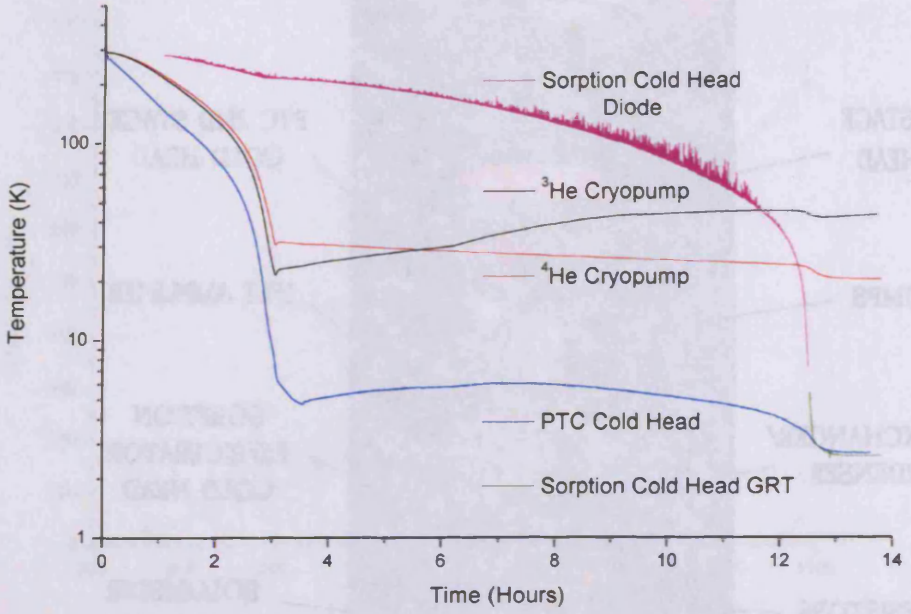

FIGURE 3.6: Temperature-time plots for the hybrid system's components during precooling.

head to cool. This happens naturally with this hybrid system because of the rapid cooling of the PTC. The heat switches turn off when the PTC reaches its base temperature and the cryopumps are thermally isolated before they thermalise fully with the PTC. This is another advantage of the extended pumping tubes. A small amount of power is applied to the cryopump heaters to maintain a temperature of more than 30 K during precooling nevertheless, and this also helps the cycling of the refrigerator to begin quicker. The precooling stages for the system are shown in Figure 3.6. A diode was used to monitor the sorption cold head temperature down to about 7 K, at which point it was turned off to avoid any unwanted thermal load. It can be seen from Figure 3.6 that precooling the sorption refrigerator requires approximately 12.5 hours.

Once the cold head temperature has stabilised with that of the PTC, the sorption refrigerator cycle can begin as shown in Figure 3.7. Note that usually some time is given for the ^{4}He to condense and then the cryopump is simply cooled from whatever temperature it levels out at during pre-cooling (usually 30–35 K). In Figure 3.7 however, the cycle was carried out like it would be in a conventional 'wet' cryostat as this was the first cycle attempt. Hence the ^{4}He cryopump was heated up to just over 50 K and left for about 10 mins. This condensing phase turned out to be too efficient and too much ^{4}He was condensed — the liquid ^{4}He charge lasted much longer than is necessary for the condensation of the ^{3}He gas. The lower base plate temperature (below 3 K)

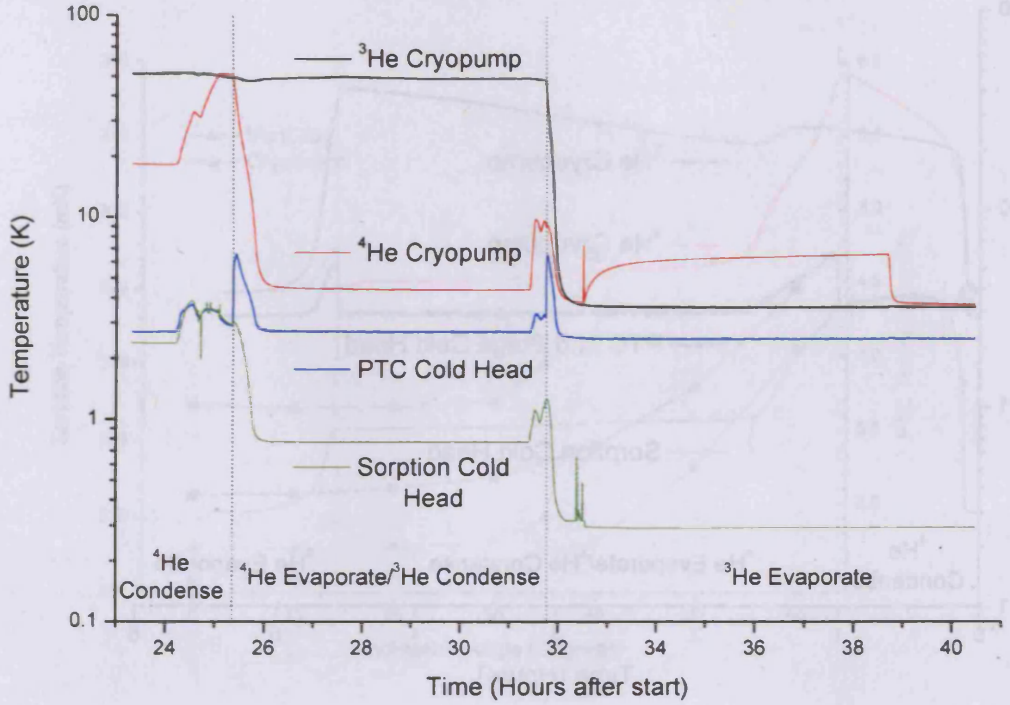

FIGURE 3.7: Temperature-time plots for the sorption refrigeration cycle carried out after precooling.

is also of great significance for the efficiency of the cycle. A lower temperature not only makes the ^{4}He charge last longer, it also means that the ^{3}He condenses at 0.8 K instead of above 1 K. In this cycle the sorption cold head was eventually heated slightly to remove the remaining ^{4}He, as can be seen by the unusual rise in temperature just before 32 hours in Figure 3.7.

One of the main considerations when cycling a PTC cooled sorption refrigerator is the heat load put onto the PTC during the pumping stages of the cycle. It was initially planned that the gas-gap heat switches could be turned partially on, by applying a lower voltage to their own cryopumps, to avoid giving too much heat load to the PTC at any one time. So long as the PTC cold head remained below about 15 K, so that the other heat switch remained in its 'off' state, then it would be acceptable provided the PTC could recover quickly. It turned out that the PTC could cope with the heat switches being switched fully on from the start, with the heat load spike only taking the Cryomech PTC cold head to just above 6.1 K for the ^{4}He cooling stage and 5.4 K for the ^{3}He cooling stage. The load diagram provided by Cryomech (Figure 3.1) indicates that the corresponding heat loads for these temperatures are approximately 1.5 W and 1 W respectively, while the mean electrical power input during the cycling of the sorption refrigerator is 160 mW. The PTC cold head returned to below 3 K in 40 minutes for

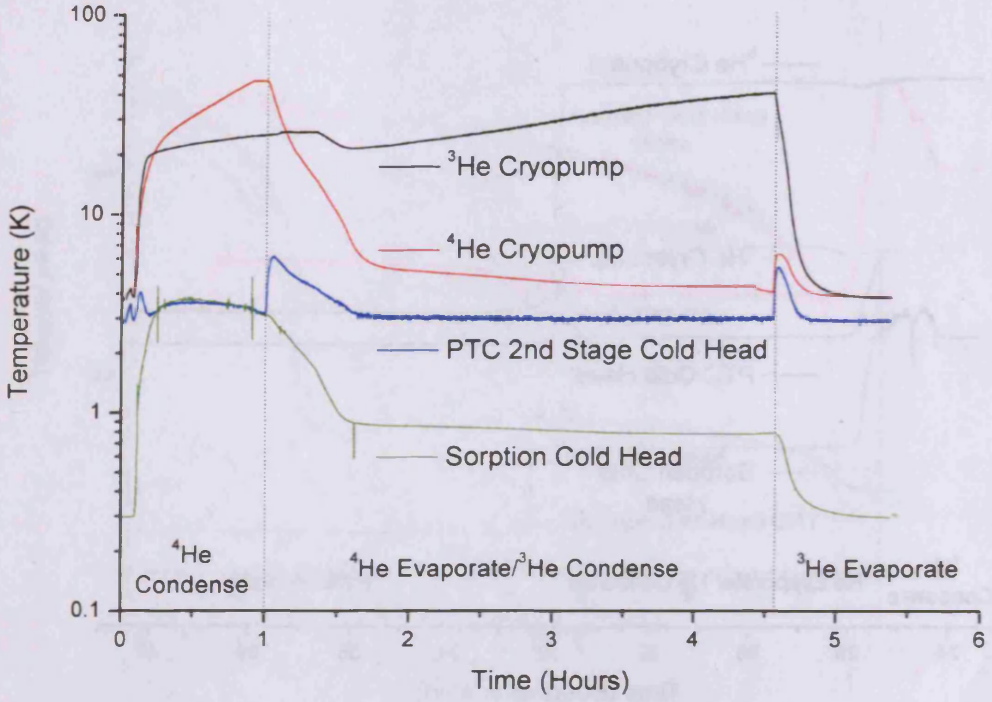

FIGURE 3.8: Temperature-time plots for the sorption refrigeration cycle carried out from 'cold'.

the ^{4}He stage and 10 minutes for the ^{3}He stage. The condensed ^{3}He charge maintains a temperature of 300 mK for approximately five days if left undisturbed.

Figure 3.8 shows a sorption refrigeration cycle carried out when the system is 'cold', in which case the cryopumps are heated rapidly to begin with. The whole cycle takes about 5 hours giving a duty cycle of over 95%. However, this is by no means a fully optimised cycle routine, having been designed for the automated system described in subsection 3.2.1, and it is possible to perform less efficient quick cycles if desired[4].

The sorption refrigerator has been designed to operate in any orientation after cycling. However, PTCs do operate best in the vertical position shown in Figure 3.5. Both systems were tested under an increasing angle of inclination to represent ground-testing for space applications and also the possibility of operating on a ground based telescope mount. The performance of each system is shown in Figure 3.9. In both cases it seems that the sorption refrigerator cold head simply follows the response of its base plate temperature (the PTC 2nd stage cold head). The VeriCold PTC however, took much longer to reach an equilibrium state after each increase in inclination, and also appears to have a minimum 'cut in' angle after which its performance is compromised. However, once the inclination does begin to affect the VeriCold it suffers more than

[4] The quickest being to just condense the ^{3}He straight away.

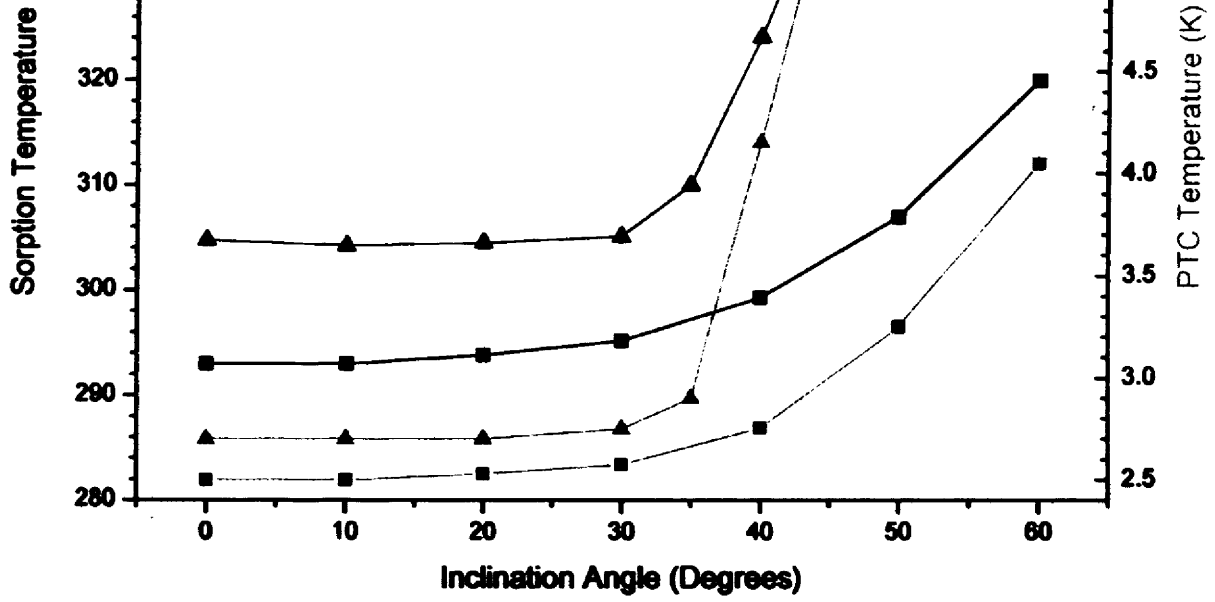

FIGURE 3.9: Cryogenic performance under inclination. Traces are shown for both the V cold and Cryomech second stage cold heads, and for the sorption refrigerator cold head w mounted in each system.

the Cryomech; the VeriCold was only inclined up to 45° and was already above 5 whereas the Cryomech was inclined up to 60° and remained below 5 K. Some of t difference in performance may be due to the slight differences in the two pulse tub geometry, such as the angle between the first and second stages.

3.2 ELECTRONICS

Two electronics systems were required for use during these investigations. The first v concerned with the 'housekeeping' — monitoring of the temperatures of the vari stages of the cryogenics system and the cycling of the sorption refrigerator. The secc system was to operate and read an NTD-Ge bolometer. Both of these systems described in this section.

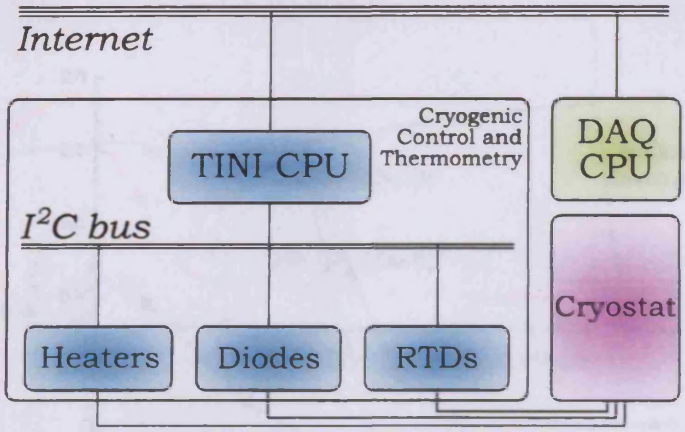

FIGURE 3.10: Schematic of the cryostat data acquisition system.

FIGURE 3.11: Cryogenic Control and Thermometry unit front panel.

3.2.1 CRYOGENIC CONTROL AND THERMOMETRY

During this work a system was being developed by QMC Instruments[5] that would enable an experiment to be monitored and run over an internet connection. Not only would the instrument allow the experimentalist to be situated away from their equipment, which in the case of a mechanical cooler can be fairly noisy, but the onboard computer could also be tasked with running sub-systems automatically. Combined with a mechanical cooler, this 'Cryogenic Control and Thermometry' unit results in a 'turn key' operated system, thus broadening the accessibility of very low cryogenic temperatures in the scientific community. This would then naturally benefit all fields of low temperature research and in particular those of low temperature physics.

The opportunity was taken to assist with the development of the Cryogenic Control and Thermometry unit and I assembled a prototype unit to be used with the PTC-sorption cooler system. A schematic breakdown of the unit and how it relates to the overall data acquisition of the cryostat is given in Figure 3.10, while Figure 3.11 shows the front panel for the unit.

[5] QMC Instruments Ltd., School of Physics and Astronomy, Cardiff University, 5 The Parade, Cardiff, CF24 3YB, U.K.. Telephone: +44 (0)29 2045 1071, Fax: +44 (0)29 2045 1271, Web: `http://www.terahertz.co.uk`

TINI CPU

The onboard CPU was provided by a TINI platform from Maxim[6] and is the key component for making the cryogenics system fully automated. The Tiny InterNet Interface microcontroller, as its name suggests, includes its own web server so that users can access the data collected from the I^2C bus that interlinks the various components of the unit. The experimenter can therefore perform their measurements remotely. Various XML tags are defined for use in scripts that can automate many of the tasks of running a cryogenic experiment. Users can upload their script via the TINI's own FTP server. An example XML script to cycle a two-stage sorption refrigerator is shown in Appendix C. Using this script with the previously described PTC-sorption refrigerator system means that 300 mK can be obtained within 24 hours at the push of a button.

DAQ CPU

The data acquisition computer runs a client to collect and log data from the TINI. The computer then converts the collected data to temperatures using the sensor calibrations and plots the results with suitable software. The clients use Open Source libraries and currently have versions for Linux and Windows.

3.2.2 NTD-Ge Bolometer Readout

Two methods of reading a bolometer with current biasing have been introduced in subsection 1.6.4; a basic DC readout, and a differential (AC) readout. There is no advantage in using a DC readout besides its simplicity. At the outset of this work it was believed that the use of AC rather than DC detector operation would lead to a significant immunity from microphonic and EM pickup (see chapter 2), because of the increase in common mode rejection. A DC readout is still required for characterisation however, and so I assembled a biasing and readout system that could use either AC or DC. The different stages of the NTD-Ge bolometer readout are show in Figure 3.12.

The stages of the readout were shared amongst three units:

- a JFET module installed inside the cryostat,

[6] Maxim Integrated Products Inc., 120 San Gabriel Drive, Sunnyvale, CA 94086 USA. Email: info2@maxim-ic.com, Web: http://www.maxim-ic.com/

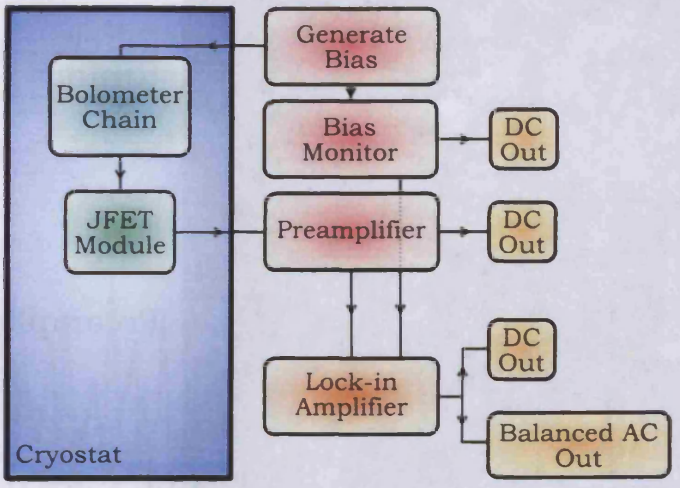

FIGURE 3.12: Stages of NTD-Ge bolometric detector readout.

- a box attached to the side of the cryostat containing the warm preamplifiers, JFET power supplies and bias generation circuits,
- and an instrument-rack mounted box containing the LIAs, readout power supplies, and collecting the various outputs.

BIAS GENERATION AND WARM AMPLIFIER

The main PCB, pictured in Figure 3.13, generates the bias voltage with a monitor output, the JFET power, and contains the room temperature preamplifiers. It is adapted from a *Bolocam* bias board and has had three of the six original bias monitors converted into preamplifiers, giving three channels as a result. *Bolocam* is a millimetre camera for the Caltech Submillimetre Observatory that has 119 working NTD-Ge bolometers. It has been used to observe star-forming molecular clouds, galaxy clusters and the CMB [43]. Also labelled in Figure 3.13 are the filter and bias controls, the power supply regulators, and the connections to the cryostat and the LIAs.

The bias generator produces a sinusoidal bias by first turning the DC bias level into a square wave, and then passing this through two narrow band-pass filters to remove harmonics and leave the desired frequency. The bias produced is low noise and very stable, making it good for the running of an observational experiment since there will be less systematic error occurring from a drift in the bias. The circuit was not designed for carrying out AC load curves however, and so some modification had to be made as described below. A ramp generator is included on the PCB alongside the bias generator to assist with load curve measurements. There is also the provision of an

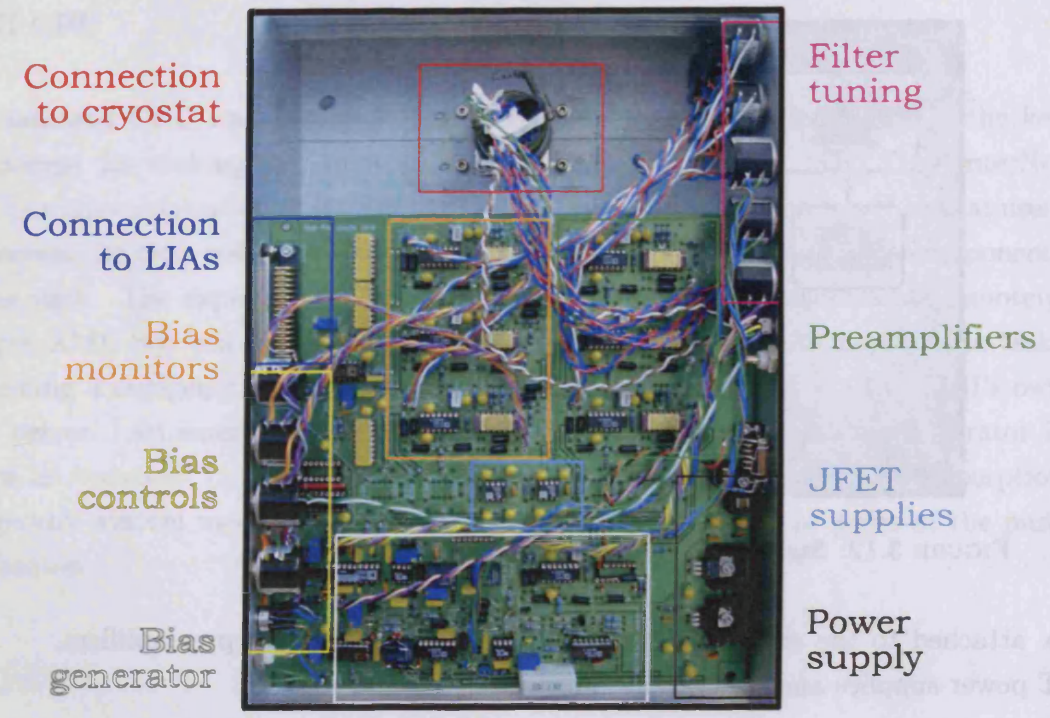

FIGURE 3.13: Cryostat mounted bolometer readout box. Contains the bias generator, bias monitors, JFET power supplies, and the room temperature preamplifiers.

external source input for the bias to allow use of a programmable power supply.

The AC bias can be selected to run at a frequency between approximately 120 and 250 Hz, however the band-pass filters in the electronics need to be manually tuned whenever the frequency is changed. This frequency range was found to be too limiting when investigating capacitive effects during the characterisation of the NTD-Ge bolometer, leading to the modifications described below.

The circuit diagrams for the original *Bolocam* bias board can be found in Appendix D, however several modifications were made to these. The main ones are as follows:

- Three of the bias monitor preamplifiers had their feed resistors removed to turn them into signal preamplifiers.
- The auto-zero filter on the AD624 output in the preamplifier was removed in order to give a true DC output.
- To give greater flexibility with the AC biasing, the external bias input was linked to beyond the band-pass filters of the internal bias generator so that an external sinusoidal input could be provided instead of a DC one. This does not affect the internal DC biasing circuit.

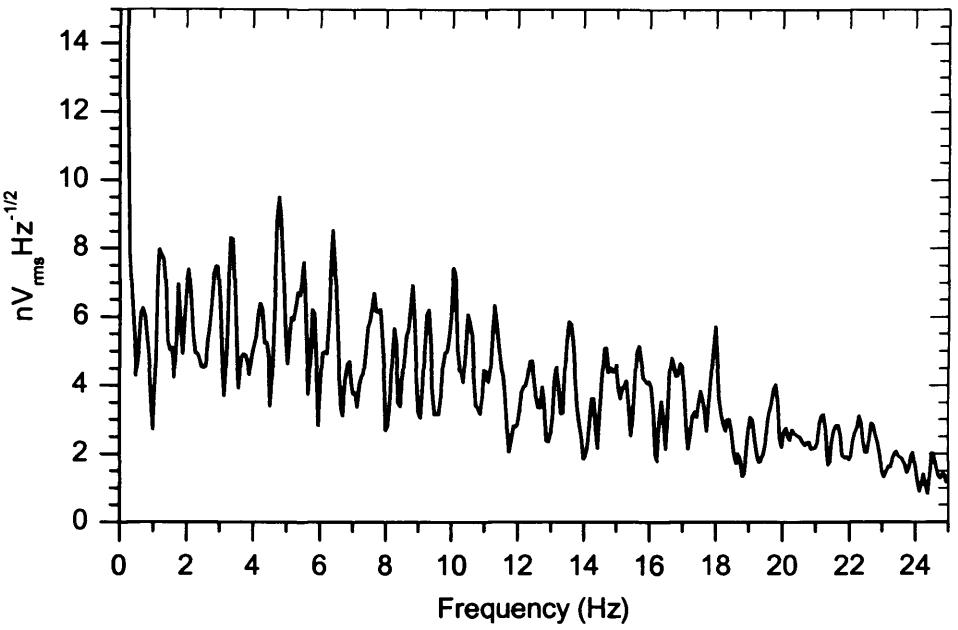

FIGURE 3.14: Input shorted warm amplifier and LIA noise. The roll-off is due to the LIA's low pass filter.

The gain of the DC output is 100 for the bolometer signal and unity for the bias.

LOCK-IN AMPLIFIER

The LIAs were housed in the instrument-rack box along with the power supplies for the readout. This unit also provided the access points to all of the outputs of the system. The DC output of the LIA has an overall gain of 136, while the balanced AC output has a gain of 1.36×10^4. The input shorted noise for the combined warm amplifier and LIA is shown in Figure 3.14.

COLD (JFET) AMPLIFIER

An NTD-Ge bolometer has an impedance of several MΩ at 300 mK and therefore requires a cold JFET stage to convert to a lower output impedance for coupling to the next stage of amplification, and to reduce microphonic pickup. The JFET module used has six channels allowing for additional test setups such as a dummy resistor and an NTD-Ge thermometer. Each channel uses a matched JFET pair[7] as part of the AC

[7] InterFET IFN146

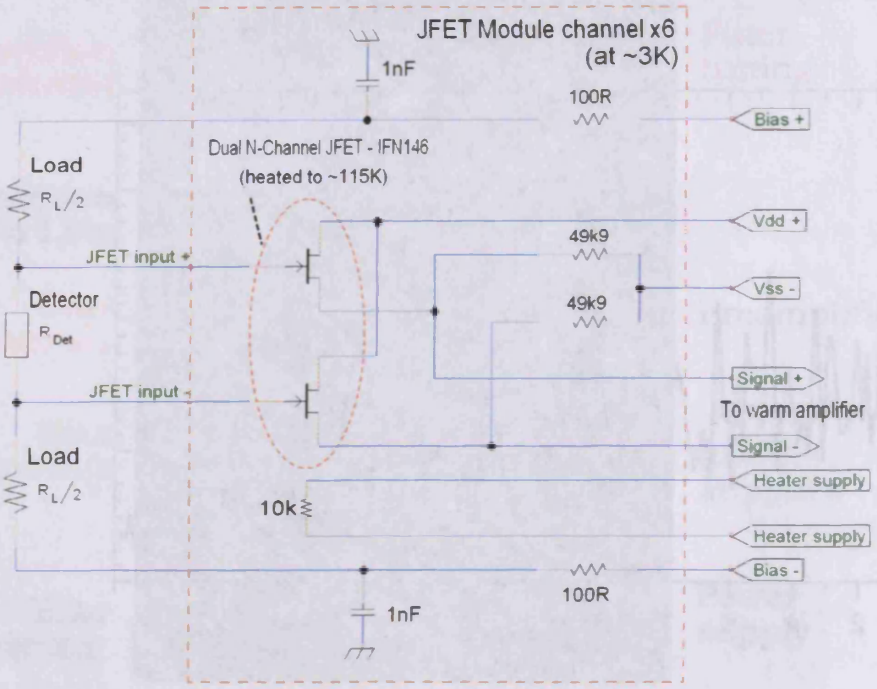

FIGURE 3.15: Cold electronics for NTD-Ge bolometer readout.

biased differential readout scheme and, contrary to its name, has unity gain.

The circuit details of the JFET module together with the rest of the cold electronics is shown in Figure 3.15. The JFETs themselves are on an isolated section of PCB, pictured in Figure 3.16, which is heated to 115 K. This is necessary in order that the charge carriers are not frozen out; 115 K is chosen as the optimum temperature for the lowest noise given by the JFETs. The narrow supports of PCB act as a very weak thermal link to the JFETs and the electrical power dissipated to keep them at 115 K is just under 40 mW.

Given that the JFETs are heated up to 115 K it is usual to mount the module on the liquid helium stage of a conventional cryostat, since this temperature would overload the cooling capacity of the 300 mK sorption stage and could also give a significant stray radiation load on the bolometer. The bolometer block, load resistor pack (both mounted on the 300 mK stage) and the JFET module (mounted on the 3 K stage) can be seen in Figure 3.5.

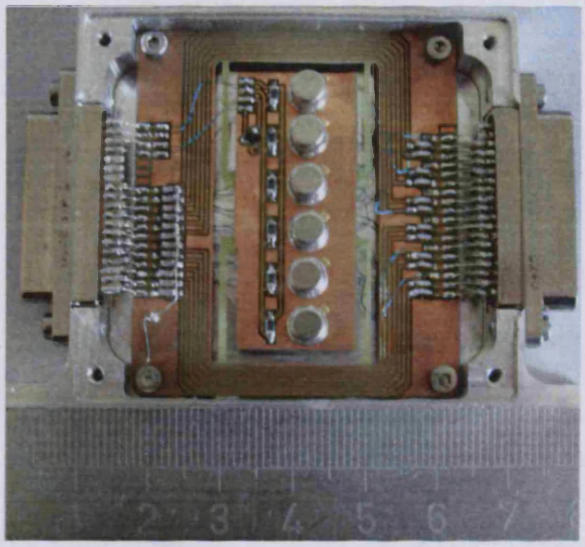

FIGURE 3.16: JFET module opened up to reveal the island of PCB where the JFETs are situated (actual size).

PREAMPLIFIER NOISE

The warm and cold preamplifiers of the readout contribute to the overall noise performance of the bolometer as described in subsection 1.6.3. The JFET amplifier contributes both current and voltage noise, whereas with the warm amplifier only the voltage noise is significant because of the down conversion to a lower impedance (*cf.* Equation 1.15). The voltage noise contributions are 4.75 and 0.35 $nV_{rms}Hz^{-0.5}$ for the warm and cold preamplifiers respectively. The current noise contribution from the JFET stage depends on the operating temperature of the bolometer but is between 2 and 4 $nV_{rms}Hz^{-0.5}$.

3.2.3 GROUNDING

The system as a whole followed a 'star' grounding scheme where possible, with individual items being grounded at the same single point. The exception was the compressor unit for the Cryomech which is not electrically isolated from the pulse tube assembly, and therefore the cryostat also, and has its own grounding via the three-phase socket (See Figure 3.17). The VeriCold's compressor was also initially in electrical contact with the cryostat, however work was later carried out on the pulse tube assembly to insert an electrical break at the connection to the rotary valve.

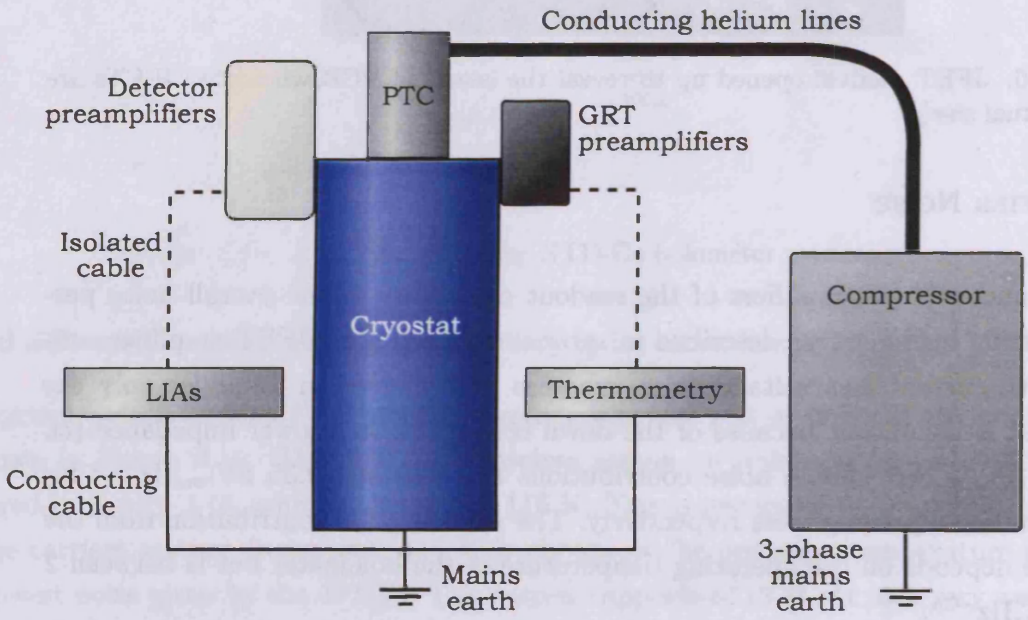

FIGURE 3.17: Grounding schematic for the PTC cryostat.

Chapter 4

300 mK NTD-Ge Bolometer Tests

This chapter concerns the tests carried out to investigate the performance of an NTD-Ge bolometer operated on the cold head of the PTC precooled ^{3}He sorption refrigerator. The tests also involved noise measurements of high impedance resistors to help identify and locate electrical pickup and problems with the wiring configuration/readout. Much of this work was done under contract from the European Space Agency (ESA).

4.1 Bolometer Description

The NTD-Ge mesh bolometer used during these tests was designed and made by Orlando [1], and has similarities with those being used for the non polarisation sensitive part of the *Planck* mission [32] and those developed by Bock *et al.* [44]. The NTD-Ge chip is bonded to a Si_3N_4 mesh and has two superconducting niobium wires attached with indium solder, unlike the more sophisticated kind mentioned above that have their electrical leads deposited directly onto the Si_3N_4 mesh. The bolometer is pictured in Figure 4.1 with its main parts labelled.

NTD-Ge mesh bolometers are used for submillimetre and millimetre observations in astronomy and earth observations (wavelengths roughly between 200 and 2000 μm). Sensitivity to certain wavelengths of radiation is determined by the mesh spacing in the case of a micromesh bolometer. Given the wavelength range it follows that the astronomical sources observed with such devices are those that are 'cool' in temperature, *eg.* the CMB, debris and accretion disks, dust, pre-stellar cores and protostars.

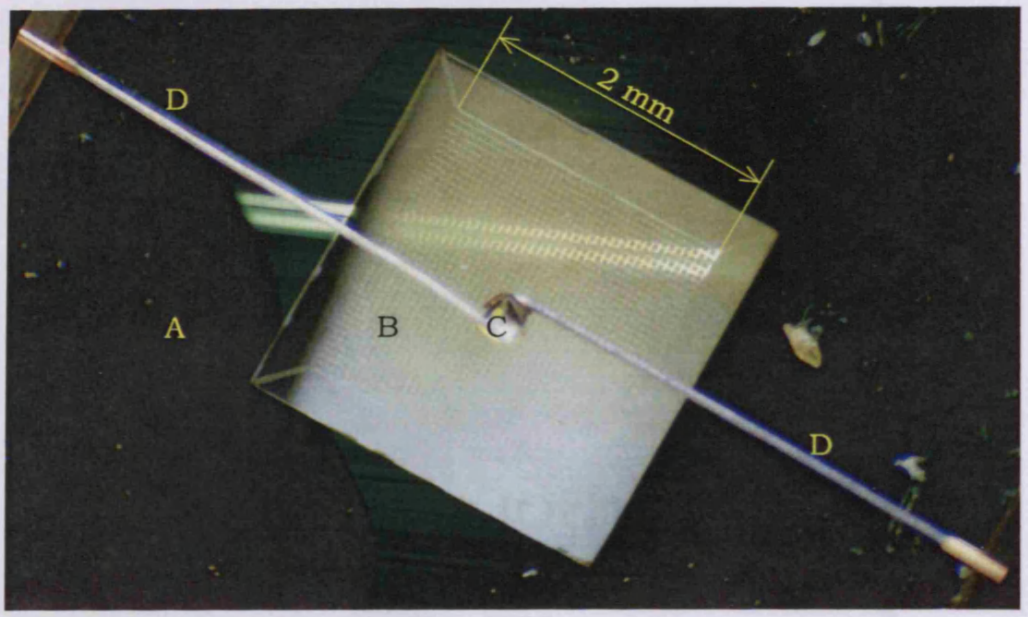

FIGURE 4.1: The 300 mK NTD-Ge bolometer (*cf.* Schematic shown in Figure 1.8). *A* — Silicon substrate; *B* — Si_3N_4 mesh absorber with 50 μm grid spacing and 4 μm leg width; *C* — NTD-Ge thermistor; *D* — Niobium leads with copper contacts bonded to *C* with indium solder.

Problems with the technology experienced in the past are due to their construction. The number of pixels in an instrument is limited since their manufacture cannot be automated, and in the past quite high failure rates of pixels have been known. Older absorber materials such as sapphire also meant the devices had low resonant frequencies, increasing the detrimental effect of microphonics.

Although newer, faster, and more sensitive types of bolometer are well into development (*eg.* low impedance superconducting Transition Edge Sensors), most current field instruments use the same NTD-Ge high impedance detectors as used in this study. It is also beneficial to use a technology that is fully understood so that the influence of the new cryogenics system is easier to interpret. The results of this study should allow current large array instruments to be operated without the incumbent of liquid cryogens at remote field sites. Many of the parasitic effects discussed here will also benefit experiments proposing newer detector technologies (TES) by raising awareness of thermal and EMI issues that need to be addressed.

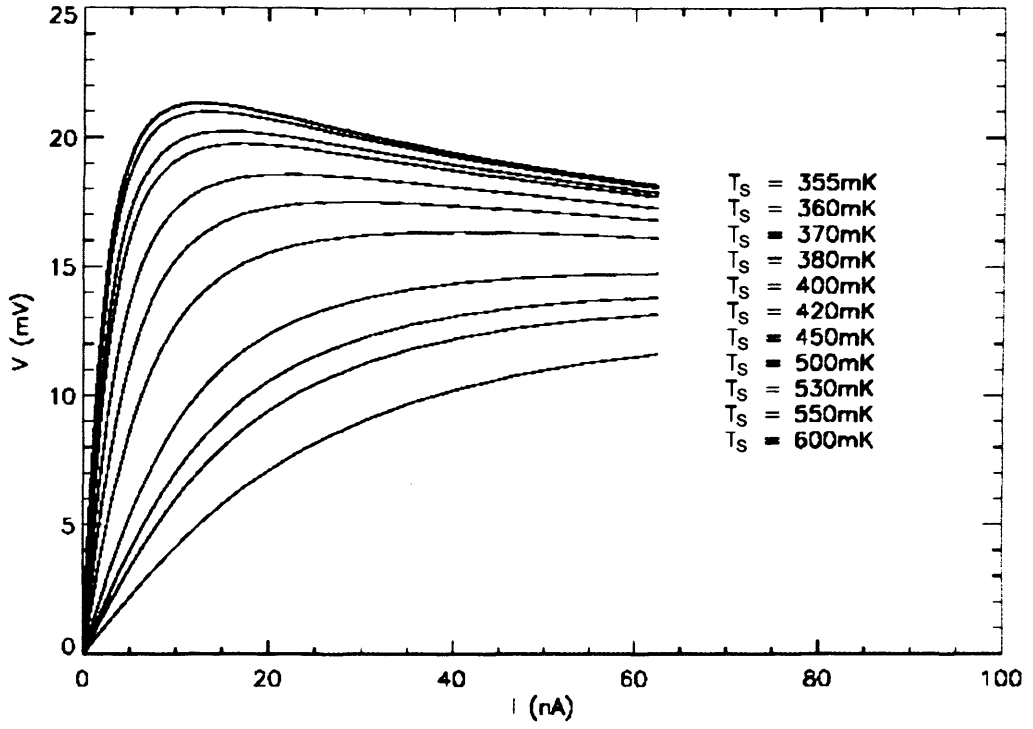

FIGURE 4.2: NTD-Ge bolometer V-I characteristics (load curves) measured for a set of heat sink temperatures, T_S, in a 'wet' cryostat [1].

4.2 BASELINE CHARACTERISATION

The bolometer was first characterised, using the model developed by Sudiwala *et al.* [33], in a conventional liquid helium ('wet') cryostat before installing it in the PTC-sorption refrigerator ('dry') cryostat. The characterisation process begins by taking a series of load curves, the voltage-current characteristics, of the bolometer at a range of heat sink temperatures and optically blanked off. This procedure enables us to find the resistance parameters R_* and T_g for the analytical equation fit to the temperature-resistance curve of the NTD-Ge thermistor (see Equation 1.17), by considering the 'zero-bias' resistance of each load curve. The family of load curves taken in the 'wet' cryostat is shown in Figure 4.2.

The 'zero-bias' resistances are found by measuring the gradients of the straight line portions of the load curves at the lowest bias current levels. At these low bias currents the self heating of the bolometer is insufficient to significantly raise its temperature above that of the heat sink, and so we can consider the resistance at this bias level to be the NTD-Ge chip's resistance at the heat sink temperature. Alternatively the chip can be separately characterised before the bolometer is constructed. A plot of $ln(R)$ against $1/\sqrt{T}$ is produced and a linear fit is performed to find the two resistance

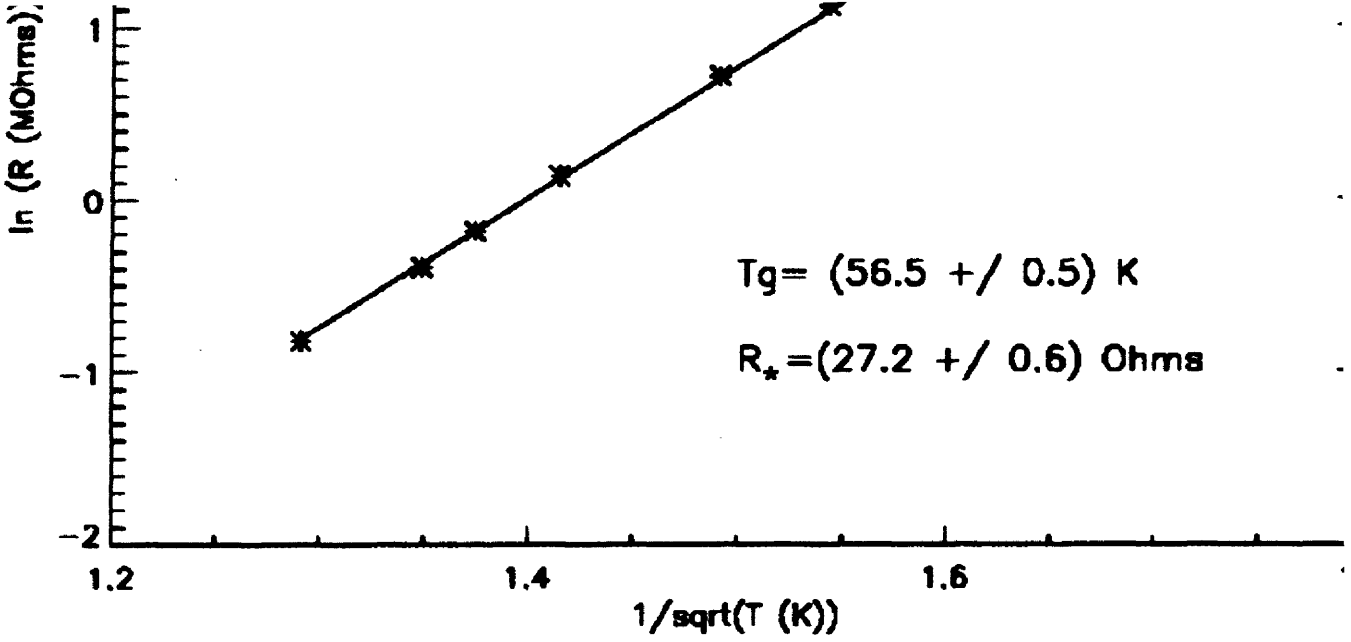

FIGURE 4.3: Natural log of the zero-bias resistance versus the inverse of the square the heat sink temperature for the NTD-Ge bolometer. A linear fit is performed to de the bolometer's resistance parameters [1].

parameters; $ln(R_*)$ being the y-axis intercept, and $\sqrt{T_g}$ being the gradient. Th fit for the data gathered from the load curves is shown in Figure 4.3 and the expo fit is compared to the experimental data on a linear scale in Figure 4.4. There is excellent agreement between the theory and the data.

The next stage of characterisation involves using the thermal model of the bolon find values for the average thermal conductance at the various heat sink tempe $\bar{G}_S$, and the material parameter, β. These two free parameters are used to load curve individually, as shown in Figure 4.5.

As previously mentioned in subsection 1.6.4, β should ideally be a single valu temperatures but varies in practice. This variation can be seen when Equati is fitted to the obtained values of $\bar{G}_S$ giving a best fit value of β. This fit is in Figure 4.6 and the resulting value of β was 1.7. Note that the small am variation in β is not significant when comparing the bolometer's noise performa various configurations later on, since this was done at an approximately consta sink temperature.

The speed of response of the bolometer was then measured by viewing an optical

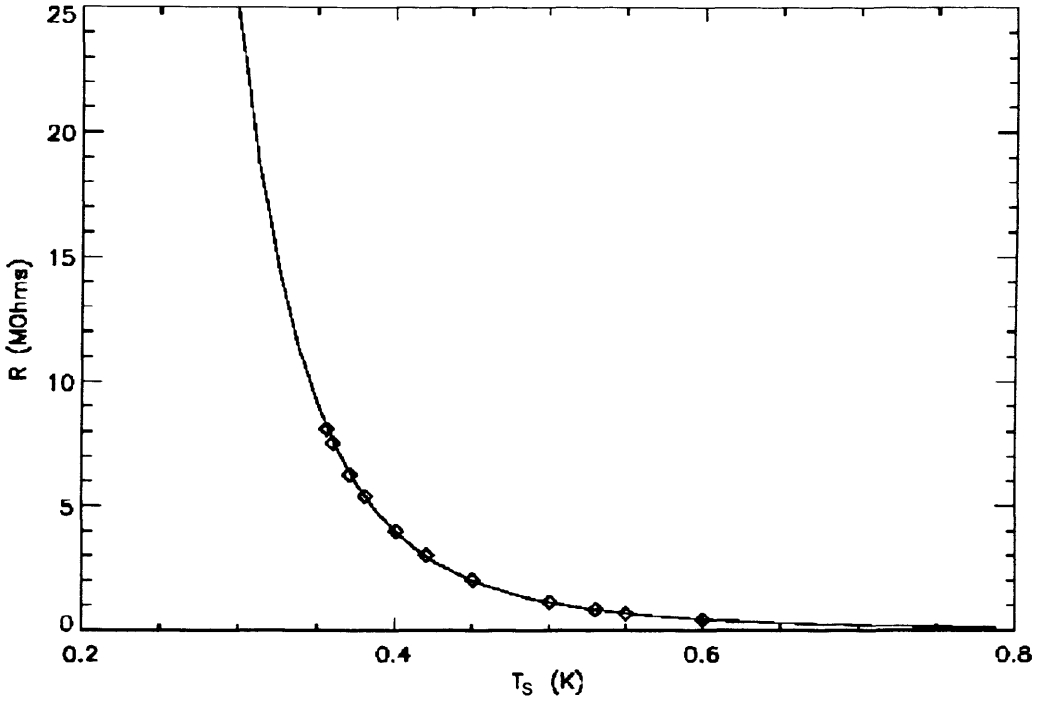

FIGURE 4.4: Resistance versus heat sink temperature of the NTD-Ge bolometer. The curve is given by the fitted resistance parameters and the points are the experimental data [1].

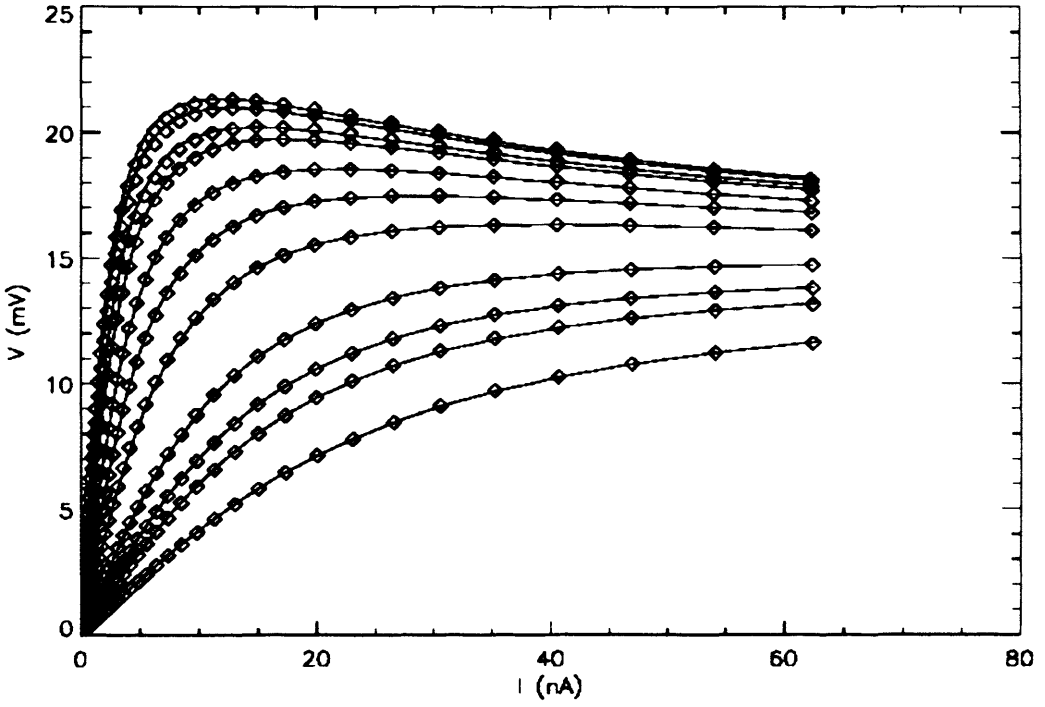

FIGURE 4.5: Fitted load curves for the NTD-Ge bolometer in the 'wet' cryostat (points — data, lines — theory) giving values for β and $\bar{G}_S(T_S)$ [1].

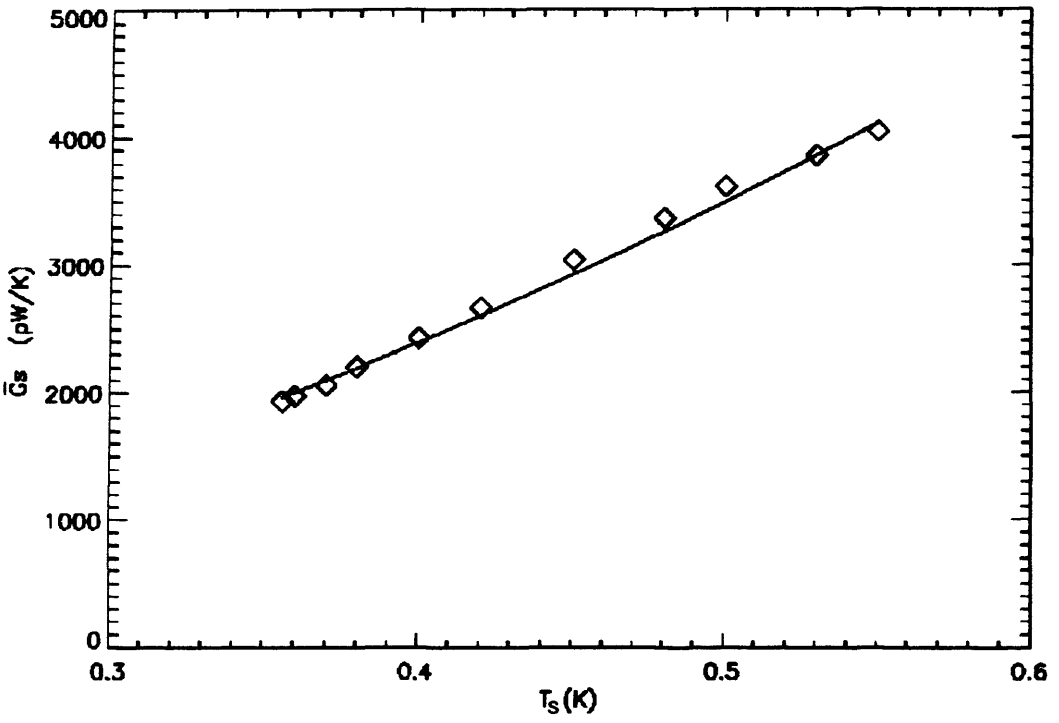

FIGURE 4.6: NTD-Ge bolometer's average thermal conductance against heat sink temperature with model fit (points — data, lines — theory) [1].

modulated at a suitable frequency. This was done at a single heat sink temperature and for varied bias levels. The optical time constant is obtained by observing the drop off in signal with increasing chopping frequency. The results for three bias levels around the optimum bias point (just above maximum responsivity where the NEP is minimum) are shown in Figure 4.7. These will later be compared with electrical time constant measurements taken in the 'dry' cryostat.

Finally, the quiescent voltage noise level for the bolometer was measured using a DC bias and readout. A baseline noise figure of 13 $nV_{rms}Hz^{-0.5}$ was obtained at a bolometer heat sink temperature, T_S, of 360 mK and with the bolometer optically blanked off. This is shown in Figure 4.8 for reference.

4.3 CHARACTERISATION USING PTC SYSTEM

The characterisation tests were repeated in the 'dry' cryostat to confirm that the bolometer's characteristics were unchanged, *ie.* its time constant and load curves at various T_S conformed to those obtained in the 'wet' cryostat. It was also a requirement that the noise response should return to that in the 'wet' cryostat when the PTC is

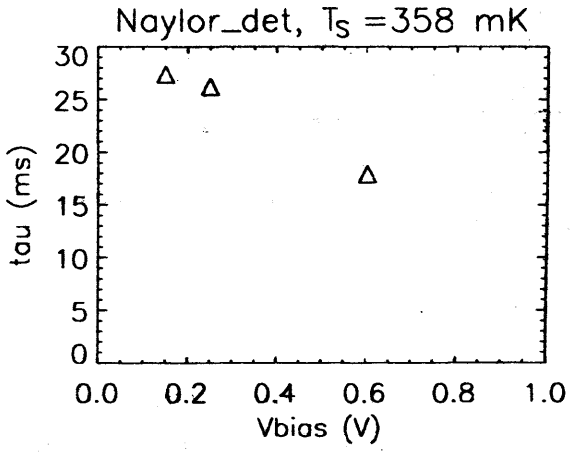

FIGURE 4.7: NTD-Ge bolometer optical time constants measured in the 'wet' cryostat [1].

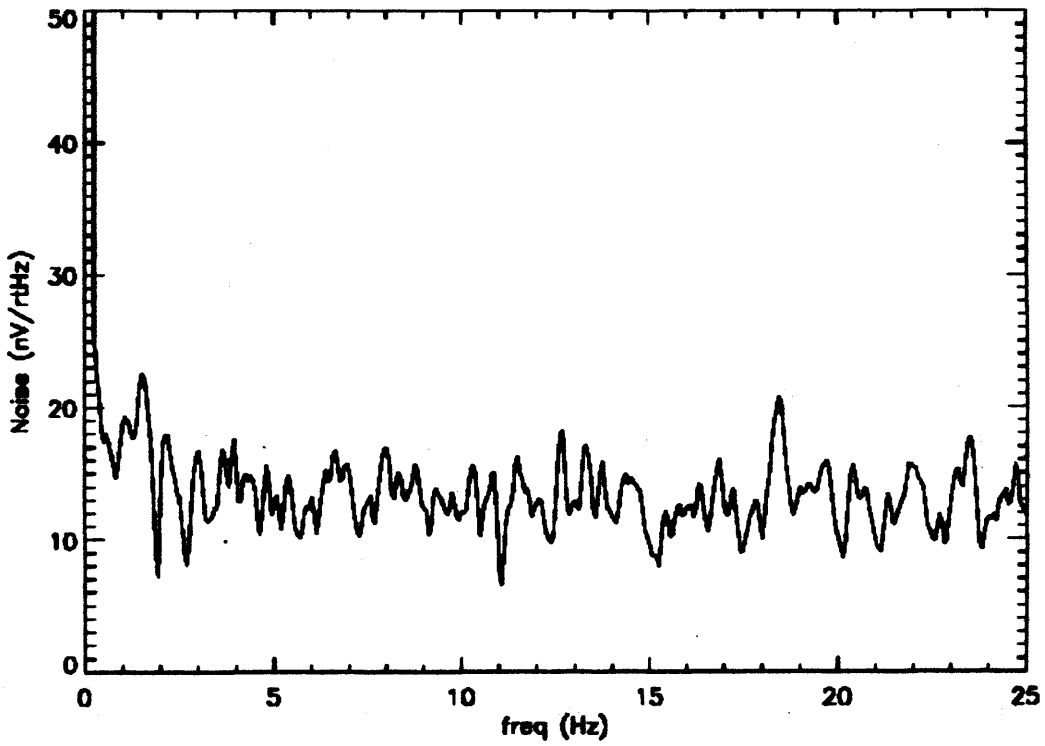

FIGURE 4.8: NTD-Ge bolometer DC noise response in a 'wet' cryostat [1].

T_S	360 mK	300 mK
Johnson	10.7	14.8
Phonon	9.5	16.9
JFET v_n	0.35	0.35
JFET i_n	2.06	3.97
Warm Amp. v_n	4.75	4.75
Total	15.2	23.3

TABLE 4.1: Table showing the voltage noise components for the bolometer operating at 360 and 300 mK. All values are in $nV_{rms}Hz^{-0.5}$.

turned off momentarily.

Better cryogenic performance compared to the 'wet' cryostat, due to the improved design of ^{3}He sorption refrigerator, meant that the bolometer was operated at a lower base temperature of 300 mK in the 'dry' cryostat. This leads to different levels of voltage noise from the various contributions, but these can be predicted from the characterisation data. Table 4.1 summarises and compares the noise contributions at 360 and 300 mK. It is seen that at the lower temperature the phonon noise begins to dominate. The Johnson and phonon noise are larger at the lower temperature primarily because of the increased responsivity of the bolometer, but also because of the NTD's higher impedance at this temperature.

4.3.1 Modelled and Measured DC Load Curves

Another series of load curves were measured with the bolometer optically blanked off and operating at a range of temperatures; approximately 300 to 360 mK. A DC bias was used to begin with. Using the characterisation data from the 'wet' cryostat, model VI load curves were produced for the bolometer operating at these lower temperatures. The model VI load curves fit well with those measured in the PTC cryostat, as shown in Figure 4.9.

4.3.2 AC Load Curves

Load curves were then taken using the AC biasing and readout system to ensure that the bolometer's behaviour remained the same under these biasing conditions. There were initially problems with AC readout system and bolometer wiring configuration which caused discrepancies between the AC and DC load curves.

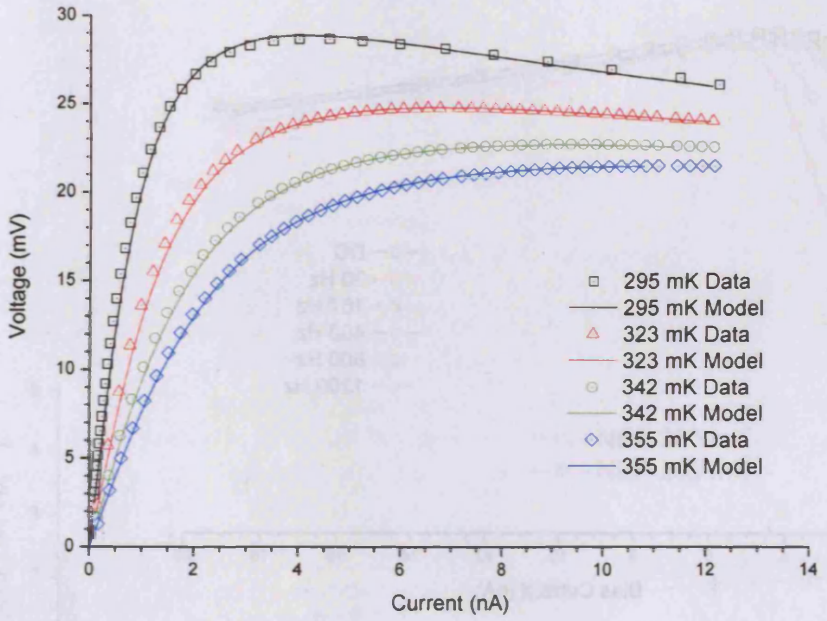

FIGURE 4.9: Load curves for the NTD-Ge bolometer with data taken in the PTC system and fitted with the thermal model characterised in the 'wet' cryostat for a range of temperatures.

It was at this point that the modifications described in the previous chapter were made to the readout electronics. In addition, the high impedance wiring between the JFET stage on the PTC cold head and the bolometer block on the sorption cold head was also reduced in length to its bare minimum. This was in order to reduce the capacitance between the four wires and the stray capacitance to ground. Originally a substantial length (~30 cm) of Constantan wire was used and most of this was wound around the sorption cold head for heat sinking. The reduced length was 15 cm.

The final AC and DC load curves are compared in Figure 4.10 for a range of bias frequencies and at a constant T_S of 297 mK. As expected, a capacitance in parallel with the bolometer causes the peak of the load curve to shift to higher bias currents for higher bias frequencies. Low frequencies match closely with the DC curve at low currents and the difference in peak amplitude was reduced to less than 1%. This is due to the drop off in the bolometer's frequency response which has not been calibrated out of the data. In any case, both methods give the same optimum bias region of between 2 and 4 nA where the NEP is minimum for the largest T_S used (355 mK).

Figure 4.11 shows the AC and DC responsivity curves as a function of bias current as well as the NEP for the minimum and maximum T_S. Since the ill-determined capacitance effects of the circuitry decrease with bias we note at optimum bias, between

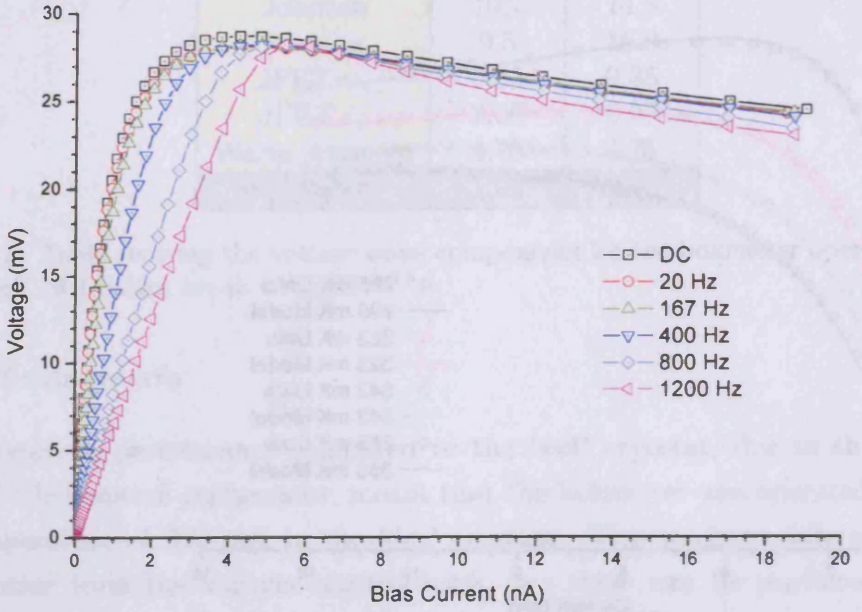

FIGURE 4.10: Comparison of AC and DC load curves of the NTD-Ge bolometer in the 'dry' cryostat, with varying bias frequency and constant heat sink temperature.

2 and 4 nA, the agreement between AC and DC values is good. This allows us to directly compare the system performance with either AC or DC readout.

One other problem encountered during the investigation into the AC readout was cross-talk between readout channels. The origin of the cross-talk was traced to the JFET module and occurred between adjacent channels. The problem was solved by using every second channel so that there were grounded tracks on the JFET PCB separating the channels that were in use. This was possible since the JFET module has six available channels compared to three in the room temperature electronics.

4.3.3 ELECTRICAL TIME CONSTANT

Originally it was intended to use an optical illuminator inside the cryostat to measure the optical response of the bolometer as one of the requirements for the ESA contract. Quite often however, the electrical response of the bolometer is very close to its optical response. To show the validity of this statement for this detector, the optical response data in Figure 4.7 was compared with data taken in the 'dry' cryostat and optically blanked off. The electrical measurements were made by recording the detector response to a step-change in the bias voltage.

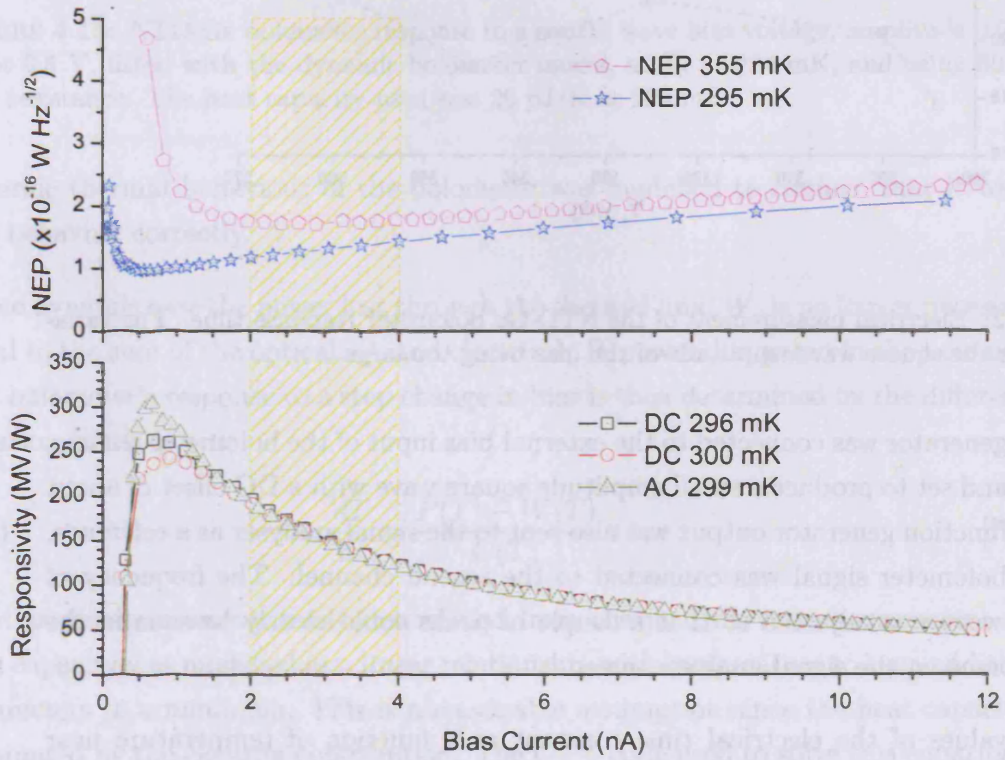

FIGURE 4.11: NTD-Ge bolometer's AC and DC responsivity in PT system and NEP versus bias current. The shaded area shows the optimum bias region between 2 and 4 nA where the NEP is minimum for the largest T_S used (355 mK).

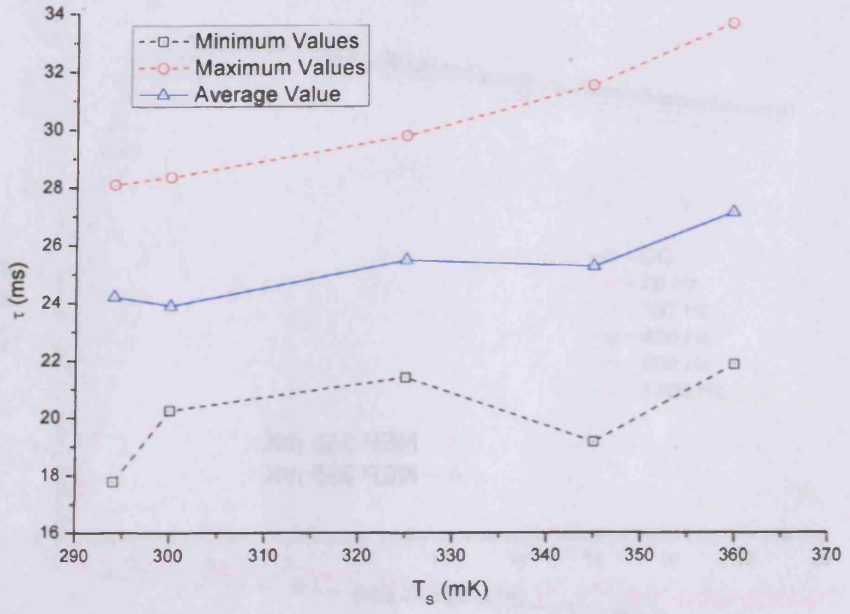

FIGURE 4.12: Electrical measurement of the NTD-Ge bolometer response time. The variation was due the square wave amplitude of the bias being too large.

A function generator was connected to the external bias input of the bolometer readout electronics and set to produce a small amplitude square wave with a DC offset of about 0.5 V. The function generator output was also sent to the signal analyser as a reference, whilst the bolometer signal was connected to the second channel. The frequency of the square wave was adjusted so that a couple of peaks could clearly be seen in the bolometer trace on the signal analyser screen.

To obtain values of the electrical time constant as a function of temperature near 300 mK the cold head of the adsorption refrigerator was heated. Traces of the bolometer's response to the step bias were recorded at ~20 mK intervals from 295 to 360 mK. The Hewlett-Packard sdf files were converted to text files for analysis. Straight lines were fitted to logarithmic plots of the decay curves to give the appropriate response times. It was discovered that the positive and negative steps gave two different time constants, differing by ~10 ms. Figure 4.12 shows the maximum, minimum and averaged values obtained for each temperature.

With hindsight it is believed that the amplitude for the function generator's square wave was set too large in respect to the offset. The effect of this is that the bolometer's operating point travels a significant distance on the load curve, and the effective time constant changes since the bolometer's heat capacity varies with temperature. The

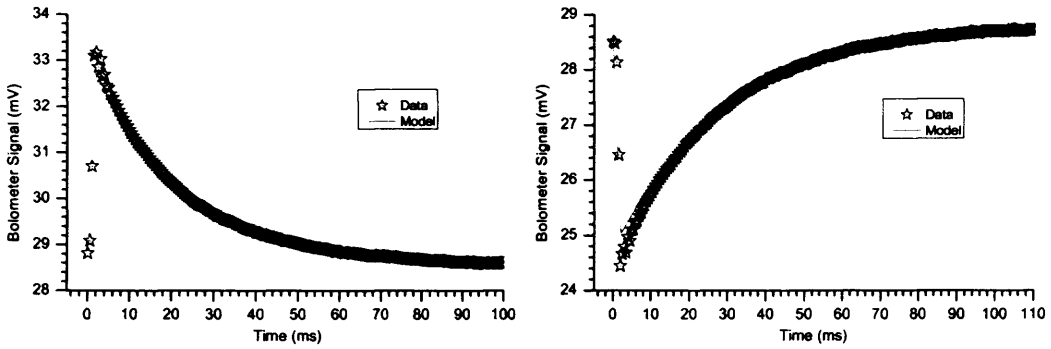

(a) Step up. (b) Step down.

FIGURE 4.13: NTD-Ge bolometer response to a square wave bias voltage, amplitude 0.07 V, offset 0.5 V, fitted with the dynamic bolometer model, at T_S = 294 mK, and using 80 MΩ load resistance. The heat capacity used was 26 pJ/K at 294 mK.

dynamic thermal behaviour of the bolometer was modelled to confirm that it was in fact behaving correctly.

In the dynamic case the power lost through the thermal link, W, is no longer necessarily equal to the sum of the optical, Q, and electrical, P, power dissipated in the bolometer. The bolometer's response to a step change in bias is then determined by the differential equation (with $Q = 0$),

$$\frac{dT}{dt} = \frac{P(T) - W(T)}{C(T)} \qquad [\mathrm{Ks}^{-1}] \tag{4.1}$$

Most parameters were already determined from the load curve measurements. The heat capacity was modelled as a linear relationship with temperature to keep additional parameters to a minimum. This is a reasonable assumption since the heat capacity is dominated by the electron contribution. The C++ code used to solve this equation for a step change in bias can be found in section B.2.

The model fitted the measured bolometer response well using a single value for the heat capacity, 26 pJ/K, at a specified temperature, 294 mK, except at the transition of the square wave (Figure 4.13). The discrepancy here, approximately 1 2 %, is believed to be due to the higher harmonics of the imperfect square wave producing a ringing in the bolometer signal. Figure 4.14 shows the corresponding path that the bolometer's signal takes (red arrows) on its load curve. At a step in the bias the bolometer follows the straight $V = IR$ line (green dashed lines) to a peak voltage (triangles) before relaxing back down, or up, to a position on the load curve line for the new bias level (blue dotted lines).

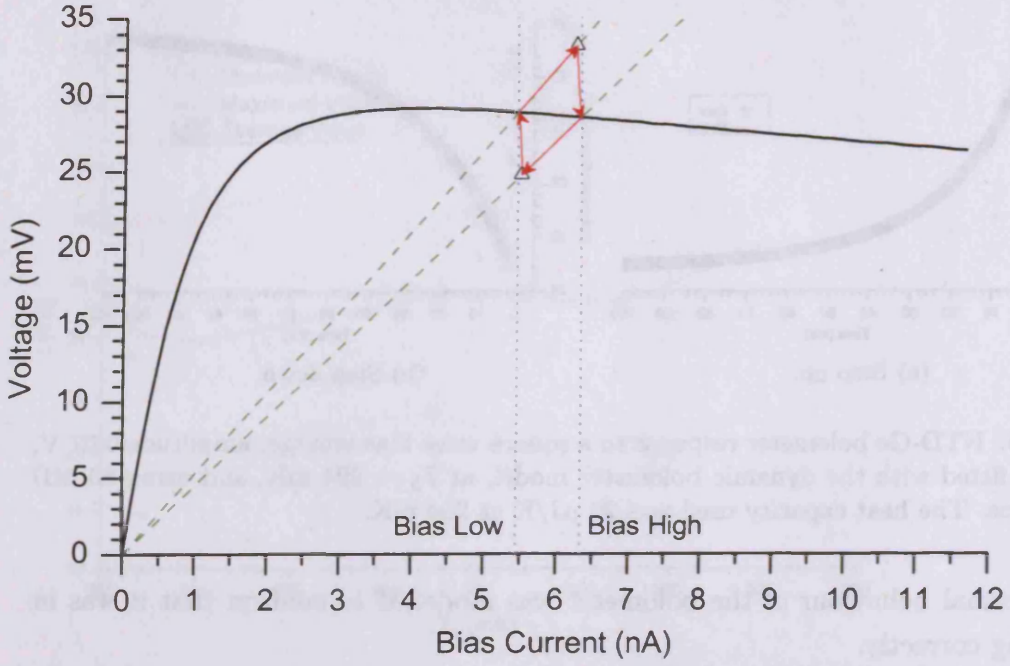

FIGURE 4.14: Path of the NTD-Ge bolometer's signal on its load curve in response to a square wave bias, at a T_S of 294 mK (shown by the red arrows). The blue dotted lines indicate the high and low bias levels of the square wave. The green dashed lines show the $V = IR$ lines for the high and low bias operating points of the load curve.

It is noted that the averaged response times in Figure 4.12 are directly comparable to those obtained from the optical data. The measured time response is slightly slower than the optical test result for an equivalent bias overall. This is consistent with the bolometer being blanked off and therefore not 'optically loaded'. The inclusion of an internal illuminator was therefore not deemed to be necessary because first, these data show that the detector response time can be measured electrically, and second, the bolometer is reasonably responsive over the frequency range of interest for the PTC study (0–25 Hz). The time constant of around 24 ms gives a -3 dB point of 6.6 Hz so the signal response at 25 Hz is about 25 % of the DC level on a linear scale.

4.3.4 BASELINE PTC NOISE MEASUREMENT

The initial noise measurements carried out with the final modified readout system using DC and AC biasing are shown in Figure 4.15 and Figure 4.16 respectively. All measurements were taken at a T_S of 300 mK using a Hewlett-Packard HP35665A signal analyser. In each figure the quiescent bolometer response taken with the PTC turned off momentarily is compared to the bolometer response with the PTC running. In the

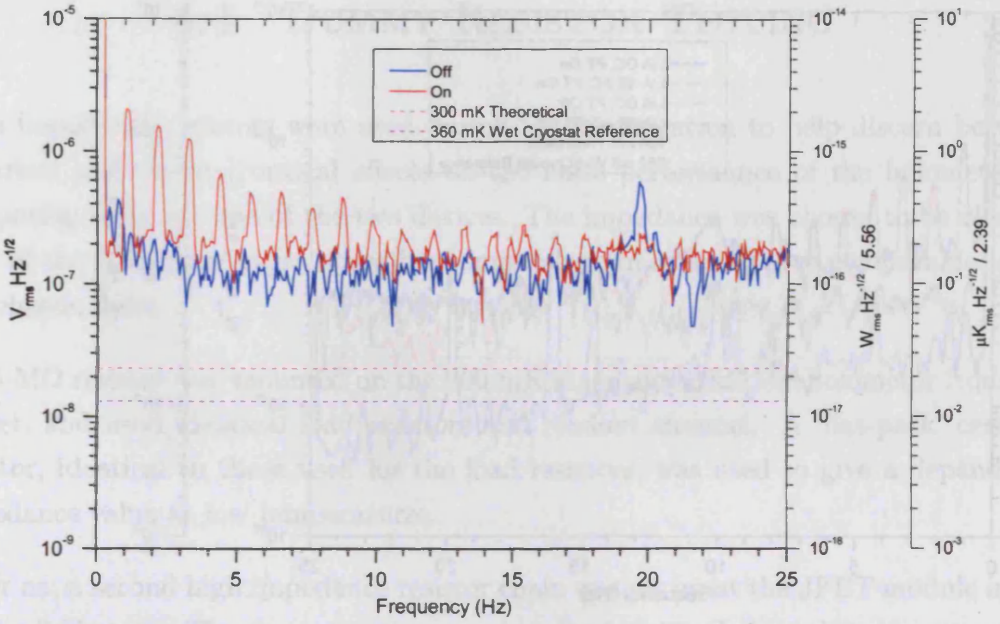

FIGURE 4.15: Initial NTD-Ge bolometer noise for DC biasing at 300 mK with the PTC turned on and off. Note the scaling factors on the axes for $W_{rms}Hz^{-0.5}$ and $\mu K_{rms}Hz^{-0.5}$.

time taken to measure the quiescent response the sorption cold head rose in temperature only by a few millikelvin, because of its good thermal isolation. Two additional y-axis scales are shown alongside the usual $V_{rms}Hz^{-0.5}$ for easier comparison to results in later chapters; the NEP shown in $W_{rms}Hz^{-0.5}$ and a temperature scale in $\mu K_{rms}Hz^{-0.5}$. The conversion factors for these scales were obtained from the responsivity and the gradient of the voltage-temperature curve respectively.

The DC bias measurements in Figure 4.15 suffer from the limited dynamic range of the signal analyser which was set to a 'DC float'[1] measurement. The DC level was too high in comparison to the bolometer noise level and so the 'white' noise is dominated by the signal analyser noise. Confirmation of this problem was obtained from measurements carried out on a dummy test resistor, see subsection 4.4.2 below. The mistake in the original setup of the signal analyser was not realised until later on and the poor quiescent DC response was incorrectly attributed to electrical pickup at the time. Nevertheless, there are features in the 'PTC on' bolometer response that are strong enough to rise above the signal analyser background. These peaks are at the PTC pulse frequency and its harmonics.

[1] 'Float' indicates that the signal is not referenced to ground. 'DC' indicates that the signal analyser does not apply any electrical filter and the zero-frequency part of the signal remains. For an 'AC float' measurement the signal analyser removes the DC level with a high-pass filter so that only the higher frequency components remain.

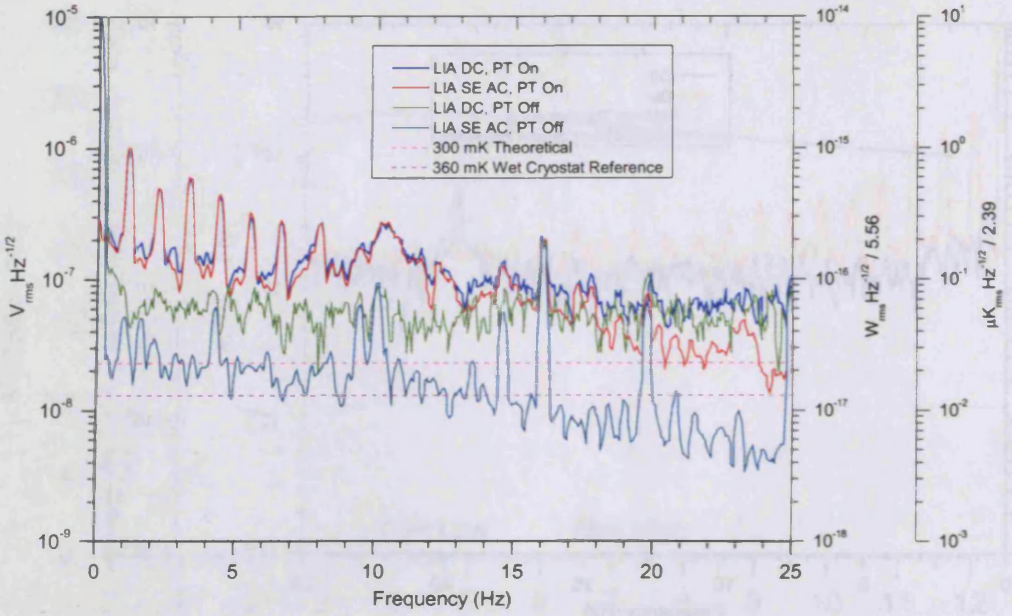

FIGURE 4.16: Initial bolometer noise for AC biasing (80 Hz) at 300 mK with the PTC turned on and off. DC refers to the DC output of the LIA while SE AC refers to a single ended AC output.

The AC bias measurements in Figure 4.16 were not as greatly affected by the limited dynamic range as the DC measurements, particulary because the LIA has an AC output that removes the DC level of the signal. Only the LIA DC output with the PTC turned off suffered from significant saturation by the signal analyser noise. Similar features to the DC responses are also present when the PTC is turned on. This is an early indication that these features are thermal in nature since an electrical signal at these frequencies would be rejected by the AC biasing system, while a thermal feature is treated like something the bolometer is viewing. However, unwanted electrical power dissipated by the NTD-Ge chip would cause an increase in overall noise level, and if it was modulated by the PTC at these lower frequencies it would produce peak features also. When the PTC was turned off the bolometer response, as measured at the LIA AC output, returned to the expected quiescent level. The roll-off seen above 10 Hz is due to the low-pass filter of the LIA (*cf.* Figure 3.14). Comparing the two AC output traces we can see that with the PTC running the voltage noise level is increased by approximately an order of magnitude for the background. Additional peak features are seen at the PTC operating frequency and its harmonics. The nature of this increase in the overall background noise level was investigated first and is reported in the following sections.

4.4 Dummy Resistor Testing

High impedance resistors were used during the investigation to help discern between electrical and thermal/optical effects on the noise performance of the bolometer by comparing noise spectra of the two devices. The impedance was chosen to be close to that of the bolometer at its operating temperature in order to give comparable levels of Johnson noise.

A 15 MΩ resistor was mounted on the 300 mK stage alongside the bolometer from the outset, and used identical load resistors and readout channel. A 'flat-pack' ceramic resistor, identical to those used for the load resistors, was used to give a dependable impedance value at low temperatures.

Later on, a second high impedance resistor chain was set up at the JFET module input on the 3 K stage. The dummy resistor and its load resistor's impedances were scaled to give similar levels of Johnson noise to the 15 MΩ, 0.3 K resistor. Consequently, a 1.5 MΩ resistor was used for the dummy detector, this time a standard 5 % tolerance metal film resistor.

4.4.1 0.3 K Resistor Chain

Initially excess noise was seen in the resistor noise response even with the PTC turned off, as shown by the DC and AC noise spectra in Figure 4.17 and Figure 4.18 respectively. With the PTC turned on the noise floor was about an order of magnitude higher than the theoretical Johnson noise (16 $nV_{rms}Hz^{-0.5}$), and when turned off there was a residual excess noise about three times higher than the theoretical. Note that the LIA DC outputs suffered from the same dynamic range problems as the bolometer measurements.

It turned out that the AC bias frequency used for the bolometer was not suitable for the resistor, and features in the resistor's DC response around the AC bias frequency were responsible for the raised noise floor when the PTC was turned off. Adjusting the bias frequency to within the 120–145 Hz range, and making use of the 'AC float' setting of the signal analyser, produces the noise spectra shown in Figure 4.19. There remained an order of magnitude increase in noise level when the PTC was turned on but the quiescent response of the resistor was about the expected Johnson noise level.

The order of magnitude increase in the background noise was present in both the

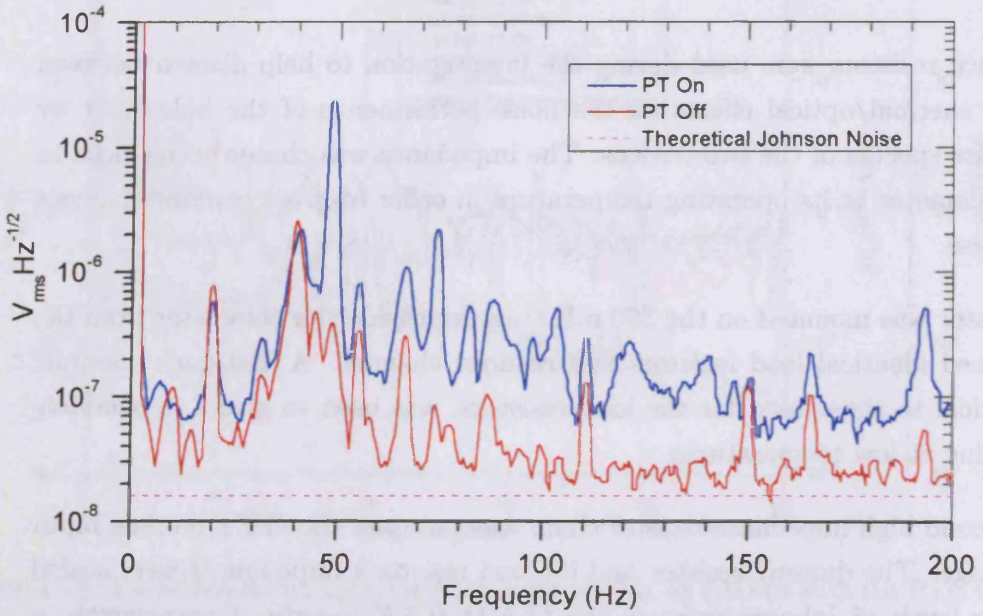

FIGURE 4.17: Initial noise spectra from the 15 MΩ fixed resistor at 300 mK, DC biased.

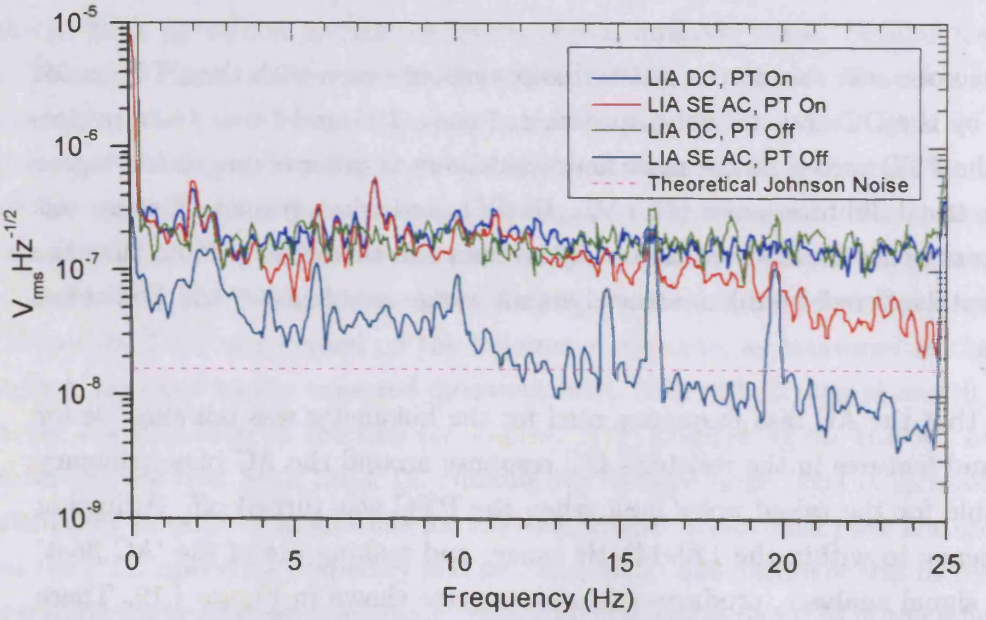

FIGURE 4.18: Initial noise spectra from the 15 MΩ fixed resistor at 300 mK, AC biased at 80 Hz.

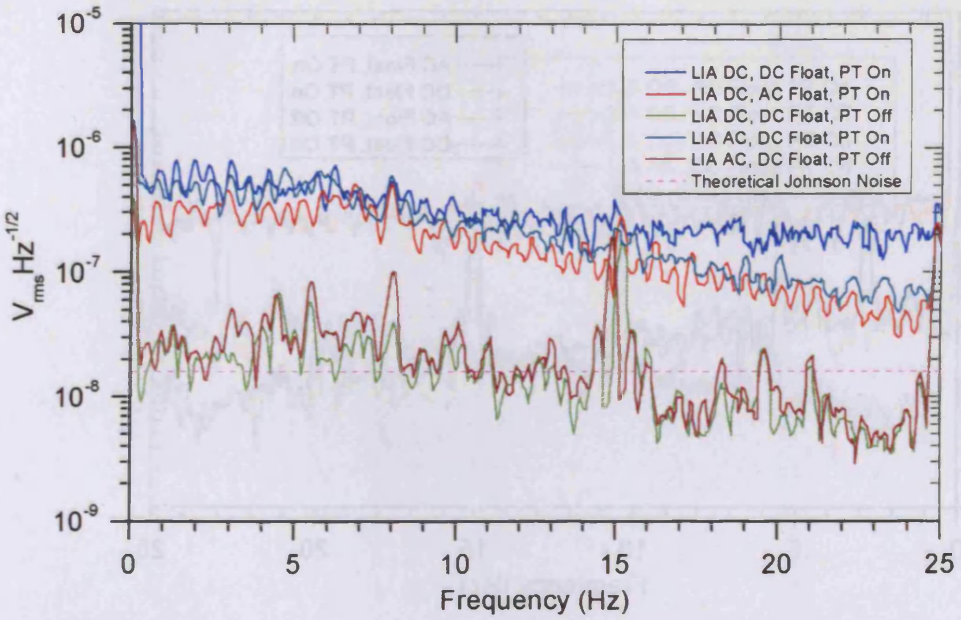

FIGURE 4.19: PTC on/off noise spectra from the 15 MΩ fixed resistor at 300 mK, AC biased at 142 Hz. 'AC Float' and 'DC Float' refers to the signal analyser setting used for that trace.

bolometer and resistor noise responses when the PTC was turned on; at this stage of the investigation it seemed that the bolometer response background was dominated by electrical pickup and had overlying peaks caused by a thermal effect. Priority was given to determining the source of the electrical pickup and taking steps to remove or significantly reduce it. The most likely source of the electrical pickup was the high impedance wiring between the bolometer and the JFET module. After the JFET amplifier down converts to a lower impedance the electrical pickup should in theory be negligible.

4.4.2 3 K Resistor Chain At JFET Input

The third channel of the bolometer readout was brought into action with the second resistor chain[2] mounted directly onto the JFET input (*ie.* at 3 K) to test the idea that noise was being introduced in the high impedance wiring between the bolometer/dummy resistor and the JFET amplifier stage. The resistor value was scaled so that the expected noise would be the same as the (30–15–30) MΩ chain, the middle resistor acting as the dummy bolometer, mounted on the sorption refrigerator cold head (~16 $nV_{rms}Hz^{-0.5}$). Hence the 3 K chain was (1.5–1.5–1.5) MΩ. The chain was made up using standard metal film resistors with a 5% tolerance value.

[2] 'Resistor chain' refers to the two 'Load' and single 'Detector' resistors in Figure 3.15

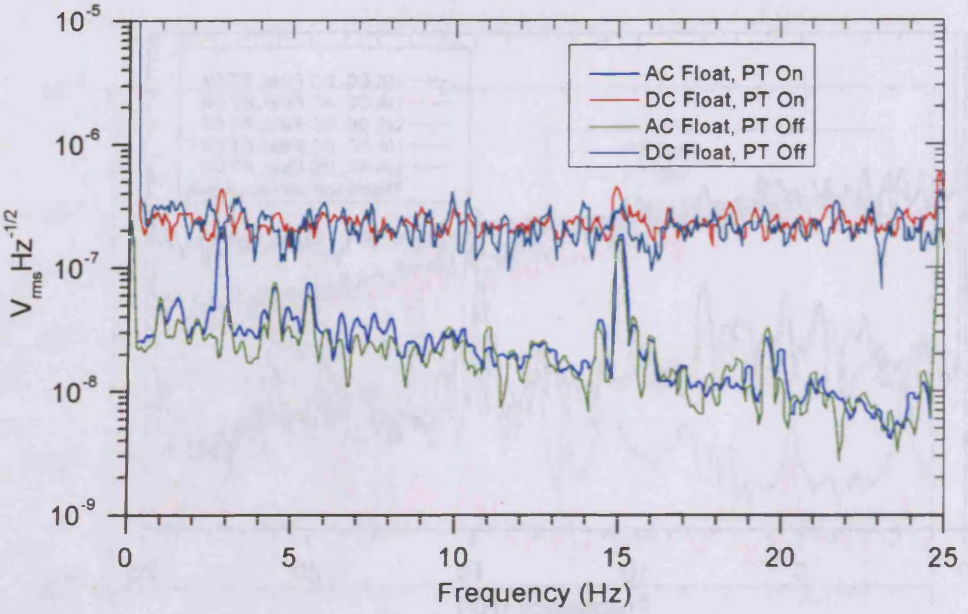

FIGURE 4.20: 3 K, 1.5 MΩ resistor noise spectra showing the limited dynamic range of the signal analyser. All traces are taken from the LIA DC output.

Tests carried out at this time also aimed to resolve the issue of excess noise seen in the LIA DC output, even with the PTC turned off. It was suggested that this was noise from the signal analyser seen when its dynamic range is too small to measure both the DC level of the signal and its noise component.

The measurements performed on the 3 K resistor chain are displayed in Figure 4.20 and Figure 4.21 and show two things. First, they confirm that the dynamic range was a problem. In Figure 4.20 the two LIA DC output traces with the signal analyser set to 'DC float' are both clearly saturated with the signal analyser noise when compared to the equivalent measurements with the 'AC float' setting. Secondly they show that without any high impedance wiring there was very little, if any, excess noise in the resistor when the PTC was turned on compared to the quiescent response when it was turned off, as shown in Figure 4.21.

These results confirmed suspicions that the high impedance wiring from the JFET module on the 3 K stage down to the detector on the 300 mK stage was by far the dominant 'source' of the electrical pickup observed. Although it would be possible to locate the JFET module closer to the sorption refrigerator cold head, by attaching it to the 3 K radiation shield for example, this would not be entirely representative of real instrument setups where heat load and physical space limitations have to be considered. It was instead decided to try modifying this length of wiring, originally a

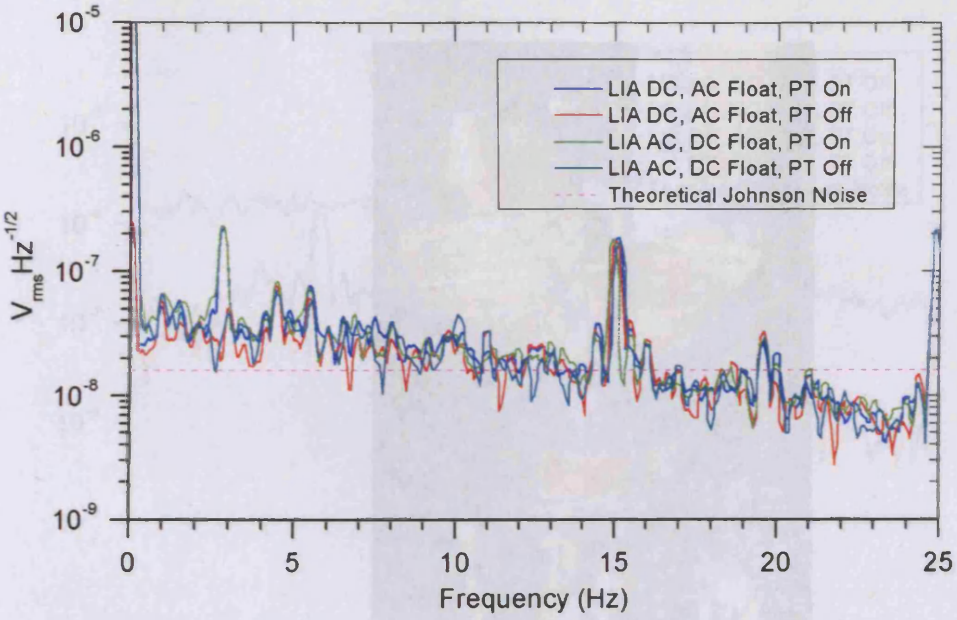

FIGURE 4.21: PTC on/off noise spectra from the 1.5 MΩ fixed resistor at 3 K, AC biased at 135 Hz.

simple twisted pair of Constantan wires, as is reported below.

4.5 High Impedance Wiring Configurations

Tests of various wiring configurations were carried out using the VeriCold PTC which had become available again after servicing. The original wiring was a simple twisted pair of Constantan secured to the sorption refrigerator using Kapton tape. The first modification replaced the bolometer and resistor signal wires, between the sorption cold head and the JFET module, with two lengths of commercially available cryogenic coaxial cable (Lakeshore CC-SS-25). The core and shield of the coaxial cable acted in place of the two Constantan wires as shown in Figure 4.22. The responses of the bolometer and resistor are shown in Figure 4.23 and Figure 4.24 respectively. The performance was worse for both devices when using this single coaxial cable configuration with neither of them now meeting the expected quiescent response level.

Two lengths of coaxial cable must be used to receive the most benefit; using only the cores for the signal lines and with the shields grounded. To begin with this was only carried out on the bolometer channel so as not to put too much extra thermal load on the sorption cold head. The resistor channel reverted to a pair of twisted Constantan wires but this time with an aluminised Mylar shield taped around it, as had already

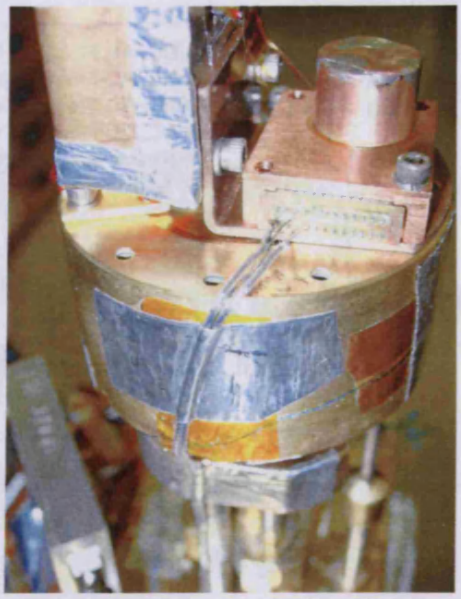

FIGURE 4.22: Single cryogenic coaxial cable setup. There is one coaxial cable for each channel (bolometer and resistor). The core is 64 strands of 50 AWG 304 stainless steel (overall diameter 0.2 mm), and the shield is 48 strands of 44 AWG 304 stainless steel (overall diameter 0.7 mm, 1 mm including insulation).

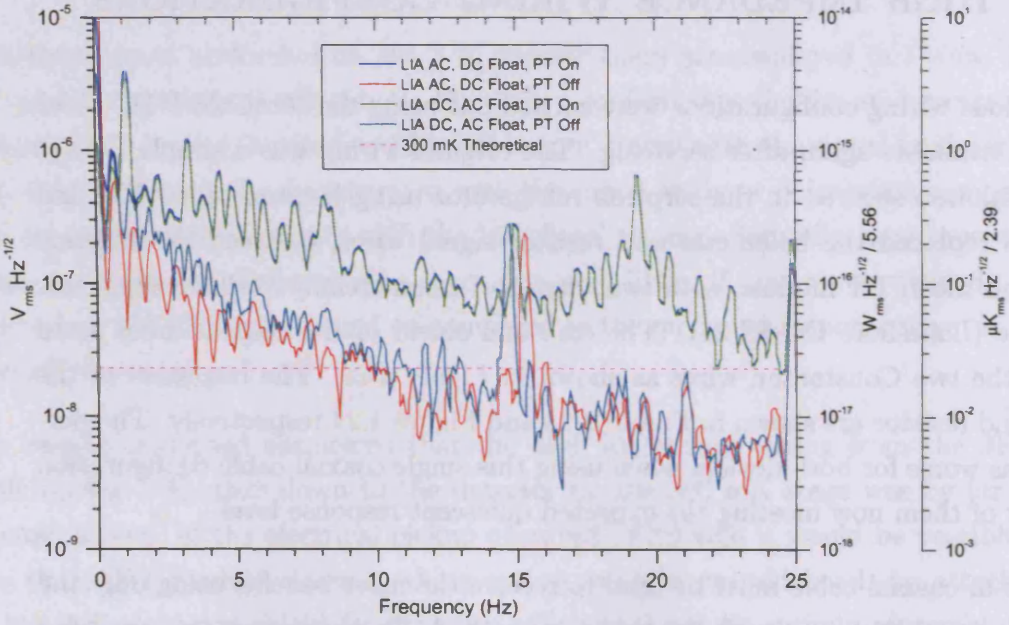

FIGURE 4.23: NTD-Ge bolometer response using a single coaxial cable between the detector and the cold JFET module.

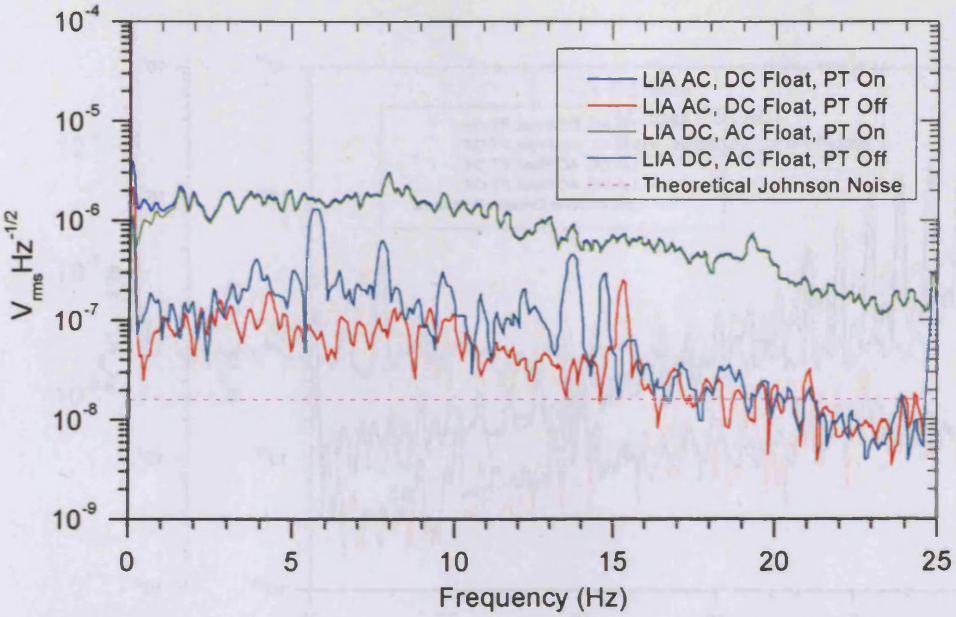

FIGURE 4.24: 0.3 K, 15 MΩ resistor response using a single coaxial cable between the resistor and the cold JFET module.

been done on the readout wires from the JFET module to the outside connector. The bolometer and resistor responses for these configurations are shown in Figure 4.25 and Figure 4.26 respectively.

The bolometer performance did improve overall by using the coaxial cable. The noise floor was reduced by about a factor of two, although the thermal peaks were stronger at the fundamental PTC frequency and harmonics up to about 6 Hz. This could be because of the increased thermal coupling between sorption and PTC cold heads through the thicker stainless steel wires, but also due to increased susceptibility to modulated electrical power at higher frequencies. The resistor meanwhile now displayed a near theoretical Johnson noise level with the PTC turned on. The first results using this configuration (Figure 4.26) did have some broad features in the spectrum which were believed to be present because the cleanest region in the DC spectrum had not been chosen for the AC bias frequency. Later results are shown in Figure 4.27 where these features have mostly managed to be avoided. Both of the traces shown in this figure were taken with the PTC running and with no other modification besides the aluminised Mylar shielding on the high impedance wires.

With the success of the Mylar tape on the resistor response, the configurations for the two channels were swapped so that the resistor channel was using the coaxial cables and the bolometer channel had the shielded twisted pair. The responses of the

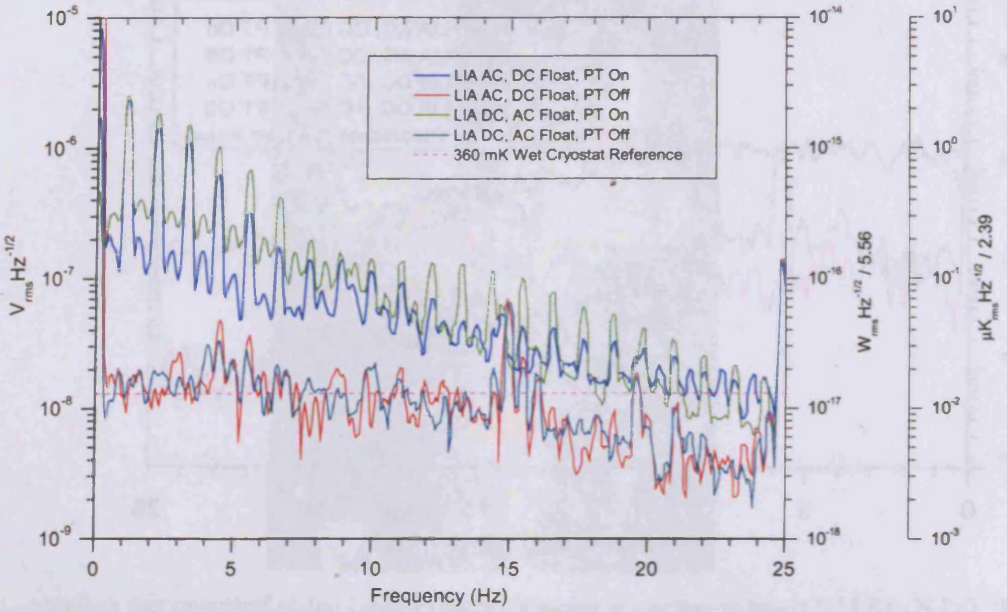

FIGURE 4.25: NTD-Ge bolometer response using twin coaxial cables between the detector and the JFET module.

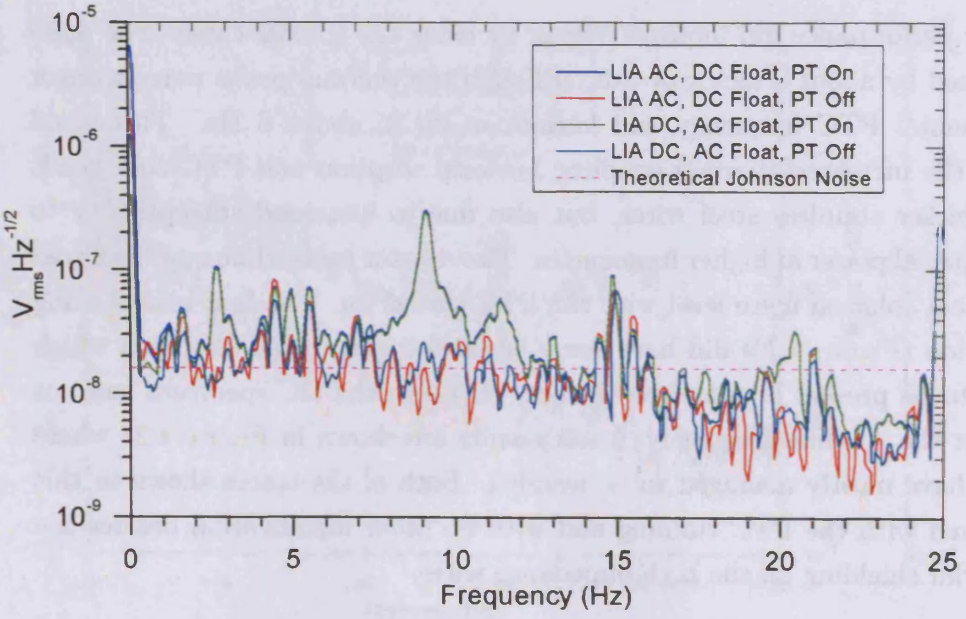

FIGURE 4.26: 0.3 K, 15 MΩ resistor response using an aluminised Mylar shielded twisted pair of Constantan wires between the resistor and the JFET module.

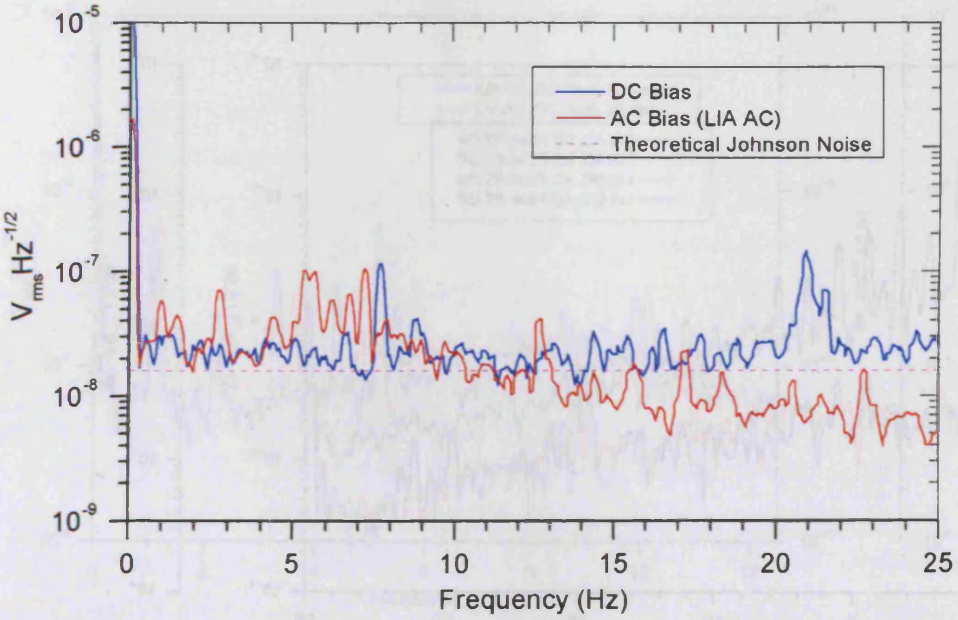

FIGURE 4.27: Improved 0.3 K, 15 MΩ, resistor response using an aluminised Mylar shielded twisted pair of Constantan wires. Both traces were taken with the PTC turned on.

bolometer and the resistor with the reversed configurations are shown in Figure 4.28 and Figure 4.29 respectively. The resistor no longer reached its quiescent noise level with the PTC turned on and while the overall noise level of the bolometer was similar to that when connected using the coaxial cable, the thermal peak features were less evident. It can also be noted that the roll off of the noise at the lower frequencies now follows that to be expected from the bolometer's time constant, *ie.* 24 ms giving a -3 dB point at approximately 6 Hz. It is likely that the additional defence against pickup offered by the twisting is what makes the shielded twisted pair slightly more effective than the coaxial cable. Perhaps if the coaxial cables were twisted together, provided there is space, then they would be equivalent.

4.6 Reducing Thermal Noise Using a Passive Thermal Filter

4.6.1 Identifying the Thermal Noise

As mentioned previously, thermal effects can be determined by comparing the bolometer response to that of the resistor which is essentially insensitive to temperature and radiation loading variations. Peaks seen in the bolometer response at the PTC pulse

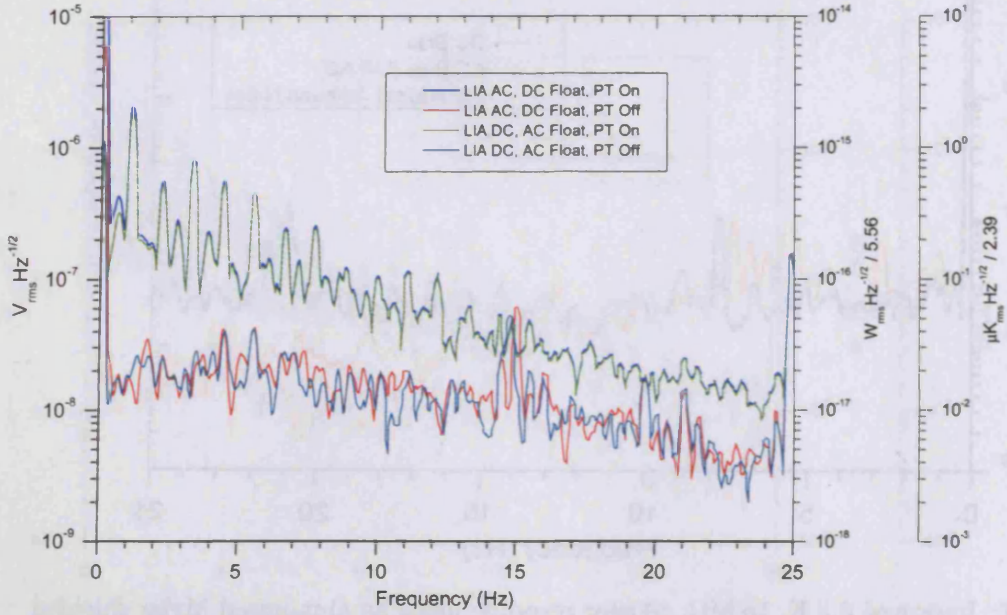

FIGURE 4.28: NTD-Ge bolometer response using an aluminised Mylar shielded twisted pair of Constantan wires between the detector and the JFET module.

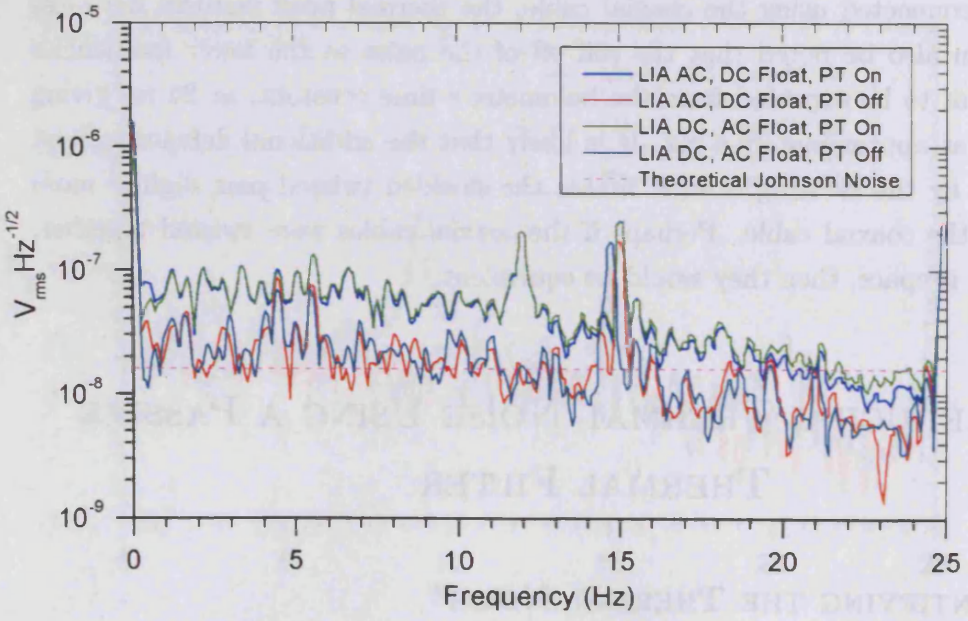

FIGURE 4.29: 0.3 K, 15 MΩ resistor response using twin coaxial cables between the resistor and the JFET module.

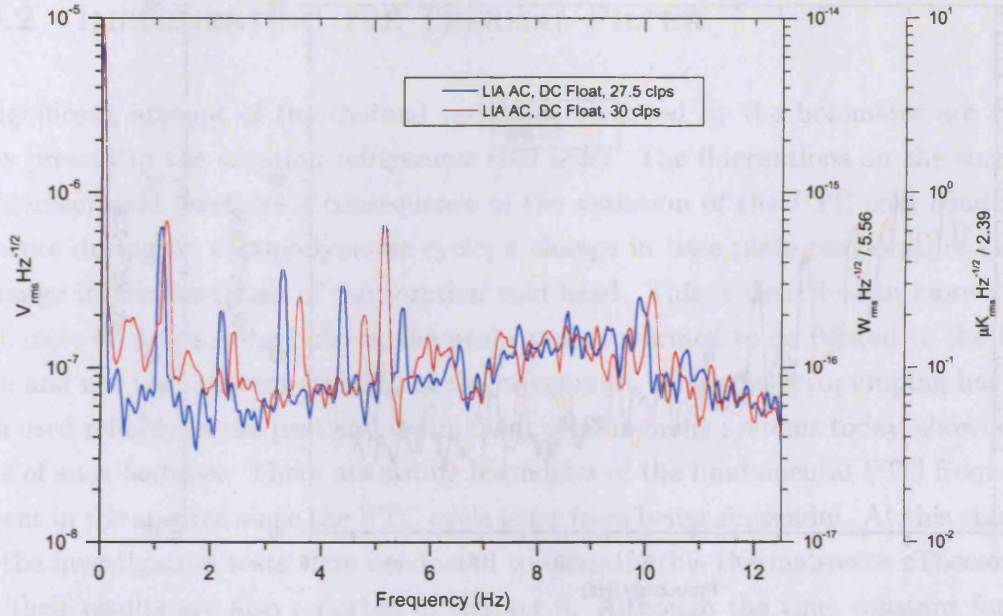

FIGURE 4.30: NTD-Ge bolometer's thermal noise peaks dependence on PTC operating frequency. Two traces are shown for PTC operating frequencies of 27.5 and 30 clps (1.1 and 1.2 Hz)

frequency (just over 1 Hz for both systems) and its harmonics are not present in the resistor response. They were confirmed to be caused by the PTC using the VeriCold system and its variable operating frequency. When the rotary valve frequency is adjusted the peaks shift accordingly.

A series of measurements were taken while adjusting the rotary valve frequency setting. The default setting is 27.5 cycle-lines per second (clps) giving a rotation frequency of $27.5/50 = 0.55$ Hz but this appears as twice this at 1.1 Hz because the valve works on half rotations. Figure 4.30 shows clearly that the fundamental and higher harmonics shifted when the frequency was changed to 30 clps (corresponding to 1.2 Hz). One peak at about 5.2 Hz did not move but this was confirmed not to be a thermal manifestation as it was also present in the noise spectrum of the 0.3 K resistor.

It is reasonable to assume that since the low frequency electrical pickup was successfully suppressed in the resistor signal, then it is also suppressed in the bolometer signal using the shielded twisted pair configuration. This suggests that the excess noise left in the bolometer response is thermal in origin; either changes in bolometer heat sink temperature, changes in dissipated electrical power, or a combination of both. To back up this statement the DC biasing response was correlated with the AC biasing LIA output. Any electrical noise present in the DC spectrum between zero and 25 Hz will not be present in the LIA output since in this case the signal is modulated at a

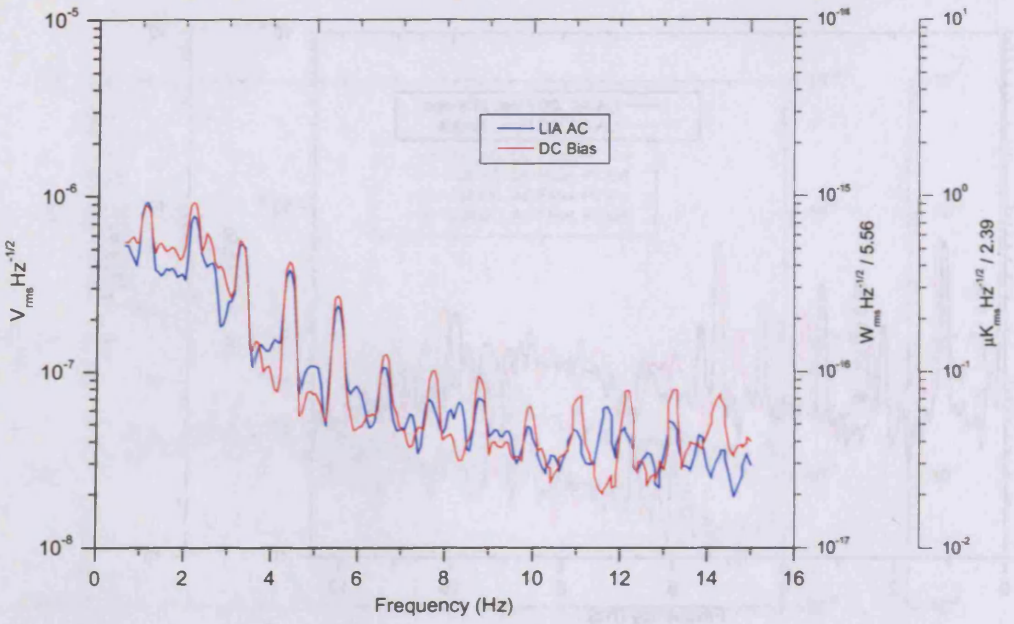

FIGURE 4.31: Comparison of the NTD-Ge bolometer's DC response and LIA output.

higher frequency. Therefore the DC response and the LIA output should look very different in the 0–25 Hz frequency range if the dominant noise in that region is random electrical pickup. On the other hand, any thermal variation is effectively treated as being a signal (as you would hope for a bolometric system!) by the AC biasing and will therefore appear in both spectra. An example is shown below in Figure 4.31 which compares the two responses in the region where no high or low pass electrical filters are operating. The strong correlation coefficient between these two traces of 0.93 indicates that a lot of the noise here is common to both the DC biasing and the AC biasing and is likely to be thermal in origin. However, it was still unclear at this point whether changes in bolometer heat sink temperature, or changes in dissipated electrical power, were now the dominant problem. Changes in electrical power dissipation caused by the operation of the PTC are believed to be very intrinsic to the PTC itself, as discussed in section 4.8. They are therefore difficult to eliminate without severe modification to the cryostat and/or PTC. It was decided to first investigate methods of reducing the bolometer heat sink temperature variations for these reasons, and because of the limited space available in the test bed.

4.6.2 Implementing the Thermal Filter

A significant amount of the thermal variations observed by the bolometer are variations present in the sorption refrigerator cold head. The fluctuations on the sorption refrigerator cold head are a consequence of the variation of the PTC cold head temperature during its thermodynamic cycle; a change in base plate temperature causes a change in the heat load of the sorption cold head. This is described in more detail in chapter 6. As described above, the peaks were confirmed to be related to the PTC cycle and not the inherent stability of the cryopumps. Charcoal cryopumping has also been used reliably in the past and is still being used in many systems today, showing no signs of such features. There are strong harmonics of the fundamental PTC frequency present in the spectra since the PTC cycle is far from being sinusoidal. At this stage of the the investigation tests were conducted to quantify this thermal noise. These tests and their results are also reported in chapter 6. Although the time constant for the sorption cold head is relatively large, the temperature fluctuations are still significant because they are so large at the PTC cold head. Attempts were made to reduce the effect of this source of thermal noise on the bolometer response at the same time.

It is a fairly common idea to increase the bolometer temperature stability by using a passive thermal filter underneath the detector, in this case a layer of Mylar, to partially isolate the detector from the temperature fluctuations. However, the thicker the buffer is, the higher the bolometer's heat sink temperature will be, and therefore the greater the degradation in detector performance. Thus, a compromise is required for any particular application. In an attempt to suppress primarily the thermal peak features, but also the overall noise level, it was decided to try this method beginning with a fairly arbitrary thickness of 50 μm (Note that no 50 μm thick Mylar was available and so two layers of 25 μm were used instead). This was successful in suppressing the higher harmonic, and to some extent the fundamental, temperature variations but did not reduce the overall noise level, as shown in Figure 4.32. The responses of the bolometer with and without the thermal buffer in place are compared. There is a visible reduction in the strength of the fundamental and first harmonic while the higher harmonics disappear into the 'white' background noise level.

A second cool down of the system was carried out without opening the cryostat. During the second series of measurements the DC response was discovered to have changed and so the AC bias frequency was adjusted to a cleaner region of the DC spectrum. It was at this point that the best bolometer performance for any setup during the investigation was observed, shown in Figure 4.33. It can be seen that the overall noise level is reduced

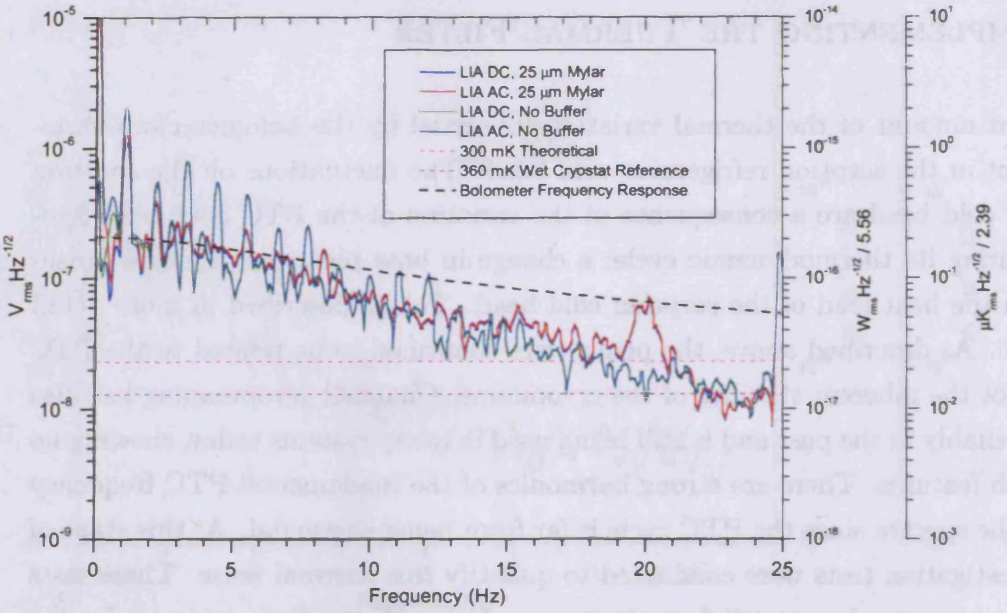

FIGURE 4.32: NTD-Ge bolometer response with and without the 2 × 25 μm Mylar thermal buffer.

and many of the harmonic peaks can no longer be seen beyond 10 Hz. The explanation for the difference between this result and that shown in Figure 4.32 is that during the warm up and cool down of the system the bolts securing the sorption refrigerator to the PTC cold head bracket had loosened. The reduced thermal contact inadvertently provided additional thermal buffering, and to a certain extent vibration isolation, and therefore improved the bolometer performance. This was unfortunately not realised at the time and so instead of pursuing the idea of buffering at the PTC-sorption interface, further tests were carried out applying thermal buffers at the bolometer mount. It was investigated later however and details can also be found in chapter 6.

Tests were continued by increasing the thickness of the thermal buffer to 100 μm (four layers of 25 μm) and tried again. The results of this test can be seen in Figure 4.34 and also shows the high correlation between the AC and DC biasing responses within the no electronic filters region (1–15 Hz). This time there was a decrease in overall noise level, as well as the peak features, everywhere except below around 3 Hz. This is an indication that the peak features are becoming dominated by modulation of high frequency noise as described below in section 4.8.

In the final stages of the thermal buffer tests the several thin layers of Mylar were exchanged for a single 185 μm layer, however the bolometer performance declined from this point on. It was suspected that the stainless steel screws holding the bolometer block to the mounting bracket, with the Mylar in between, were dominating the

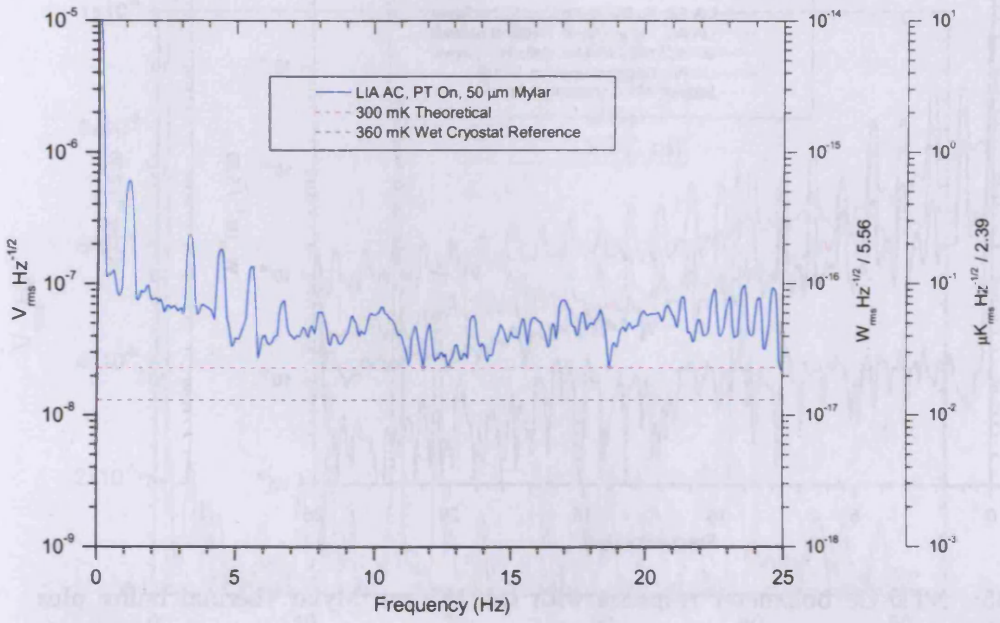

FIGURE 4.33: Best NTD-Ge bolometer response with the 2 × 25 μm Mylar thermal buffer. It is suspected that the sorption refrigerator had inadvertently become partially thermally isolated from the PTC, thereby reducing thermal noise.

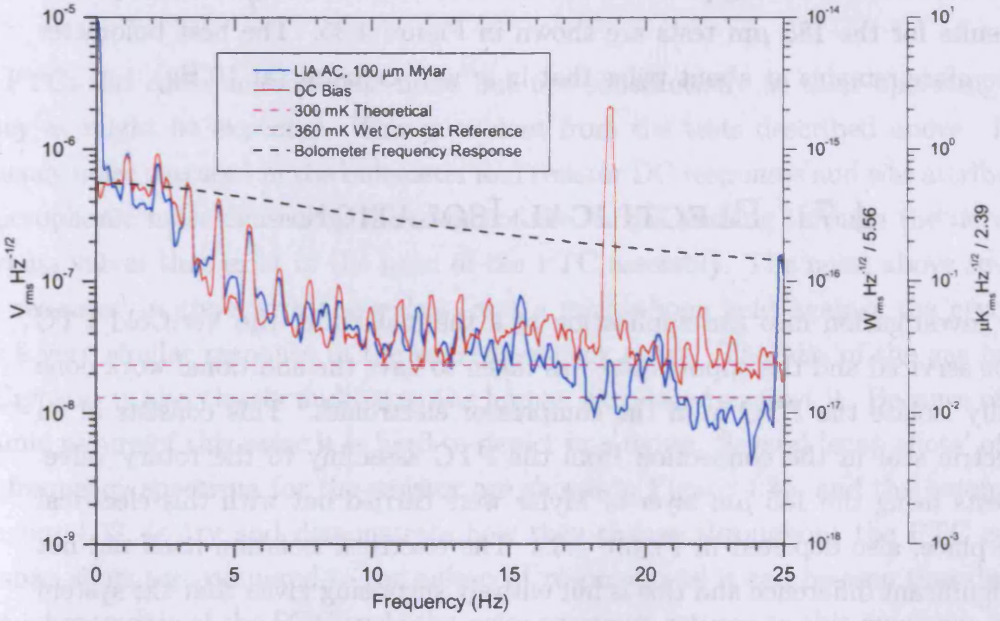

FIGURE 4.34: NTD-Ge bolometer response with the 4 × 25 μm Mylar thermal buffer. The position of the detector's frequency response (shown by the dashed black line) suggests that the roll off in the bolometer trace *is* due to the Mylar filter.

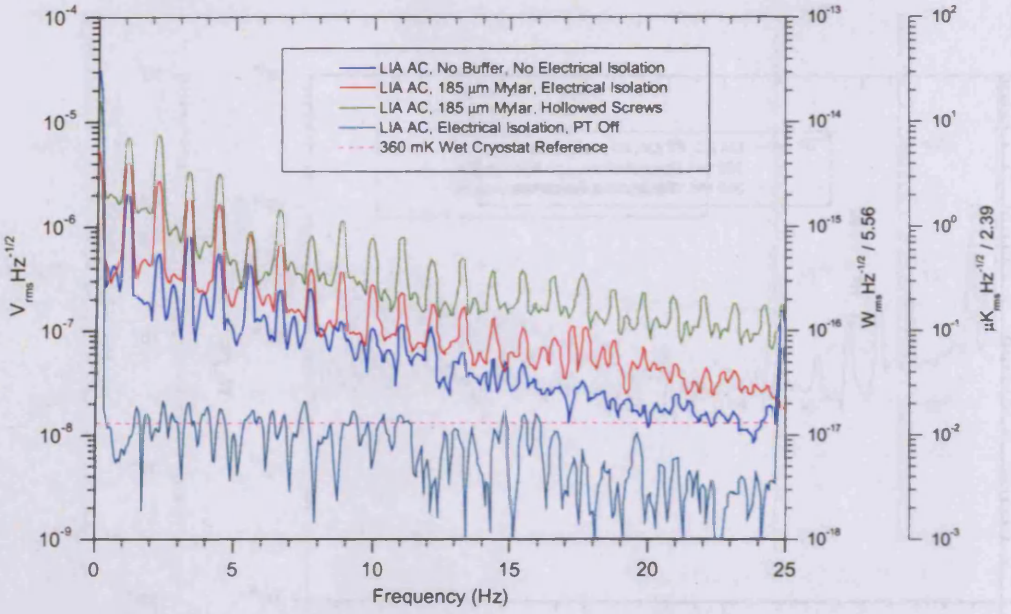

FIGURE 4.35: NTD-Ge bolometer response with the 185 μm Mylar thermal buffer plus electrical isolation.

conductance between the two and so the Mylar was reaching its maximum effective thickness. But when a test was run using hollowed out screws there was a further drop in performance. It is likely then that the bolometer was in fact becoming *too* thermally isolated and the reduced cooling power of its heat sink was hindering its noise performance. Results for the 185 μm tests are shown in Figure 4.35. The best bolometer response therefore remains at about twice that in a 'wet' cryostat (at 10 Hz).

4.7 Electrical Isolation

During the investigation into the application of a thermal buffer the VeriCold PTC needed to be serviced and the opportunity was taken to have the additional work done to electrically isolate the PTC from the compressor electronics. This consists of an epoxy dielectric seal in the connection from the PTC assembly to the rotary valve. The final tests using the 185 μm layer of Mylar were carried out with this electrical isolation in place, also depicted in Figure 4.35. The electrical isolation itself did not make any significant difference and this is not entirely surprising given that the system was already well grounded.

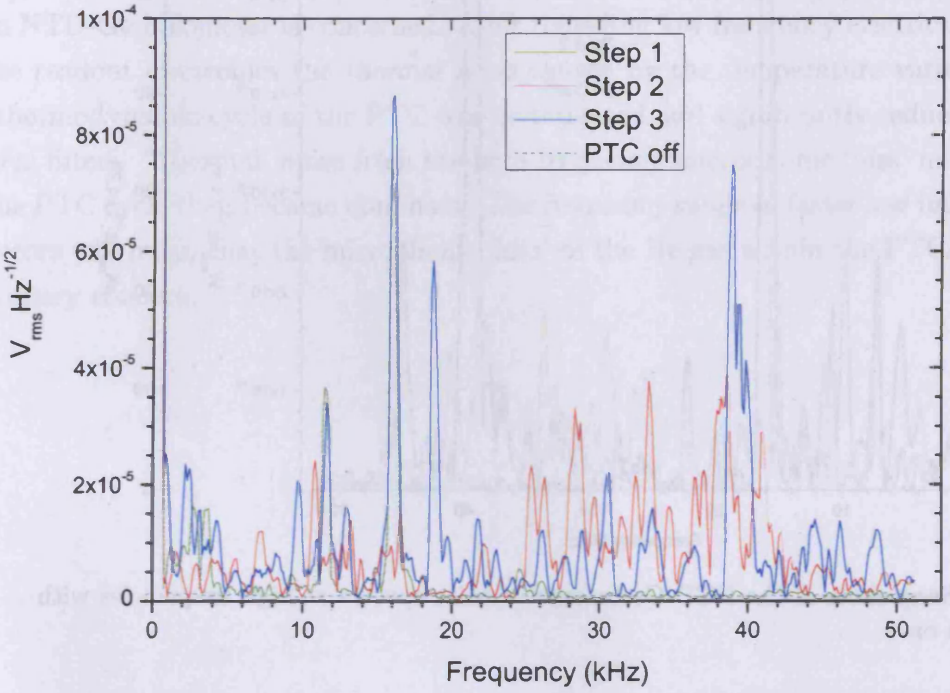

FIGURE 4.36: Snap shots of the 0.3 K, 15 MΩ resistor noise spectra at high frequencies with the PTC turned on.

4.8 HIGH FREQUENCY MICROPHONICS

The PTCs did cause microphonic noise but not substantially at their operating frequency as might be expected. This is evident from the tests described above. High frequency noise was seen in the bolometer and resistor DC responses and was attributed to microphonic noise caused by the sound of the He gas passing through the network of bypass valves that exist in the head of the PTC assembly. The noise above several kHz 'see-saws' in time with the pulses, and a microphone held against the cryostat gives a very similar response in the same frequency range. The hiss of the gas inside the Cryostat is also clearly audible to the human ear placed against it. Because of the dynamic nature of this noise it is hard to depict in a figure. Several 'snap shots' of the high frequency spectrum for the resistor are shown in Figure 4.36, and the bolometer in Figure 4.37, to try and demonstrate how they change throughout the PTC cycle. The snap shots are compared to the quiescent response and it can be seen that during the quiet moments of the PTC cycle the noise spectrum returns to this quiescent level. This behaviour was seen when using both the Cryomech and the VeriCold PTCs and so initial concerns that the Cryomech's digital stepper motor control electronics may be interfering with the bolometer readout were put to rest.

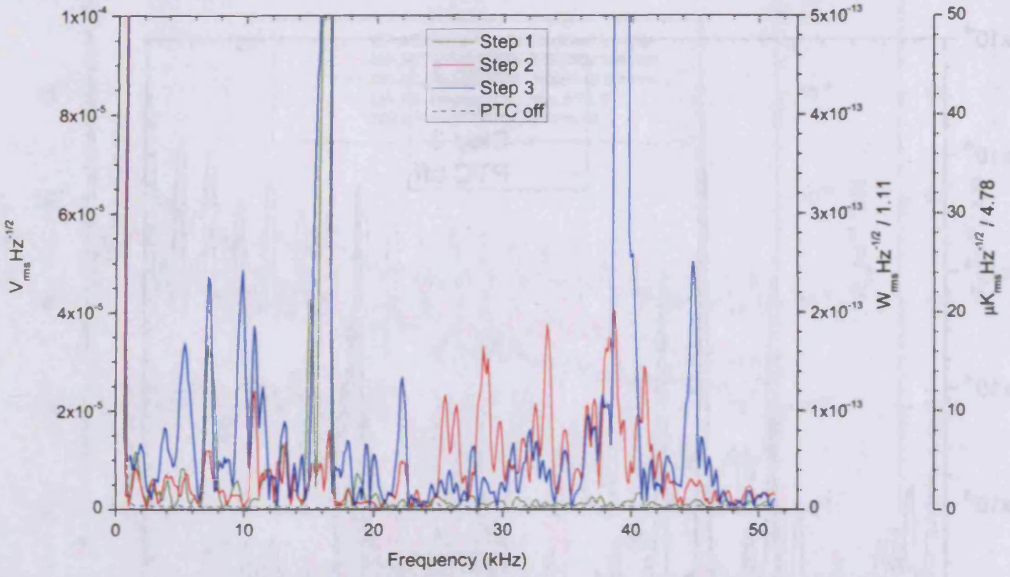

FIGURE 4.37: Snap shots of the NTD-Ge bolometer noise spectra at high frequencies with the PTC turned on.

It is believed that the microphonic vibrations caused by the gas are transmitted to the bolometer readout wiring by the structure of the PTC that the wires are strapped to. This high frequency microphonic noise results in an excess dissipation of electrical power in the bolometer, raising its temperature slightly. The modulation by the PTC cycle varies this temperature rise and produces peak features that combine with those caused by the heat sink temperature variations. So the high frequency noise manifests itself as a thermal feature in the bolometer's response, and hence is not present in the resistor's response, although at its source it is electrical in nature. The high frequency noise itself is more of a potential problem than the thermal variations for faster detectors such as 4 K InSb hot electron bolometers. Even with their lower impedance of a few kΩ, the same 'see-sawing' noise was seen in the response of an InSb detector mounted on the PTC cold head. Details of this can be found in the following chapter.

4.9 300 mK NTD-Ge Bolometer Conclusions

The investigation into the operation of a 300 mK NTD-Ge bolometer with a PTC has shown that near theoretical performance can be achieved with only minor modifications to the conventional setup of the detector and cryogenics. A noise level two times the quiescent response at 10 Hz was obtained.

A methodical series of tests has prioritised the various sources of excess noise as far as an NTD-Ge bolometer is concerned. After removing low frequency electrical pickup in the readout electronics the thermal noise caused by the temperature variations of the thermodynamic cycle of the PTC was investigated and significantly reduced using passive filters. 'Thermal' noise from the high frequency microphonic 'hiss' modulated by the PTC cycle then became dominant. The frequency range of faster low impedance detectors will mean that the microphonic 'hiss' of the He gas within the PTCs will be of primary concern.

Chapter 5

3–4 K InSb Hot Electron Bolometer Tests

This chapter describes the tests carried out to investigate the performance of an InSb hot electron bolometer operated on the cold head of each of the PTC systems in turn. InSb hot electron bolometers (HEBs) are used in applications where fast detectors are more desirable than having the most sensitive detectors (Examples of such applications are given in subsection 1.6.5). Their time constants of fractions of a microsecond give them a bandwidth up to and above one MHz.

The HEB was provided by QMC Instruments and is one of their standard designs that are commercially available. It consists of a 7-legged InSb element that is toaster like in shape, mounted on a 5 mm×5 mm quartz substrate, as pictured in Figure 5.1. All testing was done in the dark, *ie.* with the detector blanked off. The detector block was initially mounted directly onto the PTC cold head with a twisted pair of Constantan wires connecting it to the outside connector. The readout used was the ULN95 preamplifier unit from QMC Instruments that is sold with the InSb detectors.

5.1 Wet Cryostat Baseline Testing

The detector was first characterised in a liquid helium bath cryostat so that this quiescent performance could be compared to the performance in a PTC cooled cryostat. A uniform noise level of 1.7 $nV_{rms}Hz^{-0.5}$ was obtained at reference frequencies of 1,

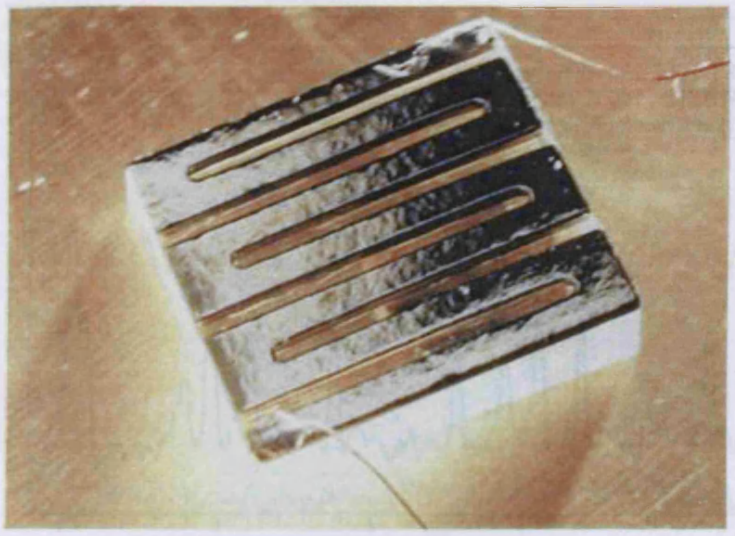

FIGURE 5.1: The InSb hot electron bolometer 'toaster' element mounted on a quartz substrate.

10 and 25 kHz, including the 1 $nV_{rms}Hz^{-0.5}$ amplifier noise. A DC bias of 21.2 μA was used and the detector's operating impedance at 4.2 K was 3.94 kΩ. An optical responsivity of 0.68 kVW^{-1} was measured giving an NEP of 2.5 $pW_{rms}Hz^{-0.5}$.

5.2 CRYOMECH PTC TESTING

The detector was then tested using the Cryomech PTC system while the VeriCold was in use with the NTD-Ge bolometer testing. During these first PTC tests the PTC cold head was warmed up to about 4 K to replicate the conditions of the 'wet' cryostat. The HEB responses with the PTC turned on and off are compared to the 'wet' cryostat noise level in Figure 5.2. There is over an order of magnitude difference in the noise level with the PTC turned on compared to when it is turned off. The 'off' response also shows some excess noise in relation to the quiescent 'wet' response.

This excess could be due to the unshielded wiring used for the two signal lines, and also the water chiller that was being used to cool the compressor unit at this time. Unfortunately circumstances did not permit further investigation into the HEB performance with the Cryomech PTC system to give credence to this theory. The Cryomech was required for other purposes and the device had to be transferred to the VeriCold system alongside the NTD-Ge bolometer testing.

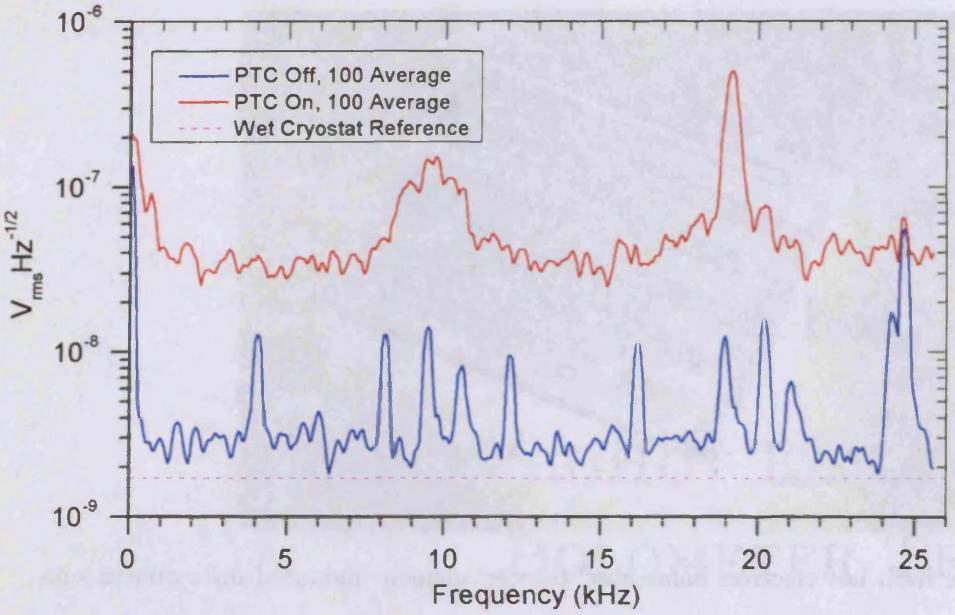

FIGURE 5.2: Hot electron bolometer response while mounted in the Cryomech PTC. Traces are shown for the PTC turned on and off and are compared to the noise level obtained in the 'wet' cryostat.

5.3 VERICOLD PTC TESTING

The tests performed with the VeriCold system were carried out at the lower PTC cold head temperature of around 3 K. This was necessary because of the 300 mK tests being done in parallel. The detector therefore had a higher operating impedance of approximately 5 kΩ and larger bias current of 44 μA. The other difference was that this time the wiring was shielded with aluminium tape.

The HEB response with the PTC turned on is shown for a variety of frequency ranges in Figure 5.3, Figure 5.4, and Figure 5.5, which also show the equivalent 'wet' cryostat response for comparison[1]. Given the slightly higher impedance the HEB performs nominally in the PTC system up to 6 kHz but with some additional *1/f* noise, presumably from the thermal noise of the PTC cold head fluctuations (These were visible below 25 Hz as they were with the 300 mK tests). Up to 12 kHz there was a more notable drop-off in performance and above this frequency there were problems with the acoustic 'see-sawing' noise of the He gas inside the PTC as expected.

A single noise spectrum has been compared to an average of 100 spectra to show the problem of the acoustic noise and to demonstrate its dynamic nature more clearly. This

[1] The exception is Figure 5.3 which uses the 'wet' cryostat response up to 12 kHz in the absence of data at 6 kHz.

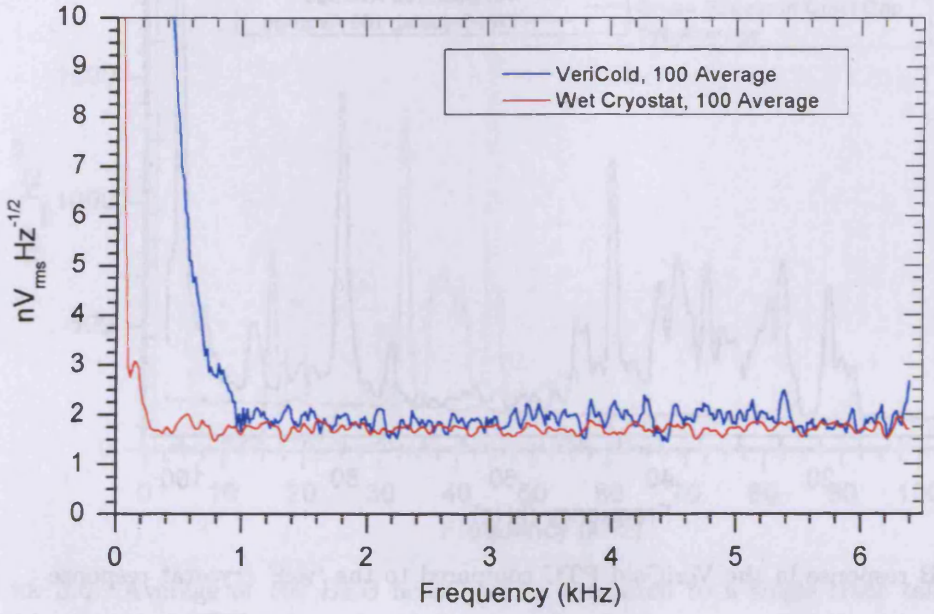

FIGURE 5.3: HEB response in the VeriCold PTC compared to the 'wet' cryostat response up to 6 kHz.

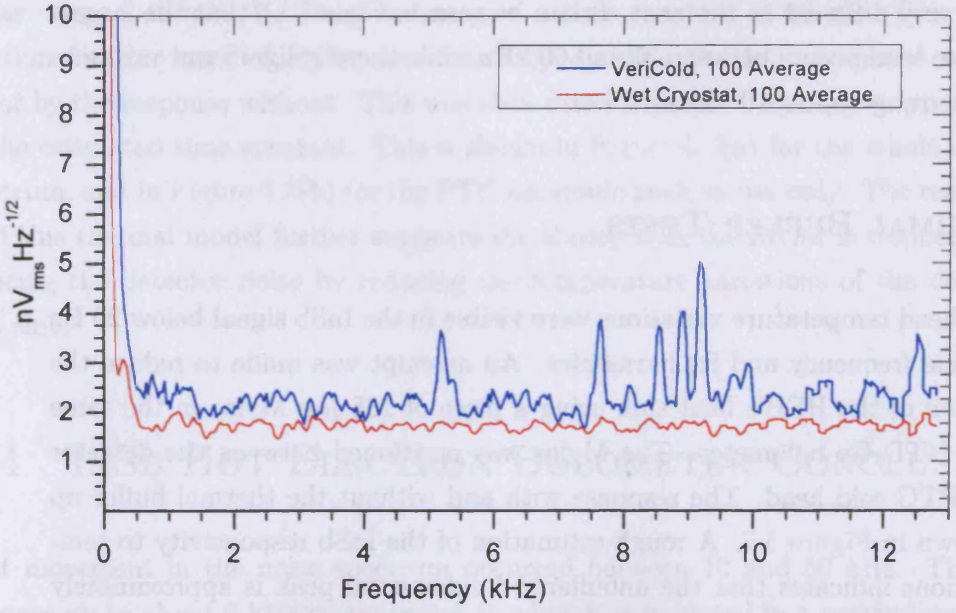

FIGURE 5.4: HEB response in the VeriCold PTC compared to the 'wet' cryostat response up to 12 kHz.

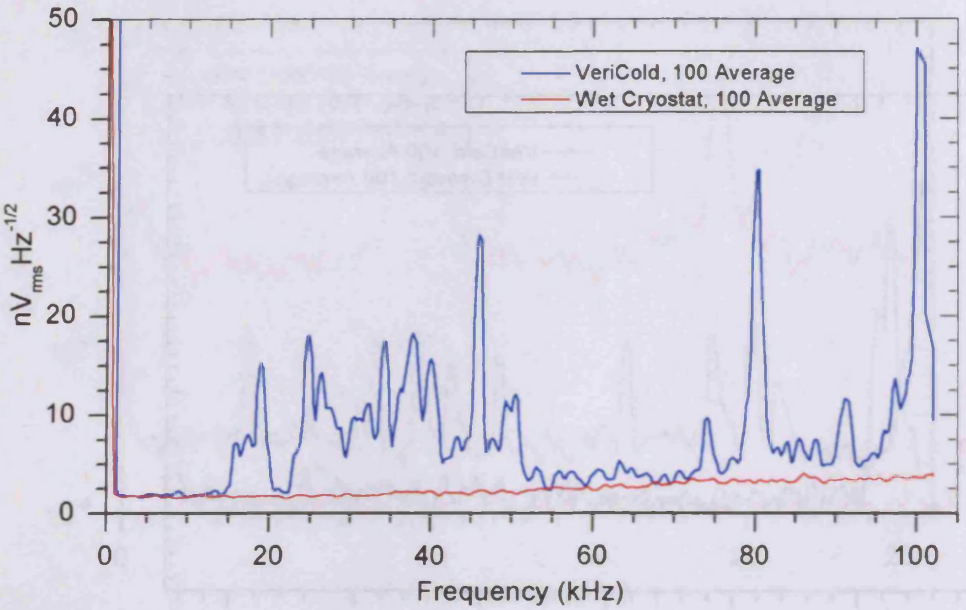

FIGURE 5.5: HEB response in the VeriCold PTC compared to the 'wet' cryostat response up to 100 kHz.

comparison is shown in Figure 5.6. The single spectrum was timed to coincide with the relatively quiet gap between the PTC's pulses. Note that the scale is fairly arbitrary since the gain of the system has not been taken into account like it has been with the other figures. It can be seen however that at these high frequencies the situation at one moment is very different to the next. It can be seen in Figure 5.6 that the largest variation in noise level occurs between 20 and 60 kHz while there is significant variation across the entire range up to 100 kHz.

5.3.1 THERMAL BUFFER TESTS

The PTC cold head temperature variations were visible in the InSb signal below 25 Hz at the PTC cycle frequency and its harmonics. An attempt was made to reduce the thermal variation of the HEB's heat sink using a piece of 185 μm Mylar in the same way as for the NTD-Ge bolometer. The Mylar was positioned between the detector block and the PTC cold head. The response with and without the thermal buffer up to 25 Hz is shown in Figure 5.7. A rough estimation of the InSb responsivity to temperature variations indicates that the unbuffered fundamental peak is approximately 60 $mK_{rms}Hz^{-0.5}$. The fundamental peak was reduced by almost an order of magnitude while higher harmonics were reduced much more. This again suggests that thermal buffering in the case of a 300 mK detector may be best implemented at the PTC cold

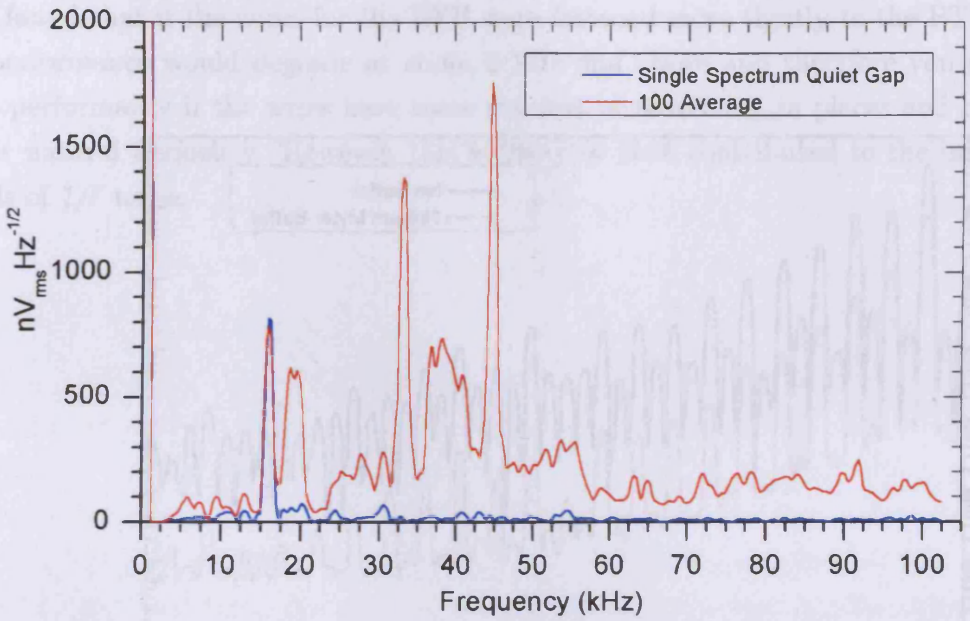

FIGURE 5.6: Average of 100 HEB noise spectra compared to a single trace taken in the 'quiet' gap between PTC pulses.

head stage.

The time constant for the InSb detector block's temperature variations was estimated by calculating it's heat capacity, ~4.8 mJ/K, and the thermal conductance of the Mylar layer, ~49 mW/K. These values give a time constant of 98 ms. The transfer function for the layer of Mylar was found by dividing the InSb response with the Mylar by the response without. This was then fitted with the frequency response given by the estimated time constant. This is shown in Figure 5.8(a) for the whole 0–25 Hz spectrum, and in Figure 5.8(b) for the PTC harmonic peak values only. The reasonable fit of this thermal model further supports the theory that the Mylar is responsible for reducing the detector noise by reducing the temperature variations of the detector's heat sink.

5.4 InSb Hot Electron Bolometer Conclusions

Most movement in the noise spectrum occurred between 10 and 50 kHz. The HEB response up to about 6 kHz is equivalent to when it is mounted in a conventional 'wet' cryostat and it is hypothesised that the acoustic noise seen will drop off before the MHz range where the detectors are commonly used. No data acquisition system capable of measuring the response at this frequency was available at the time however. It was

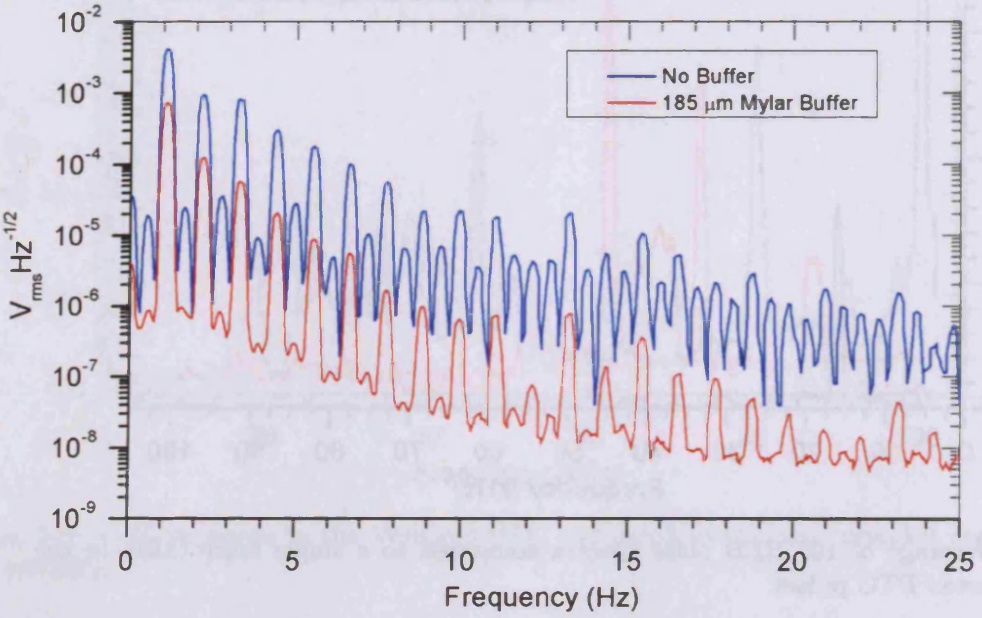

FIGURE 5.7: HEB response in the VeriCold PTC with and without the 185 μm Mylar thermal buffer.

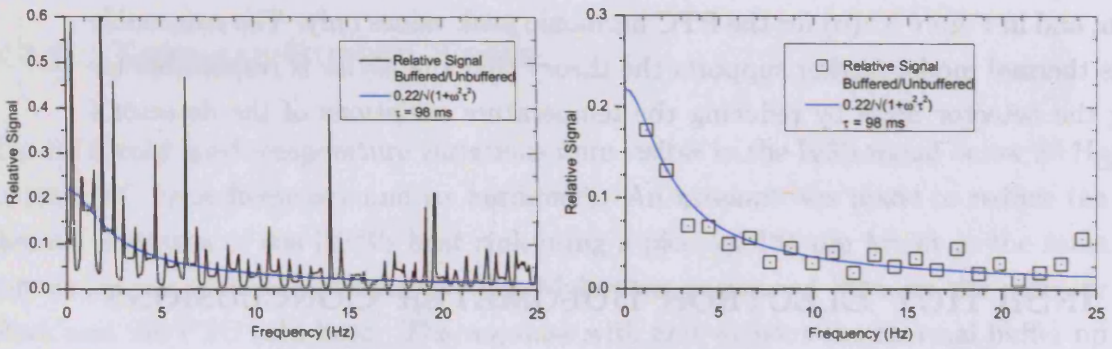

(a) Whole spectra.

(b) Harmonic peak values only.

FIGURE 5.8: Relative InSb signal — buffered/unbuffered.

also found that if the wires for the HEB were fastened more tightly to the PTC then its performance would degrade at about 3 kHz and above and therefore you get the best performance if the wires have some freedom of movement in places and hence a lower natural frequency. However, this is likely to have contributed to the increased levels of $1/f$ noise.

Chapter 6

Thermal Fluctuation Measurements

This chapter presents the results of the investigation into the thermal noise resulting from the temperature fluctuations of the PTC cold head caused by its thermodynamic cycle. This thermal noise was observed at low frequencies (0–25 Hz), as described in the previous two chapters, at the PTC's fundamental cycle frequency and its harmonics.

Once the temperature stability of the sorption cold head had been identified as being a problem for the NTD-Ge bolometer it was decided to try and measure the thermal fluctuations on the 300 mK stage using a 'bare' NTD-Ge chip similar to that used for the bolometer itself. Unlike the bolometer NTD chip, which has a weak heat link through the Si_3N_4 mesh and niobium wires, this bare chip was placed in good thermal contact with the sorption refrigerator cold head using a copper mounting block. This NTD-Ge thermistor was read out on an identical channel to the bolometer. The NTD-Ge thermistor spectra were converted to units of temperature using its characterisation parameters and the usual exponential fit for the resistance-temperature curve, $R(T) = R_* exp(T_g/T)^{1/2}$ (From Equation 1.17 using $n = 1/2$).

Since the temperature fluctuations on the 300 mK stage are caused by the base plate fluctuations it was desirable to measure them also. This was simply done by linking the temperature sensor (diode) signal voltage to the signal analyser. The voltage noise could then be converted to units of temperature using the diode calibration.

Before discussing the results of these measurements I will first describe in more detail the theory of how these temperature fluctuations are seen at the sorption cold head.

This model is then used later on to compare the temperature fluctuations on the PTC cold head with those on the sorption cold head.

6.1 PTC-Sorption Refrigerator Coupling Model

For the purposes of this model, the sorption refrigerator cold head can be thought of as a bolometer with the PTC being equivalent to its heat sink (*cf.* Figure 1.8). They are physically connected by a weak thermal link (the pumping tubes) with some value of conductance but, just like a bolometer, it also has an *effective* conductance. The sorption refrigerator's load curve, like the bolometer's load curve, tells us this effective conductance. Continuing the analogy, the physical time constant for the sorption cold head can be obtained by combining the effective conductance (gradient of the cooling power load curve) with the heat capacity.

The heat capacity of the sorption cold head is dominated by the contained liquid ^{3}He. The full charge of 8 litres STP has a heat capacity of around 1 mJ/K. The gradient of the cooling power load curve, Figure 3.4, at 300 mK is approximately 442 μW/K. Hence the time constant for the sorption cold head is about 2.3 s, giving a -3 dB point in its frequency response of only 69 mHz. At first glance it seems that it is unlikely that the sorption refrigerator would feel the effects of any temperature variations at the PTC cold head, but they can still be significant if the PTC fluctuations are large enough.

The amplitude for the sorption cold head's responsivity to temperature changes was estimated by finding the gradient of a plot of conductive heat load against base plate (PTC) temperature. It is the conductive power through the pumping tubes that dominates the total heat load of the sorption cold head. The dependance of the heat load on PTC temperature was found to be approximately quadratic; $W = 1.47 \times 10^{-6}T^2$. The ratio of the temperature changes on the two cold heads is then found by dividing the gradient of the heat load at the PTC temperature, $\sim$8.87 μW/K, by the gradient of the cooling power at the sorption cold head temperature, $\sim$442 μW/K. It is therefore estimated that the sorption cold head temperature change is about 2 % that of the PTC temperature change.

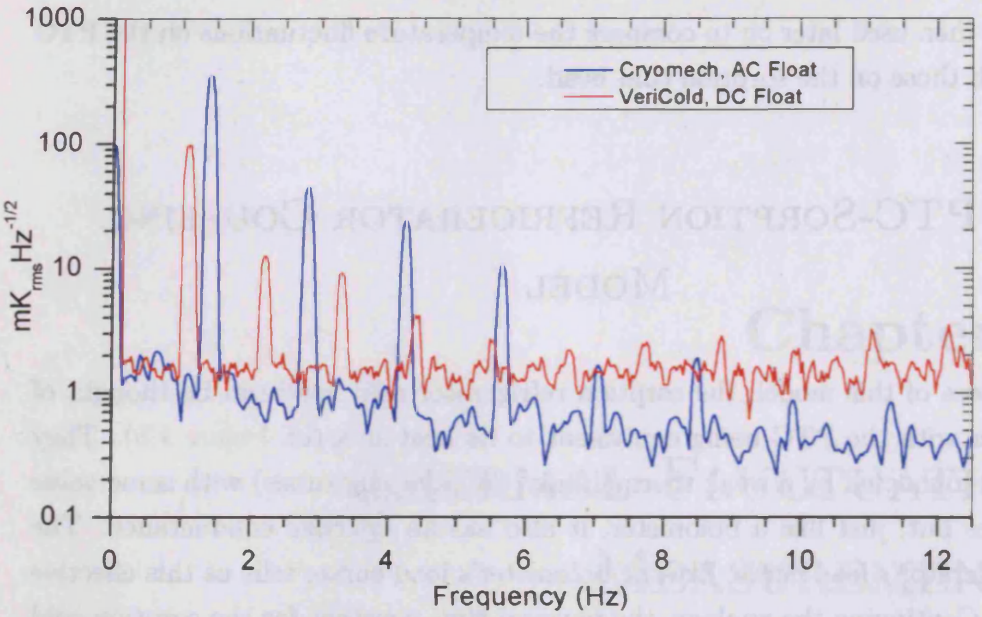

FIGURE 6.1: PTC second stage temperature fluctuations. Both systems used the same diode thermistor.

6.2 PTC WITH 2-STAGE SORPTION REFRIGERATOR

It was observed that the noise level for both detectors was substantially higher when using the Cryomech system compared to the VeriCold system. The thermal fluctuation measurements were therefore carried out in both systems to see if these were also larger for the Cryomech. It was expected to be the case since the thermal noise from heat sink temperature instabilities appeared to be contributing significantly to the NTD-Ge bolometer's response.

6.2.1 PTC COLD-HEAD MEASUREMENTS

The diode thermistor signal was linked to the input of the signal analyser and the average of 10 power spectra was taken over the frequency range 0–12.5 Hz. The results for both PTCs can be seen in Figure 6.1. Note that the trace for the VeriCold system is partially saturated by noise from the signal analyser because of its limited dynamic range and the 'DC float' setting which does not remove the DC voltage level. Besides this the results show clear features at the PTC operating frequency and its harmonics, slightly different for each system. The fact that odd *and* even harmonics are present suggests a cold head temperature variation along the lines of a triangle wave for both PTCs.

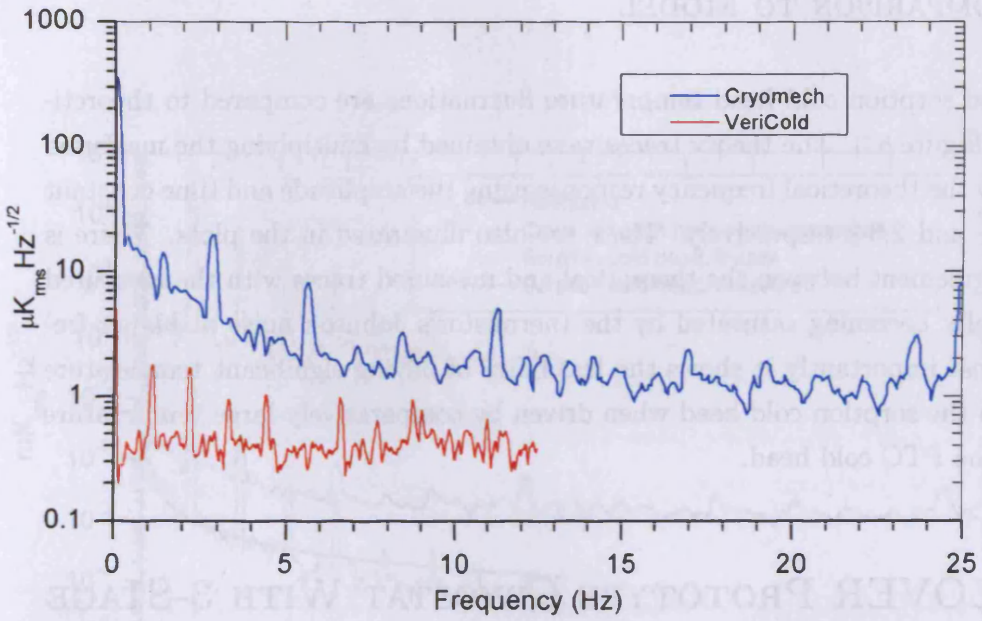

FIGURE 6.2: 2-stage sorption refrigerator cold head temperature fluctuations.

Converting the fundamental to a peak-to-peak temperature variation gives 170 mK_{pp} for the Cryomech and 50 mK_{pp} for the VeriCold (These agree well with the spread of the logged temperature-time data). It may therefore be expected that temperature fluctuations on the 300 mK stage will be around twelve times larger for the Cryomech given the quadratic dependance of heat load on PTC temperature.

6.2.2 SORPTION COLD-HEAD MEASUREMENTS

The NTD thermistor was read out using a DC bias so that the results were unaffected by electrical filters in the AC bias readout. Once again averages of 10 spectra were taken. The results for both systems are shown in Figure 6.2.

The corresponding peak-to-peak variations for the fundamental are about 9.5 μK_{pp} for the Cryomech and 0.9 μK_{pp} for the Vericold. This is in fairly good agreement with the quadratic dependance previously stated when compared with the PTC temperature variation amplitudes.

6.2.3 Comparison to Model

The measured sorption cold head temperature fluctuations are compared to theoretical traces in Figure 6.3. The theory traces were obtained by multiplying the measured PTC trace by the theoretical frequency response using the amplitude and time constant of about 2 % and 2.3 s respectively. These are also illustrated in the plots. There is reasonable agreement between the theoretical and measured traces with the measured traces naturally becoming saturated by the thermistor's Johnson noise at higher frequencies. Most importantly it shows the feasibility of having significant temperature variations on the sorption cold head when driven by comparatively large temperature changes on the PTC cold head.

6.3 CLOVER Prototype Cryostat With 3-Stage Sorption Refrigerator

The final set of temperature fluctuation measurements were carried out in the prototype *Clover* cryostat. This utilised a large 15 kg base plate connected to the PTC cold head using flexible copper straps and also a three-stage sorption refrigerator. The large mass of the base plate necessitates the use of a mechanical support system so as not to put too much stress on the PTC. Therefore the flexible thermal straps are required to interface the base plate with the PTC cold head. The setup of this cryostat is shown in Figure 6.4.

The large mass of the base plate together with the copper straps provide some thermal and vibrational buffering between the sorption refrigerator and the PTC. In addition, the intermediate sorption refrigerator cold head will also protect the ultra cold head from base plate temperature variations via conduction through the stainless steel tubes because of the specific heat capacity of the contained liquid ^{3}He.

Unfortunately no NTD-Ge bolometer was available at the time to see how it would perform under these conditions. Given the fact that the bolometer's peak features are of roughly equivalent magnitude to the measured sorption cold head temperature fluctuations, it was possible to get a very good insight however.

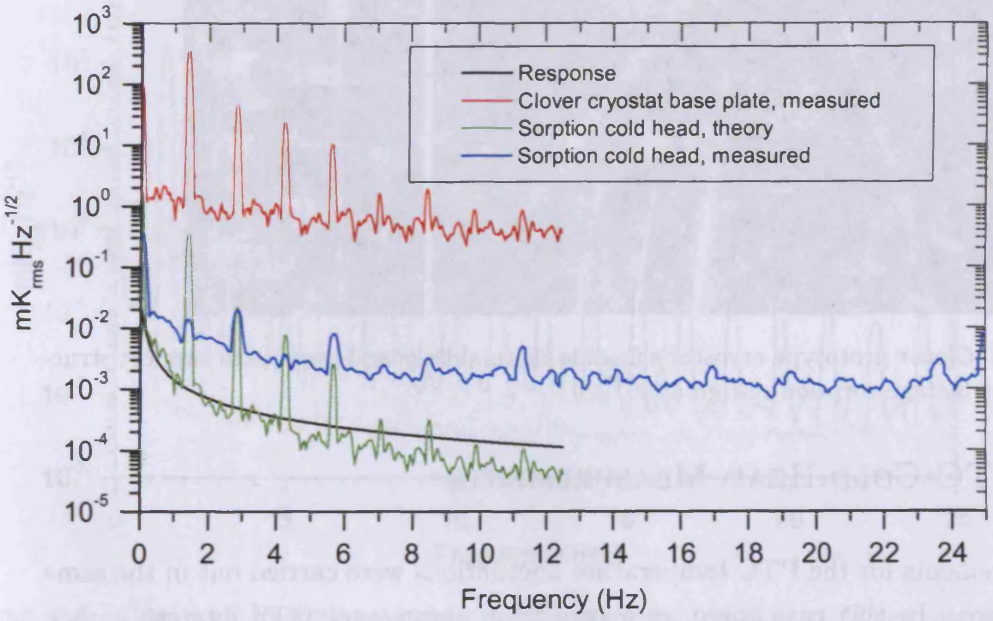

(a) Cryomech

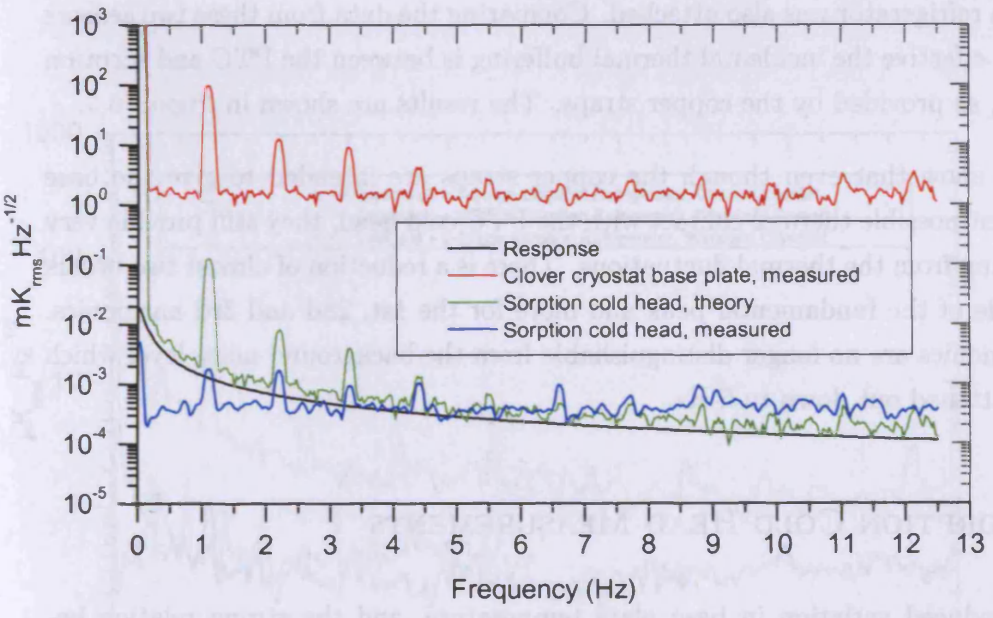

(b) VeriCold

FIGURE 6.3: The measured temperature fluctuations compared to the theoretical model in the original test bed.

FIGURE 6.4: *Clover* prototype cryostat's flexible thermal links and base plate support structure, plus the 3-stage sorption refrigerator.

6.3.1 PTC Cold-Head Measurements

The measurements for the PTC temperature fluctuations were carried out in the same way as before. In this case there were two diode thermometers of interest — one located directly on the PTC cold head, and the other on the large base plate to which the sorption refrigerator was also attached. Comparing the data from these two sensors tells us how effective the incidental thermal buffering is between the PTC and sorption refrigerator, as provided by the copper straps. The results are shown in Figure 6.5.

The results show that even though the copper straps are intended to give the base plate the best possible thermal contact with the PTC cold head, they still provide very good buffering from the thermal fluctuations. There is a reduction of almost two orders of magnitude of the fundamental peak and more for the 1st, 2nd and 3rd harmonics. Higher harmonics are no longer distinguishable from the background noise level which has been flattened out down to 6 Hz.

6.3.2 Sorption Cold Head Measurements

With this reduced variation in base plate temperature, and the strong relation between base plate and sorption cold head temperature fluctuations, there should be a very significant reduction in the sorption cold head temperature variations. These measurements were again performed with a DC bias/readout and 10 averages were taken. The results are shown in Figure 6.6 and compared to the previous setup's results for both PTCs.

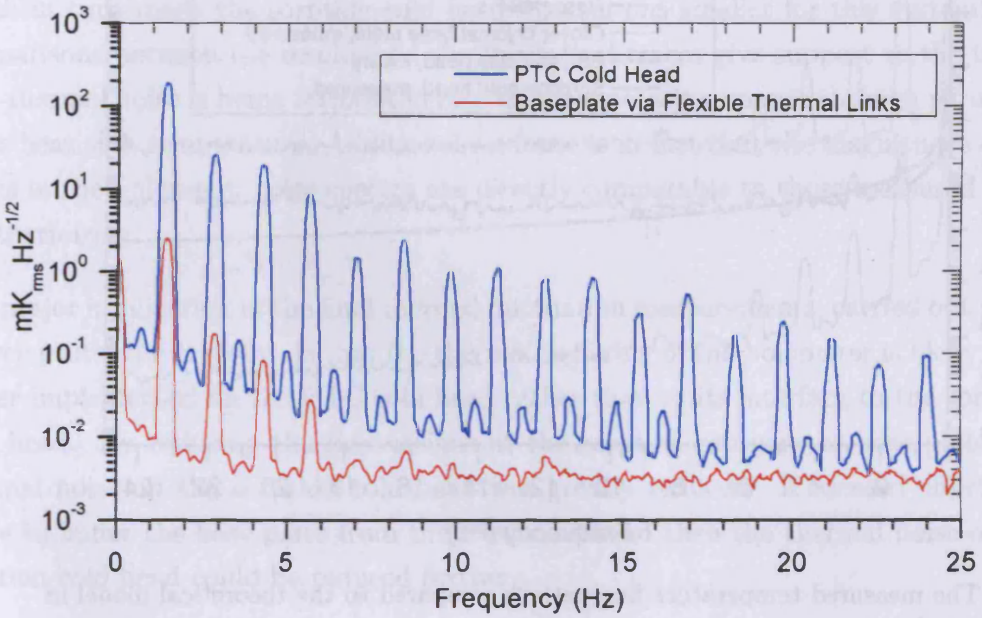

FIGURE 6.5: Cryomech PTC second stage temperature fluctuations in *Clover* prototype cryostat.

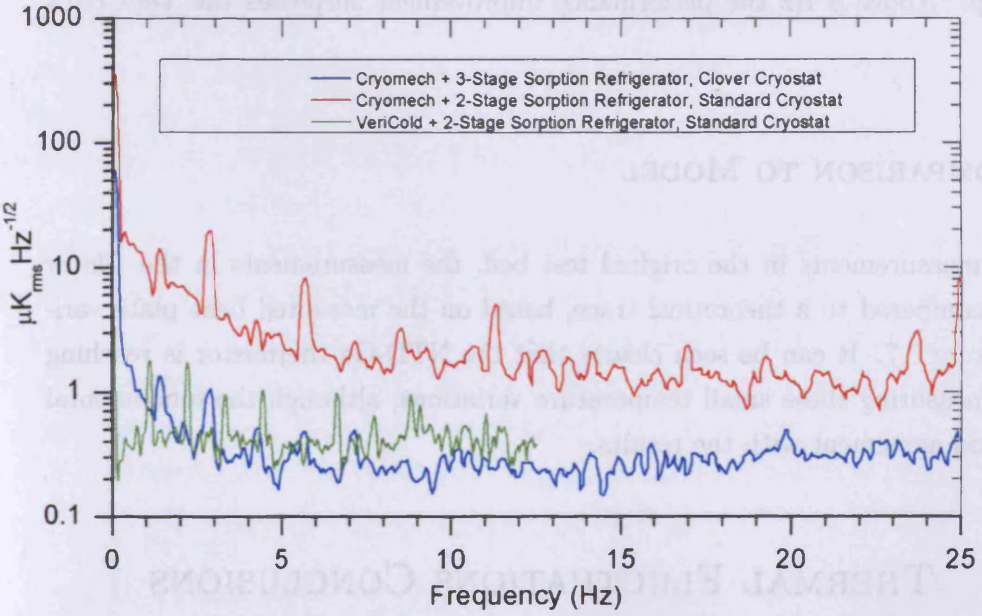

FIGURE 6.6: 3-stage sorption refrigerator cold head temperature fluctuations in *Clover* prototype cryostat. Also shown for comparison are the results for the 2-Stage version in the original setups.

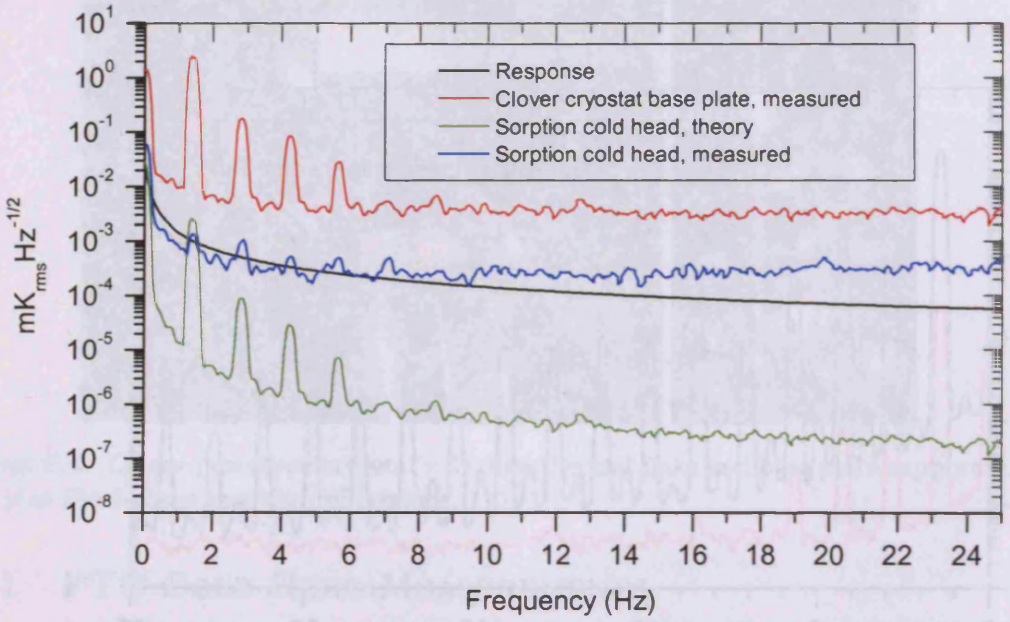

FIGURE 6.7: The measured temperature fluctuations compared to the theoretical model in the *Clover* test bed.

Following the PTC cold head results the background level has been flattened above 6 Hz where only the additional 4th harmonic is distinguishable. The fundamental was reduced to 1 μK_{pp} making it comparable in performance to the Vericold PTC in the original setup. Above 3 Hz the performance improvement surpasses the VeriCold's results.

6.3.3 Comparison to Model

As with the measurements in the original test bed, the measurements in the *Clover* cryostat are compared to a theoretical trace, based on the measured base plate variations, in Figure 6.7. It can be seen clearly that the NTD-Ge thermistor is reaching its limit for measuring these small temperature variations, although the fundamental peak is in good agreement with the results.

6.4 Thermal Fluctuations Conclusions

The poorer bolometer performance when using the Cyromech PTC system implied that the VeriCold should have lower levels of thermal noise, and this was indeed found

to be the case. The VeriCold PTC cold head temperature fluctuations were smaller, which in turn made the sorption cold head fluctuations smaller for this system. The comparisons between the results and the theoretical traces give support to the theory that thermal noise is being introduced into the bolometer's response through variations in its heat sink temperature. Additional evidence is in fact that the magnitudes of the peaks in the bolometer noise spectra are directly comparable to those measured using the thermistor.

The major implication of the final thermal fluctuation measurements, carried out in the *Clover* prototype cryostat, is that the thermal buffering of the bolometer is likely to be better implemented on the PTC cold head rather than at its interface to the sorption cold head. By reducing the fluctuations at the sorption refrigerator base plate, the thermal noise on the sorption cold head was greatly reduced. If focused efforts are made to buffer the base plate from the PTC cold head then the thermal noise on the sorption cold head could be reduced further.

Chapter 7

Discussion And Conclusions

Over the course of my study the integration of two types of bolometric detectors with pulse tube cryocoolers has been investigated. This has involved the setting up of a 300 mK test-bed by the coupling of a two-stage ^{3}He sorption refrigerator with the PTC. Electronics were constructed to automate the running of the hybrid cooler to produce a 'turn-key' cryogen free system. This concluding chapter forms a summary of my findings, with some discussion, and then puts forth the implications. Finally, an outline of possible further study is given based on these results and implications.

7.1 Summary Of Results

◇ **Turn-Key, Cryogen Free, Sub-Kelvin System**
The two-stage sorption refrigerator was successfully integrated with both commercial PTCs and performed beyond expectations with a large hold time resulting in a duty cycle of over 95%. The automated electronics produced to read the thermometry and control the sorption refrigerator have been successfully tested and released commercially. All together, the electronics, sorption refrigerator, and PTC operate as a 'turn-key' system that can achieve 300 mK within 24 hours of turning on the PTC's compressor.

◇ **300 mK NTD-Ge Bolometer**
The best NTD-Ge bolometer performance using the previously discussed countermeasures of passive thermal filtering and shielded twisted pair wiring, was approximately two times higher than the quiescent noise level. It is believed that the limiting factor

on the bolometer noise performance was a combination of the short term temperature stability of its heat sink, *ie.* the sorption refrigerator cold head, and the modulated high frequency microphonics dissipating excess electrical power. It has been shown that the heat sink temperature variations are caused by the coupling between the PTC and the sorption refrigerator, and some success in suppressing this unwanted noise can be achieved by using a passive thermal filter beneath the detector. It is hypothesised that greater success can be achieved by buffering the sorption refrigerator itself, as apposed to the detector alone. This hypothesis has been backed up by further temperature stability measurements in the *Clover* prototype cryostat as described below. The modulated high frequency microphonics however, will require significant cryostat and/or PTC modification to reduce substantially.

◇ **Dummy Resistors and Electrical Pickup**

The tests done on the dummy resistors have shown that electrical pickup in the NTD-Ge bolometer's frequency range can be rejected to satisfactory levels using shielded wiring and without mechanical modification. However, microphonic noise above one kHz is present and appears to be due to the acoustic noise of the helium gas moving within the PTC. The evidence for this is its dynamic nature and the observations of a microphone's response whilst held against the cryostat. It is not clear at present how this source of noise can be tackled without modification to the PTCs themselves.

◇ **4 K InSb HEB**

The high frequency microphonic noise was the main concern for the 4 K InSb HEB. With shielded readout wires and using the VeriCold PTC system, the detector's performance was unaffected up to 6 kHz (neglecting the thermal noise below 25 Hz) compared to its quiescent response in a 'wet' cryostat. Above this frequency the acoustic microphonic noise causes a large increase in noise level, although it is unclear whether this will drop off above the audio frequencies and into the MHz range. It is unclear whether the acoustic noise would have less effect if the detector were to be read out using a differential readout, since this noise was also present in the readout of the NTD-Ge bolometer and dummy resistors which were using a differential system. The thermal noise below 25 Hz was reduced by more than an order of magnitude by using a passive thermal filter of 185 μm Mylar.

◇ **Thermal Fluctuations**

The thermal fluctuation measurements showed the feasibility of having significant temperature variations on the sorption cold head when driven by comparatively large temperature changes on the PTC cold head. The initial tests with the Cryomech and VeriCold show that the magnitude of the sorption cold head fluctuations are approxi-

mately 2 % that of the PTC cold head variations, and varies as a square law. For the measurements carried out in the Clover cryostat this generalisation begins to break down; the buffering of the base plate in the *Clover* cryostat meant that the sorption refrigerator was subjected to temperature fluctuations more than 10 times smaller than in the Vericold setup, and yet the the sorption cold head fluctuations were only marginally smaller. It may be that heating by the high frequency microphonics became significant at this point, even for the thermistor.

When comparing the size of the measured fluctuations to those seen in the NTD-Ge and InSb bolometer's spectra using the VeriCold system we see that the bolometer's are slightly reduced because of their weak thermal link to the sorption and PTC cold heads. The NTD-Ge bolometer's fundamental peak was 0.83 $\mu K_{rms} Hz^{-0.5}$ with no Mylar filter in place, whilst the sorption cold head had a fundamental peak size of 1.9 $\mu K_{rms} Hz^{-0.5}$. The InSb HEB's fundamental peak was approximately 56 $mK_{rms} Hz^{-0.5}$ (calculated using an estimated responsivity) with no Mylar filter in place, whilst the VeriCold PTC cold head had a fundamental peak size of 100 $mK_{rms} Hz^{-0.5}$. The comparative size of the thermistor and bolometer fluctuations gives support to the theory that the peak features in the bolometer spectra are produced by a variation in heat sink temperature.

7.2 InSb Results' And Thermal Fluctuation Measurements' Implications For The NTD-Ge Bolometer

During tests on the 4 K InSb HEB it was found that the thermal peaks in its DC response could be attenuated by a factor of six for the fundamental, and more than an order of magnitude for higher harmonics, by using a 185 μm Mylar layer between it and the PTC cold head. The overall noise level was also reduced by about an order of magnitude. Given the strong dependence of the sorption refrigerator cold head temperature fluctuations on the PTC's fluctuations, it would probably have been of great benefit to the NTD-Ge bolometer if the sorption refrigerator base plate was buffered from the PTC cold head in the same way. This could be combined with a thinner buffer at the bolometer itself as had been implemented during the investigation.

At the time of the InSb HEB testing the benefit of a thermal buffer at the PTC cold head stage for an NTD-Ge bolometer was roughly estimated as follows: Comparing the

Cryomech and VeriCold temperature variations (Figure 6.1 and Figure 6.2), a factor of 3.5 difference on the PTC cold head gave a factor of 10 difference on the 300 mK stage. Extrapolating the results of the InSb detector tests therefore suggested that a buffer between the refrigerator base plate and PTC cold head would give large reductions of the 300 mK stage temperature variations; a factor of 17 for the fundamental, and almost 30 for the other harmonics and overall background level. If this were the case, then for the NTD-Ge bolometer response in Figure 4.28 the fundamental peak at just above 1 Hz would be reduced from around 2×10^{-6} $V_{rms}Hz^{-0.5}$ to about 1×10^{-7} $V_{rms}Hz^{-0.5}$, and the background level below 5 Hz would be reduced to about 6×10^{-9} $V_{rms}Hz^{-0.5}$. Note that this is actually below the expected quiescent noise level, because in reality it is only the *excess* thermal noise that is suppressed and this fact is not taken into account here. This estimation led to the explanation that a loosened thermal contact between the sorption refrigerator and its mounting bracket, occurring during repeated cool downs and warm ups, was responsible for the better bolometer performance observed in Figure 4.33.

The thermal fluctuation measurements later carried out in the *Clover* prototype cryostat revealed that reducing the PTC cold head fluctuations by a factor of 100 only resulted in a factor of 10 reduction in the sorption cold head fluctuations, at least in the case of the Cryomech PTC. Nevertheless, there are obvious benefits and advantages of this method of thermal buffering for the operation of a 300 mK bolometer.

7.3 Future Work

There is considerable scope for future studies to expand on the findings of the work presented in this thesis, particularly because of the rapidly developing detector technologies. As already pointed out, there needs to be further investigation into overcoming the temperature instabilities introduced by the use of a PTC. As well as this, the acoustic microphonic noise introduced by the He gas within the PTC has not been fully investigated since it was beyond the scope of this work to modify the PTCs themselves, and was therefore restricted to commercially available PTC systems.

In addition to passive thermal filtering, another solution to the problem of the thermal noise is the use of an active temperature control mechanism on the PTC cold head. A PID temperature control would be easier to implement on the PTC cold head than on the sorption cold head because of the larger cooling power available. If the PTC cold head temperature fluctuations can be reduced to the μK range then it should be

possible to achieve nK scale temperature stability on the sub-K cold head. Perhaps a combination of passive and active controls is the ultimate solution.

The acoustic noise could be a major consideration for newer and faster technologies that are rapidly replacing NTD-Ge bolometers, rather than the low frequency temperature variations. For example, TES devices which have characteristic response times of 1000 down to 100 μs (one to ten kHz), are being implemented on most ground based experiments and also bring other issues that need to be addressed. Their readout requires magnetic shielding because of the SQUID amplifier, and it is known that some PTC designs use materials with residual magnetic fields as part of their regenerators and tube construction. However, temperature stability still remains an issue for experiments requiring the high sensitivity made possible with technologies such as TES devices. Future CMB polarisation experiments require temperature fluctuations no larger than 60 $nK_{rms}Hz^{-0.5}$ at 100 mK in order to get the most benefit out of the new detectors.

It has been claimed by the bolometer group in Berkeley through private communications [45] that TES devices can operate at their nominal noise level within a PTC pre-cooled system. Nevertheless, future work should look into the issues of operating TES devices at a range of temperatures, as well as the general development of PTC based cryogenic systems (Dilution refrigerators and ADR) with attention paid to system level integration with these detectors. This is important both because helium is a limited natural resource, and the use of mechanical coolers in general will ease the operation of instruments in remote locations and extend the lifetime of space based instruments. Bearing in mind that new low impedance detectors are less susceptible to microphonics but more susceptible to stray magnetic fields, the importance of transmitted EMI and the subsequent needs for magnetic shielding should be properly assessed, and possible alternatives to magnetic regenerator materials considered.

APPENDICES

Appendix A

THERMODYNAMICS

A.1 IDEAL STIRLING AND ERICSSON CYCLES

Nomenclature

Q — Heat entering/leaving system,

U — Internal energy,

W — Net work performed by the system,

T — Temperature

S — Entropy

P — Pressure

V — Volume

H — Enthalpy

The use of lower case letters indicates that the quantity is for unit mass.

The work term for the ideal Stirling and Ericsson cycles remains the same as the Carnot cycle because the reversible isobaric and isochoric processes trace out parallel lines (although not straight as depicted in the simplified Figure 1.3) on the T-S diagram, and hence the enclosed area remains unaffected. To show this we only have to use the First Law of thermodynamics (in differential form), plus the definition of enthalpy, and the heat capacities at constant volume and pressure.

Substituting $\delta Q = TdS$ and $\delta W = PdV$ into the First Law,

(A.1a) $$\delta Q = dU + \delta W \qquad [J]$$

(A.1b) $$TdS = dU + PdV$$

Or in specific form,

(A.2) $$Tds = du + Pdv \qquad [\mathrm{Jkg^{-1}}]$$

For an isochoric process $dv = 0$, and the specific heat at constant volume is $c_v = du/dT$, hence,

(A.3a) $$Tds = c_v dT \qquad [\mathrm{Jkg^{-1}}]$$

(A.3b) $$\frac{dT}{ds} = \frac{T}{c_v} \qquad [\mathrm{K^2 kgJ^{-1}}]$$

Therefore lines of constant volume are parallel on a temperature-entropy diagram, with a slope T/c_v.

For an isobaric process we must consider the enthalpy of the system instead of its internal energy. Differentiating the definition of enthalpy,

(A.4a) $$H = U + PV \qquad [\mathrm{J}]$$

(A.4b) $$dH = dU + PdV + VdP$$

and substituting for $dU + PdV$ in Equation A.1b gives

(A.5) $$TdS = dH - VdP \qquad [\mathrm{J}]$$

Or in specific form,

(A.6) $$Tds = dh - vdP \qquad [\mathrm{Jkg^{-1}}]$$

In an isobaric process $dP = 0$, and the specific heat at constant pressure is $c_p = \frac{dh}{dT}$, hence,

(A.7a) $$Tds = c_p dT \qquad [\mathrm{Jkg^{-1}}]$$

(A.7b) $$\frac{dT}{ds} = \frac{T}{c_p} \qquad [\mathrm{K^2 kgJ^{-1}}]$$

Therefore lines of constant pressure are also parallel on a temperature-entropy diagram, with a slope $\frac{T}{c_p}$.

The fact that these isochoric and isobaric lines are parallel means that the processes 2–3', 2–3", 4'–1, and 4"–1, in Figure 1.3 are equal and opposite and the net work remains unchanged from that of the Carnot cycle.

A.2 Dependence of Cooling Power on Phase Angle

The cooling power of Pulse Tube Cryocoolers (PTCs) is largely determined by the time averaged (over the course of a thermodynamic cycle) enthalpy flow in the pulse tube part of the cryocooler which, assuming an ideal gas, is given by,

$$\langle \dot{H} \rangle = \frac{C_p}{\tau} \int_0^\tau \dot{m} T \, dt \qquad \text{[W]} \tag{A.8}$$

where $\langle \dot{H} \rangle$ is the time averaged enthalpy flow, C_p is the molar specific heat at constant pressure, τ is the time period for one thermodynamic cycle, $\dot{m}$ is the mass flow rate of the working fluid (helium gas), T is the temperature and t is time.

The mass flow rate depends on the density, ρ, the pulse tube sectional area, A, and the working fluid's velocity, u,

$$\dot{m} = \rho A u \qquad \text{[mol s}^{-1}\text{]} \tag{A.9}$$

and the density is given by the equation of state, in this case for an ideal gas,

$$\rho = \frac{P}{RT} \qquad \text{[mol m}^{-3}\text{]} \tag{A.10}$$

where P is the pressure, and R is the gas constant.

Substituting Equation A.9 and Equation A.10 into Equation A.8 gives

$$\langle \dot{H} \rangle = \frac{C_p A}{R\tau} \int_0^\tau u P \, dt \qquad \text{[W]} \tag{A.11}$$

Assuming sinusoidal variations in the pressure ($P = \bar{P} + \Delta P \sin \omega t$, where $\bar{P}$ is the mean pressure, ΔP is the amplitude of the pressure oscillations and ω is the angular frequency of the oscillations) and fluid velocity ($u = u_0 \sin(\omega t - \phi)$, where u_0 is the maximum velocity amplitude and ϕ is the phase angle between the mass flow in the tube and the pressure oscillations) we will now go on to show how when averaged over one cycle, the cooling power (enthalpy flow) depends only on the time varying

amplitudes and the phase angle.

$$\text{(A.12a)}\quad \langle \dot{H} \rangle = \frac{C_p A u_0}{R\tau} \int_0^\tau \sin(\omega t - \phi)[\bar{P} + \Delta P \sin \omega t] dt \qquad [\text{W}]$$

$$\text{(A.12b)}\quad = \frac{C_p A u_0}{R\tau} \int_0^\tau \underbrace{\bar{P} \sin(\omega t - \phi)}_{X} + \underbrace{\Delta P \sin \omega t \sin(\omega t - \phi)}_{Y} \, dt$$

Solving each integral term, X and Y, separately:

$$\begin{aligned} X &= \int_0^\tau \bar{P}[\sin(\omega t)\cos(-\phi) + \cos(\omega t)\sin(-\phi)] dt \\ &= \bar{P} \int_0^\tau \cos(\phi)\sin(\omega t) - \sin(\phi)\cos(\omega t)\, dt \\ &= \frac{\bar{P}}{\tau\omega}[-\cos(\phi)\cos(\omega t) - \sin(\phi)\sin(\omega t)]_{t=0}^{\tau} \\ &= \frac{-\bar{P}}{2\pi}[\{\cos(\phi)\cos(2\pi) + \sin(\phi)\sin(2\pi)\} - \{\cos(\phi)\cos(0) + \sin(\phi)\sin(0)\}] \\ \text{(A.13)}\quad &= 0 \end{aligned}$$

$$\begin{aligned} Y &= \int_0^\tau \Delta P[\sin(\omega t)\sin(\omega t)\cos(\phi) + \sin(\omega t)\cos(\omega t)\sin(-\phi)] dt \\ &= \frac{\Delta P}{2} \int_0^\tau \cos(\phi)[1 - \cos(2\omega t)] - \sin(\phi)\sin(2\omega t)\, dt \\ &= \frac{\Delta P}{2} \left[t\cos(\phi) - \frac{\cos(\phi)}{2\omega}\sin(2\omega t) + \frac{\sin(\phi)}{2\omega}\cos(2\omega t) \right]_{t=0}^{\tau} \\ &= \frac{\Delta P}{2} \left[\left\{ \tau\cos(\phi) - \frac{\cos(\phi)}{2\omega}\sin(4\pi) + \frac{\sin(\phi)}{2\omega}\cos(4\pi) \right\} \right. \\ &\qquad \left. - \left\{ 0 - \frac{\cos(\phi)}{2\omega}\sin(0) + \frac{\sin(\phi)}{2\omega}\cos(0) \right\} \right] \\ &= \frac{\Delta P}{2} \left[\tau\cos(\phi) + \frac{\sin(\phi)}{2\omega} - \frac{\sin(\phi)}{2\omega} \right] \\ \text{(A.14)}\quad &= \frac{1}{2}\Delta P \tau \cos(\phi) \end{aligned}$$

Substituting Equation A.13 and Equation A.14 into Equation A.12b gives the result

$$\text{(A.15)}\qquad \langle \dot{H} \rangle = \frac{1}{2}\frac{C_p A}{R} u_0 \Delta P \cos(\phi) \qquad [\text{W}]$$

and it can be seen that there is no contribution from the average pressure and that the maximum enthalpy flow occurs for $\phi = 0$.

Appendix B

Bolometric Detectors

B.1 Basic Model for the Responsivity of a Semiconductor Bolometer

This model is based on that presented by Richards [31] and refers to Figure 1.8.

B.1.1 Absorbed Power Responsivity, S_A

We define the incident radiation power as a mean value plus a sinusoidal variation that the bolometer responds to:

$$Q = Q_0 + Q_1 e^{i\omega_s t} \quad \text{[W]} \tag{B.1}$$

with $e^{i\omega_s t}$ being the time variation at angular frequency ω_s. Likewise, the resulting temperature variation of the bolometer is,

$$T_B = T_0 + T_1 e^{i\omega_s t} \quad \text{[K]} \tag{B.2}$$

We assume that there is enough cooling power in the heat sink for it's temperature to remain constant. Since the temperature of the thermistor is changing, it's change in resistance will vary the dissipated electrical power accordingly:

$$P = I^2 \left[R(T_0) + \left(\frac{dR}{dT} \right) T_1 e^{i\omega_s t} \right] \quad \text{[W]} \tag{B.3}$$

Here we have used a first order Taylor expansion and also assumed that the current, I, is constant. This is a reasonable approximation since the load resistance is usually a lot larger than the bolometer's resistance. The power lost to the heat sink is,

$$\bar{G}(T_B - T_S) = \bar{G}(T_0 - T_S) + GT_1 e^{i\omega_s t} \quad \text{[W]} \tag{B.4}$$

Again, this uses a first order Taylor expansion with $G = dW/dT$ being defined as the dynamic conductance, and $\bar{G}$ being the average conductance taking into account the variation of the thermal conductivity over the relevant temperature range. The energy from the time varying part of the incident radiation going into the heat capacity is $CT_1 e^{i\omega_s t}$. Differentiating with respect to time gives the component of the power going into the heat capacity, $i\omega_s CT_1 e^{i\omega_s t}$.

We now consider the dynamic energy balance equation that equates the total input power, $W = P + Q$, to the power lost through the thermal link plus the power going into the heat capacity:

$$\begin{aligned} &Q_0 + Q_1 e^{i\omega_s t} + I^2 R(T_0) + I^2 \left(\frac{dR}{dT}\right) T_1 e^{i\omega_s t} \\ &= \bar{G}(T_0 - T_S) + GT_1 e^{i\omega_s t} + i\omega_s CT_1 e^{i\omega_s t} \end{aligned} \tag{B.5}$$

The time dependent and time independent terms can now be equated separately. The time independent terms can tell us nothing about the response of the bolometer, but do give it's average operating temperature, T_0.

$$Q_0 + I^2 R(T_0) = \bar{G}(T_0 - T_S) \tag{B.6a}$$

$$\Rightarrow \qquad T_0 = T_S + \frac{Q_0 + I^2 R(T_0)}{\bar{G}} \quad \text{[K]} \tag{B.6b}$$

This is equivalent to Equation 1.6 on page 23.

The absorbed power (voltage) responsivity is defined as,

$$S_A = dV/dQ \quad \text{[VW}^{-1}\text{]} \tag{B.7a}$$

$$= V_1/Q_1 \tag{B.7b}$$

$$= I\frac{dR}{dT}\frac{T_1}{Q_1} \tag{B.7c}$$

Equating the time dependent terms of Equation B.5 and dividing by $T_1 e^{i\omega_s t}$,

(B.8a) $$Q_1 e^{i\omega_s t} + I^2 \left(\frac{dR}{dT}\right) T_1 e^{i\omega_s t} = G T_1 e^{i\omega_s t} + i\omega_s C T_1 e^{i\omega_s t}$$

(B.8b) $$\Rightarrow \qquad \frac{Q_1}{T_1} = G - I^2 \frac{dR}{dT} + i\omega_s C$$

Inverting Equation B.8b and multiplying by $I\frac{dR}{dT}$ gives us the result (along with alternate expressions),

(B.9a) $$S_A = \frac{I dR/dT}{G - I^2 dR/dT + i\omega_s C} \qquad [\mathrm{VW^{-1}}]$$

(B.9b) $$= \frac{\alpha V}{G - \alpha P + i\omega_s C}$$

(B.9c) $$= \frac{\alpha V}{G_e + i\omega_s C}$$

(B.9d) $$= \frac{\alpha V}{G_e(1 + i\omega_s \tau_e)}$$

Where $G_e = G - \alpha P$ is defined as the effective thermal conductance, and $\tau_e = C/G_e$ is the measured effective time constant.

B.1.2 Electrical Responsivity, S_E

Considering the case with no time varying radiation ($\omega_s = 0$), Equation B.9b becomes,

(B.10) $$S_E = \frac{\alpha V}{G - \alpha P} \qquad [\mathrm{VW^{-1}}]$$

To put in a form that only contains quantities measurable from the load curve, we need to find an expression for G. This is done by eliminating dT in the two expressions,

(B.11a) $$G dT = dP \qquad [\mathrm{W}]$$

(B.11b) $$= d(IV)$$

(B.11c) $$= I dV + V dI$$

(since $dW = dP + dQ$ and $dQ = 0$ for the case of no optical power) and,

$$dV = d(IR) \quad [\text{V}] \tag{B.12a}$$
$$= RdI + IdR \tag{B.12b}$$
$$= RdI + IR\alpha dT \tag{B.12c}$$
$$= RdI + \alpha V dT \tag{B.12d}$$

Substituting for dT in Equation B.11c and rearranging for G:

$$G\frac{dV - RdI}{\alpha V} = IdV + VdI \tag{B.13a}$$
$$G\frac{Z - R}{\alpha V} = IZ + V \tag{B.13b}$$
$$G = \frac{\alpha V(IZ + V)}{Z - R} \quad [\text{WK}^{-1}] \tag{B.13c}$$

where $Z = dV/dI$ is the dynamic impedance of the detector. This can now be substituted into Equation B.10 and simplified:

$$S_E = \frac{\alpha V}{\frac{\alpha V(IZ+V)}{Z-R} - \alpha P} \quad [\text{VW}^{-1}] \tag{B.14a}$$
$$= \frac{V(Z - R)}{V(IZ + IR) - P(Z - R)} \tag{B.14b}$$
$$= \frac{Z - R}{IZ + IR - IZ + IR} \tag{B.14c}$$
$$= \frac{Z - R}{2IR} \tag{B.14d}$$

B.2 Dynamic Bolometer Model

The C++ code below simulates an NTD-Ge bolometer's response to a step change in bias voltage. It also produces theoretical load curves at a specified heat sink temperature.

```
#include <cstdlib>
#include <iostream>
#include <math.h>

using namespace std;
```

```
class bolometer{
    public:                          //Functions accessible to main program
        bolometer(float, float, float);                    //Constructor
        bolometer(float, float);                 //Alternative constructor
                                                          //full constructor
        bolometer(float, float, float, float, float, float, float);
        bolometer();                                  //Default constructor
        void define();                          //Define parameters function
        void printinfo();                                     //Print info
        void loadcurve(float);                   //Synthesise a load curve
            //Create time stream for bolometer repsonse to stepped bias
        void timestream(float, float, float);
                               //function to find phi for a given bias V
        float getphi(float, float);
        void setheatcap();

    private:                                          //Bolometer parameters
        float RStar,    //Ohms                 //NTD resistance parameters
              Tg,       //Kelvin
              n,
              beta,    //Material parameter (thermal conductivity index)
              Ts,                        //Heat sink temperature for Gs(K)
             //Static thermal conductance at heat sink temperature (W/K)
              Gs,
              TsC,                                  // Heat sink temp for C
              Cs,                // Heat Capacity at heat sink temp. (J/K)
              betaC,
              RL;                                   //Load resistance (Ohms)
};

//Constructors:
bolometer::bolometer(float input1, float input2, float input3){
    RStar = input1;
    Tg = input2;
    n = input3;
}

bolometer::bolometer(float input1, float input2){
```

```
    RStar = input1;
    Tg = input2;
    n = 0.5;
}

bolometer::bolometer(float input1, float input2, float input3,
                float input4, float input5, float input6, float input7){
    RStar = input1;
    Tg = input2;
    n = input3;
    beta = input4;
    Ts = input5;
    Gs = input6;
    RL = input7;
}

bolometer::bolometer(){
    RStar = 0;
    Tg = 0;
    n = 0;
}

void bolometer::printinfo(){//Print basic bolometer parameters
    cout << "R_* = " << RStar << " Ohms" << endl;
    cout << "T_g = " << Tg << " K" << endl;
    cout << "n = " << n << endl;
    cout << "beta = " << beta << endl;
    cout << "G_s = " << Gs/1e-12 << " pW/K at T_s = " << Ts << " K\n";
    cout << "R_L = "<< RL/1e6<<" MOhms\n";
    cout << endl;
}

void bolometer::define(){//define bolometer parameters
    cout << "Define NTD's resistance parameters.\n";
    cout << "Enter value for R_* (Ohms):\n";
    cin >> RStar;
    cout <<"Enter value for T_g (K):\n";
    cin >> Tg;
```

```
    cout <<"Enter value for n:\n";
    cin >> n;
    cout << "\nDefine thermal properties.\n"<<"Enter value for beta:\n";
    cin >> beta;
    cout << "Enter value for G_s (W/K):\n";
    cin >> Gs;
    cout << "Enter corresponding value for T_s (K):\n";
    cin >> Ts;
    cout<<"\nDefine readout parameters.\nEnter value for R_L (Ohms):\n";
    cin >> RL;
}

//synthesise a load curve
//for current parameter values or new temperature
void bolometer::loadcurve(float T0){
    cout << "\nLoad curve using parameters:\n";
    cout << "Heat sink temperature = " << T0 << " K\n";
    printinfo();

    //calculate Gs for specified heat sink temperature
    float Gs0 = Gs * pow(T0/Ts, beta);
    cout << "G_s for T_s = " << T0 << " K is " << Gs0/1e-12
         << " pW/K\n\n";

    float phi=1, phimax=1.5;          //dimensionless temperature = T/Ts
    int i, nsteps=100;
    //Define range of T (phi)
    float P=0,I=0,V=0,R=0;

    //Increment T (phi) and calculate P, I and V at each point
    cout << "I (nA),    V (mV),    phi,       P (pW),    R (MOhms)\n\n";
//    cout << "*********************************************\n";
    for (i = 1; i <= nsteps ; ++i){
        P = ((Gs0*T0)/(beta + 1))*(pow(phi,beta + 1) - 1);
        R = RStar * exp(pow(Tg/(phi*T0),n));
        I = sqrt(P/R);
        V = sqrt(P*R);
        cout<<I/1e-9<<",   "<<V/1e-3<<",   "<<phi<<",   "<<P/1e-12
```

```
            <<",   "<<R/1e6<<endl;
        phi += (phimax - 1)/(nsteps-1);
        }
}

//find equilibrium phi for a given bias V
float bolometer::getphi(float T0, float VBias){
    //controls:
    float acc = 0.0001; //percentage accuracy
    //calculate Gs for specified heat sink temperature
    float Gs0 = Gs * pow(T0/Ts, beta);
    float A = 1, B = 2, phi; //initial guesses
    float R,I,P,W,fA,fB,fphi;

    //Binary chopping method:
    while ( (200*(B-A)/(B+A)) > acc){
        phi=A;
        R = RStar * exp(pow(Tg/(phi*T0),n));
        I = VBias/(R + RL);
        //electrical power
        P = I*I*R;
        //thermal link power
        W = ((Gs0*T0)/(beta + 1))*(pow(phi,beta + 1) - 1);
        fA = P-W;

        phi=B;
        R = RStar * exp(pow(Tg/(phi*T0),n));
        I = VBias/(R + RL);
        P = I*I*R;
        W = ((Gs0*T0)/(beta + 1))*(pow(phi,beta + 1) - 1);
        fB = P-W;

        phi = 0.5*(A + B);
        R = RStar * exp(pow(Tg/(phi*T0),n));
        I = VBias/(R + RL);
        P = I*I*R;
        W = ((Gs0*T0)/(beta + 1))*(pow(phi,beta + 1) - 1);
        fphi = P-W;
```

```
        if (fA*fB > 0){
            cout << "Cannot converge!";
            break;
        } else
        if (fphi*fA > 0) A = phi; else B = phi;
    }

    phi = 0.5*(A + B);
//    R = RStar * exp(pow(Tg/(phi*T0),n));
//    I = VBias/(R + RL);
//    P = I*I*R;
//    W = ((Gs0*T0)/(beta + 1))*(pow(phi,beta + 1) - 1);
//    cout << P << "  "<< W<<"  \n";
    return phi;
}

//synthesise bolometer response to change in bias
void bolometer::timestream(float T0, float V0, float DeltaV){
    //controls:
    float t=0, dt = 0.1e-3; //time step
    float acc = 0.001; //Accuracy. Percentage change in V at the end.
    float R,I,V,P,W,C,dphi,VPrev;
    //calculate Gs for specified heat sink temperature:
    float Gs0 = Gs * pow(T0/Ts, beta);
    //calculate Cs for specified heat sink temperature:
    float Cs0 = Cs * pow(T0/TsC, betaC);

    //calculate conditions before step:
    float phi = getphi(T0, V0);
    R = RStar * exp(pow(Tg/(phi*T0),n));
    I = V0/(R + RL);
    V = I*R;

    cout << endl
         << "t (ms),     V (mV),     I (nA),     R (MOhms),  phi\n\n"
         <<t/1e-3<<",   "<<V/1e-3<<",   "<<I/1e-9<<",   "<<R/1e6
         <<",   "<<phi<<endl;
```

```
    //Loop:
    int i=-1;
    do{
        i++;
        VPrev = V;
        I = (V0 + DeltaV)/(R + RL);
        V = I*R;

        P = I*I*R;
        W = ((Gs0*T0)/(beta + 1))*(pow(phi,beta + 1) - 1);
        C = Cs0*pow(phi,betaC);
        dphi = ((P - W)/C)*dt;

        if (i==20){
            cout <<t/1e-3<<",   "<<V/1e-3<<",   "<<I/1e-9<<",   "
                 <<R/1e6<<",   "<<phi<<endl;
            i=0;
        }

        phi += dphi;
        t += dt;
        R = RStar * exp(pow(Tg/(phi*T0),n));

    } while ( 200*fabs((VPrev - V)/(VPrev + V)) > acc );
}

void bolometer::setheatcap(){
  char choice='a';
  while(choice != 'n'){
     cout <<"\nCurrent heat capacity parameters:\n"
          <<"C_s = "<<Cs/1e-12<<" pJ/K, at T_s = "<<TsC<<" K.\n"
          <<"beta_C = "<<betaC<<"\n"
          <<"Redefine? (y/n):\n";
     cin  >>choice;
     if (choice == 'y'){
       cout <<"\nEnter value for C_s (pJ/K):\n";
       cin >> Cs;
```

```
        Cs *= 1e-12;
        cout <<"Enter corresponding value for T_s (K):\n";
        cin >> TsC;
        cout<<"Enter value for the heat capacity's power law, beta_C:\n";
        cin >> betaC;
      }
   }

}

//////////////main program:////////////////////////
int main(int argc, char *argv[])
{
//    //Test code:
//    bolometer mybol;
//    cout << "Test bolometer:\n\n";
//    mybol.define();
//    mybol.printinfo();

    //Bolometer used in thesis work:
    bolometer OrlandoBol(27.2, 56.5, 0.5, 1.7, 0.355, 1960e-12, 80e6);

    int choice=-1;
    while (choice != 0){
        cout << "\nCurrent bolometer parameters:\n\n";
        OrlandoBol.printinfo();
        cout << "MENU\n"
                "----\n"
                "1: Redefine bolometer parameters\n"
                "2: Synthesise load curve\n"
                "3: Create time stream\n"
                "0: Exit\n\n"
                "Enter option: ";
        cin >> choice;
        if (choice ==1){
            OrlandoBol.define();
        }
        if (choice == 2){
```

```
            float T0;
            cout<<"\nEnter heat sink temperature for load curve (K): ";
            cin >> T0;
            OrlandoBol.loadcurve(T0);
        }
        if (choice ==3){
            float T0, V0, DeltaV;
            cout<<"\nEnter heat sink temperature for time stream (K): ";
            cin >> T0;
            cout << "\nEnter start bias voltage (V): ";
            cin >> V0;
            cout << "\nEnter bias step (voltage change) (V): ";
            cin >> DeltaV;
            OrlandoBol.setheatcap();
            OrlandoBol.timestream(T0, V0, DeltaV);
        }
    }
    return EXIT_SUCCESS;
}
```

Appendix C

Example TINI Code

```
<?xml version="1.0"?>

<!-- Trial Dewar definition - Simon Melhuish -->
<!-- Latest Changes 18/08/04 (Gareth): -->
<!-- Reduced regression calculation times back to 5 minute-->
<!-- Changed fast start 4He temp to 45K for better condensing-->
<!-- Changes 19/01/05 (Gareth): -->
<!-- Added auto recycle state -->
<!-- Changes 18/05/05 (Gareth): -->
<!-- Revised heater channel #'s for new thermometry box -->

<dewar>
<defaultstate>idle</defaultstate>
<state name="idle">
<actions>
<message>Idle</message>
</actions>
<!-- This is the idle state.  Do nothing.  Wait for nothing.  -->
</state>

<state name="precool">
<actions>
<message> System is pre-cooling</message>
<heater chan="1" V="3.0"/> <!-- H4 - 4He pump -->
<heater chan="2" V="5.0"/> <!-- H3 - 3He pump -->
<heater chan="3" V="0.0"/> <!-- HS4 - 4He switch -->
<heater chan="4" V="0.0"/> <!-- HS3 - 3He switch -->
</actions>
<tests>
<if goto="start">
```

```
<and>
<diode chan="2" greaterthan="1.22913"/><!-- 3.05 K -->
<grt chan="1" greaterthan="147"/><!-- < 3 K -->
</and>
</if>
</tests>
</state>

<state name="start">
<!-- This is where we start recycling.  Turn off everything -->
<actions>
<message>Start fridge cycle</message>
<heater chan="1" V="3.0"/> <!-- H4 - 4He pump -->
<heater chan="2" V="5.0"/> <!-- H3 - 3He pump -->
<heater chan="3" V="0.0"/> <!-- HS4 - 4He switch -->
<heater chan="4" V="0.0"/> <!-- HS3 - 3He switch -->
</actions>
<tests>
<if goto="heat4He">
<!-- Allow 2 mins for heat switches to go off -->
<timeout time="10" since="start"/>
</if>
</tests>
</state>

<state name="faststart">
<!-- This is where we start recycling.  Turn off everything -->
<actions>
<message>Execute a fast start from "cold"</message>
<heater chan="1" V="15.0"/> <!-- H4 - 4He pump -->
<heater chan="2" V="5.0"/> <!-- H3 - 3He pump -->
<heater chan="3" V="0.0"/> <!-- HS4 - 4He switch -->
<heater chan="4" V="0.0"/> <!-- HS3 - 3He switch -->
</actions>
<tests>
<if goto="start">
<!-- Allow 2 mins for heat switches to go off -->
<diode chan="3" lessthan="1.078"/>
<!-- wait for > ~45 K -->
</if>
</tests>
</state>

<state name="heat4He">
<!-- Wait in case 4He not hot enough yet -->
<actions>
<message>Started condense 4He</message>
```

```
<heater chan="1" V="5.0"/> <!-- H4 - 4He pump -->
<heater chan="2" V="5.0"/> <!-- H3 - 3He pump -->
<heater chan="3" V="0.0"/> <!-- HS4 - 4He switch -->
<heater chan="4" V="0.0"/> <!-- HS3 - 3He switch -->
</actions>
<tests>
<if goto="condense4">
<diode chan="3" lessthan="1.103"/>
<!-- wait for > 30 K -->
</if>
</tests>
</state>

<state name="condense4">
<!-- Wait for 4He to condense - heater already hot -->
<actions>
<message>Waiting for 4He condensation</message>
<heater chan="1" V="3.0"/> <!-- H4 - 4He pump -->
<heater chan="2" V="5.0"/> <!-- H3 - 3He pump -->
<heater chan="3" V="0.0"/> <!-- HS4 - 4He switch -->
<heater chan="4" V="0.0"/> <!-- HS3 - 3He switch -->
</actions>
<tests>
<if goto="pump4">
<!-- Wait 5min for He to condense -->
<timeout time="300" since="condense4"/>
</if>
</tests>
</state>

<state name="pump4">
<!-- Start to pump 4He, by turning off H4 and turning on HS4 -->
<actions>
<message>Started pump 4He</message>
<heater chan="1" V="0.0"/> <!-- H4 - 4He pump -->
<heater chan="2" V="5.0"/> <!-- H3 - 3He pump -->
<heater chan="3" V="3.0"/> <!-- HS4 - 4He switch -->
<heater chan="4" V="0.0"/> <!-- HS3 - 3He switch -->
</actions>
<tests>
<if goto="heat3He">
<!-- Normally we will wait a set time to start condensing 3He -->
<timeout time="300" since="pump4"/>
</if>
</tests>
</state>
```

```
<state name="heat3He">
<!-- Start to condense 3He, by turning up the heater -->
<actions>
<message>Started condense 3He</message>
<!-- Heater 4 is 3He -->
<heater chan="1" V="0.0"/> <!-- H4 - 4He pump -->
<heater chan="2" V="10.0"/> <!-- H3 - 3He pump -->
<heater chan="3" V="3.0"/> <!-- HS4 - 4He switch -->
<heater chan="4" V="0.0"/> <!-- HS3 - 3He switch -->
</actions>
<tests>
<if goto="condense3">
<!-- Wait 1000s for T to rise, and He to start condensing -->
<timeout time="1000" since="heat3He"/>
<diode chan="4" lessthan="1.07"/>
<!-- wait for > 50 K -->
</if>
</tests>
</state>

<state name="condense3">
<!-- Set normal condensation voltage -->
<actions>
<message>Waiting for 3He condensation</message>
<!-- Heater 4 is 3He -->
<heater chan="1" V="0.0"/> <!-- H4 - 4He pump -->
<heater chan="2" V="5.0"/> <!-- H3 - 3He pump -->
<heater chan="3" V="3.0"/> <!-- HS4 - 4He switch -->
<heater chan="4" V="0.0"/> <!-- HS3 - 3He switch -->
</actions>
<tests>
<if goto="Wait4He">
<!-- Wait 2min to settle -->
<timeout time="120" since="condense3"/>
</if>
</tests>
</state>

<state name="Wait4He">
<actions>
<message>Waiting for 4He to cool</message>
<heater chan="1" V="0.0"/> <!-- H4 - 4He pump -->
<heater chan="2" V="5.0"/> <!-- H3 - 3He pump -->
<heater chan="3" V="3.0"/> <!-- HS4 - 4He switch -->
<heater chan="4" V="0.0"/> <!-- HS3 - 3He switch -->
</actions>
<tests>
```

```
<if goto="Wait4HeEx">
<or>
<grtdot chan="1" lessthan="0" samples="300"/>
<!-- wait for temp to flatten out -->
<grt chan="1" greaterthan="875"/>
<!-- wait for < 0.95K -->
</or>
</if>
</tests>
</state>

<state name="Wait4HeEx">
<actions>
<message>Waiting for 4He exhaustion</message>
<heater chan="1" V="0.0"/> <!-- H4 - 4He pump -->
<heater chan="2" V="5.0"/> <!-- H3 - 3He pump -->
<heater chan="3" V="3.0"/> <!-- HS4 - 4He switch -->
<heater chan="4" V="0.0"/> <!-- HS3 - 3He switch -->
</actions>
<tests>
<if goto="pump3">
<grtdot chan="1" lessthan="-0.042" samples="300"/>
<!-- wait sharp temperature rise -->
</if>
</tests>
</state>

<state name="pump3">
<!-- Start to pump 3He, by turning off H3 and turning on HS3 -->
<actions>
<message>Started pump 3He</message>
<heater chan="1" V="0.0"/> <!-- H4 - 4He pump -->
<heater chan="2" V="0.0"/> <!-- H3 - 3He pump -->
<heater chan="3" V="3.0"/> <!-- HS4 - 4He switch -->
<heater chan="4" V="3.0"/> <!-- HS3 - 3He switch -->
</actions>
<tests>
<if goto="running">
<grt chan="1" greaterthan="23000"/> <!-- 0.351 K -->
</if>
</tests>
</state>

<state name="running">
<actions>
<message>Fridge cold!</message>
<heater chan="1" V="0.0"/> <!-- H4 - 4He pump -->
```

```
<heater chan="2" V="0.0"/> <!-- H3 - 3He pump -->
<heater chan="3" V="3.0"/> <!-- HS4 - 4He switch -->
<heater chan="4" V="3.0"/> <!-- HS3 - 3He switch -->
</actions>
</state>

<state name="AutoRecycle">
<!-- Put into this state when running, to automatically recycle fridge -->
<actions>
<message>Ready to auto recycle</message>
<heater chan="1" V="0.0"/> <!-- H4 - 4He pump -->
<heater chan="2" V="0.0"/> <!-- H3 - 3He pump -->
<heater chan="3" V="3.0"/> <!-- HS4 - 4He switch -->
<heater chan="4" V="3.0"/> <!-- HS3 - 3He switch -->
</actions>
<tests>
<if goto="faststart">
<grt chan="1" lessthan="800"/> <!-- about 1 K -->
</if>
</tests>
</state>

</dewar>
```

Appendix D

Circuit Diagrams

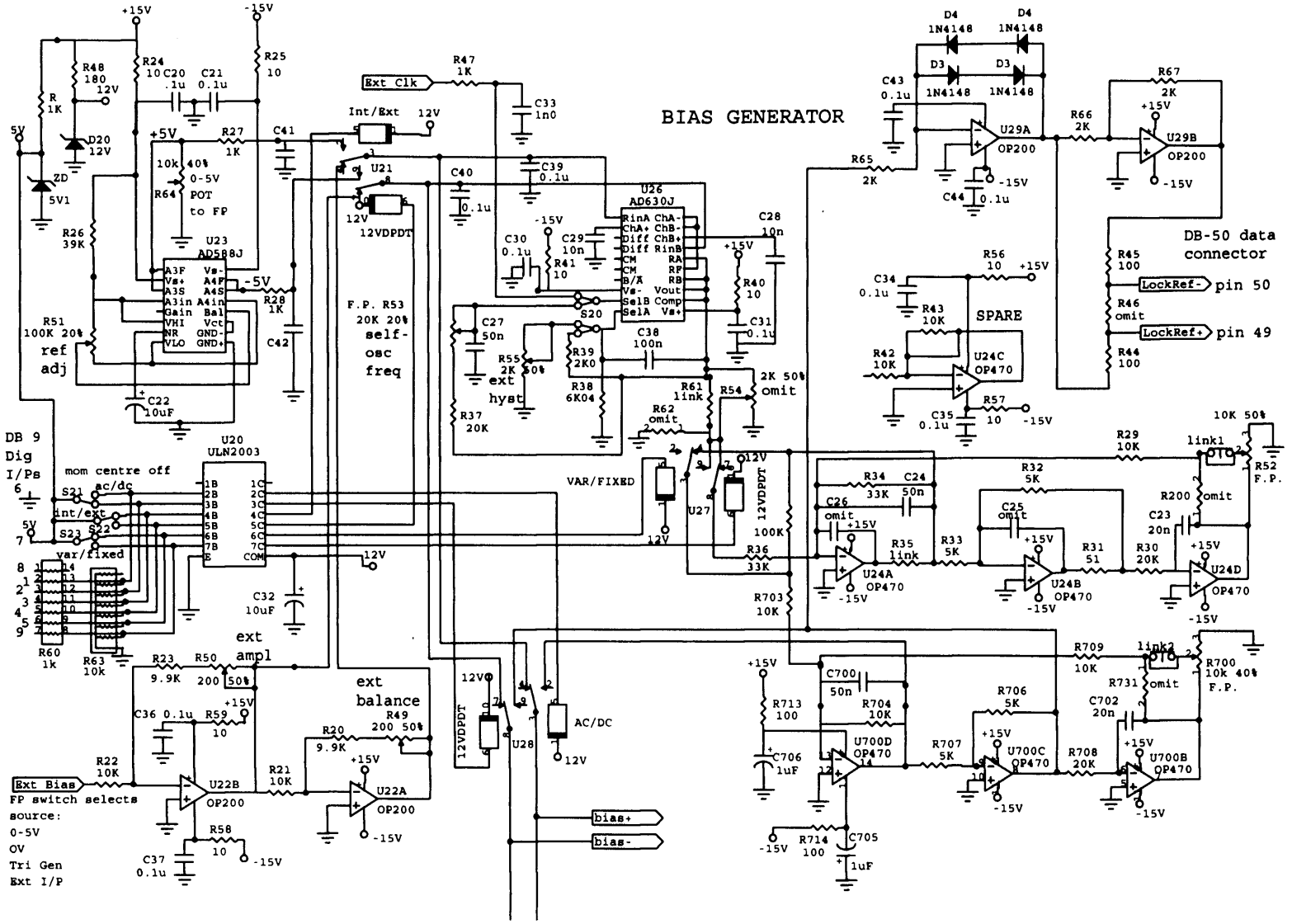
BIAS GENERATOR
+15V
-15V
+5V
5V
R48 180 12V
R24 10
C20 .1u
C21 0.1u
R25 10
R 1K
D20 12V
ZD 5V1
R27 1K
C41
10k 40% R64 POT 0-5V to FP
R26 39K
U23 AD588J
A3F Vs- A4F
Vs+ A4S
A3S A4in
A3in Bal
Gain Vct
VHI GND-
NR GND+
VLO
-5V
R28 1K
C42
R51 100K 20% ref adj
C22 10uF
Ext Clk
R47 1K
C33 1n0
Int/Ext
12V
U21
12VDPDT
C40 0.1u
C39 0.1u
F.P. R53 20K 20% self-osc freq
U26 AD630J
RinA ChA-
ChA+ ChB-
Diff ChB+
Diff RinB
CM RA
CM RF
B/R RB
Vs- Vout
SelB Comp
SelA Vs+
C30 0.1u
C29 10n
R41 10
C28 10n
R40 10
C31 0.1u
S20
C27 50n
R55 2K 50% ext hyst
R39 2K0
C38 100n
R38 6K04
R37 20K
R61 link
R54
2K 50% omit
R62 omit
VAR/FIXED
U27
12VDPDT
100K
R36 33K
R703 10K
D4 1N4148
D3 1N4148
C43 0.1u
U29A OP200
R65 2K
C44 0.1u
R66 2K
R67 2K
U29B OP200
DB-50 data connector
R45 100
LockRef- pin 50
R46 omit
LockRef+ pin 49
R44 100
R56 10
C34 0.1u
R43 10K
SPARE
R42 10K
U24C OP470
R57 10
C35 0.1u
R29 10K
link1
10K 50%
R52 F.P.
R32 5K
R34 33K
C24 50n
C26 omit
C25 omit
R200 omit
C23 20n
U24A OP470
R35 link
R33 5K
U24B OP470
R31 51
R30 20K
U24D OP470
DB 9 Dig I/Ps
mom centre off
ac/dc
int/ext
var/fixed
S21
S22
S23
U20 ULN2003
1B 1C
2B 2C
3B 3C
4B 4C
5B 5C
6B 6C
7B 7C
E COM
C32 10uF
R60 1k
R63 10k
ext ampl
R23 9.9K
R50 200 50%
C36 0.1u
R59 10
R22 10K
Ext Bias
FP switch selects source:
0-5V
OV
Tri Gen
Ext I/P
U22B OP200
R58 10
C37 0.1u
R21 10K
ext balance
R49 200 50%
R20 9.9K
U22A OP200
12VDPDT
U28
AC/DC
bias+
bias-
C700 50n
R704 10K
R713 100
C706 1uF
U700D OP470
R714 100
C705 1uF
R706 5K
R707 5K
U700C OP470
R708 20K
U700B OP470
R709 10K
link2
R731 omit
C702 20n
R700 10k 40% F.P.

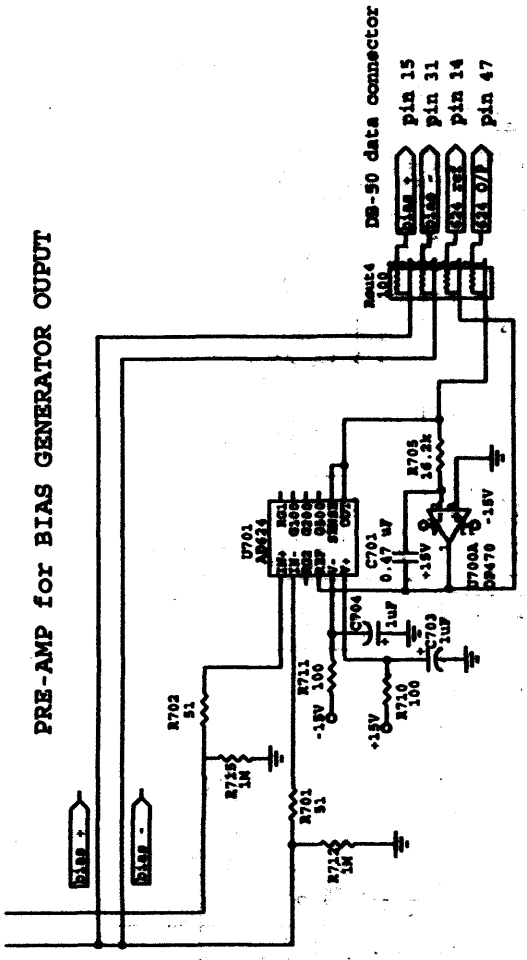
PRE-AMP for BIAS GENERATOR OUPUT
DB-50 data connector
pin 15
pin 31
pin 14
pin 47
Rnet4
U701
AM424
C701
0.47 uF
+18V
R705
10.2k
D700A
DB470
-18V
C704
1uF
C703
1uF
R711
100
-18V
R710
100
+18V
R702
51
R735
1M
R701
51
R712
1M

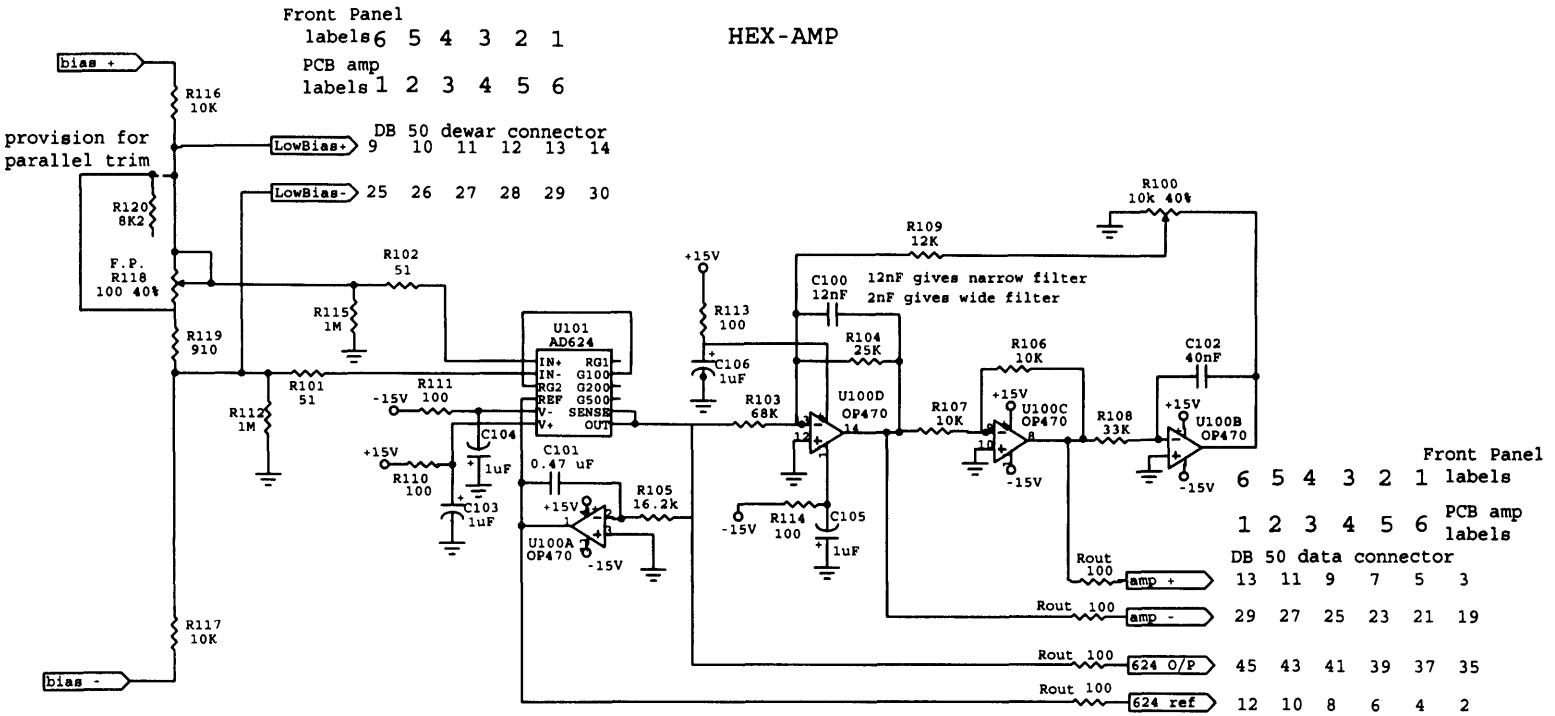
HEX-AMP
Front Panel labels 6 5 4 3 2 1
PCB amp labels 1 2 3 4 5 6
DB 50 dewar connector
9 10 11 12 13 14
25 26 27 28 29 30
bias +
bias -
provision for parallel trim
LowBias+
LowBias-
R116 10K
R117 10K
R120 8K2
F.P. R118 100 40%
R119 910
R101 51
R102 51
R111 100
R112 1M
R115 1M
R110 100
C104 1uF
C103 1uF
C101 0.47 uF
R105 16.2k
U101 AD624
IN+ RG1
IN- G100
RG2 G200
REF G500
V- SENSE
V+ OUT
U100A OP470
+15V
-15V
R113 100
C106 1uF
R103 68K
U100D OP470
R114 100
C105 1uF
C100 12nF
12nF gives narrow filter
2nF gives wide filter
R109 12K
R104 25K
R100 10k 40%
R106 10K
R107 10K
U100C OP470
R108 33K
C102 40nF
U100B OP470
Rout 100
amp +
amp -
624 O/P
624 ref
Front Panel labels 6 5 4 3 2 1
PCB amp labels 1 2 3 4 5 6
DB 50 data connector
13 11 9 7 5 3
29 27 25 23 21 19
45 43 41 39 37 35
12 10 8 6 4 2

Repeated *6

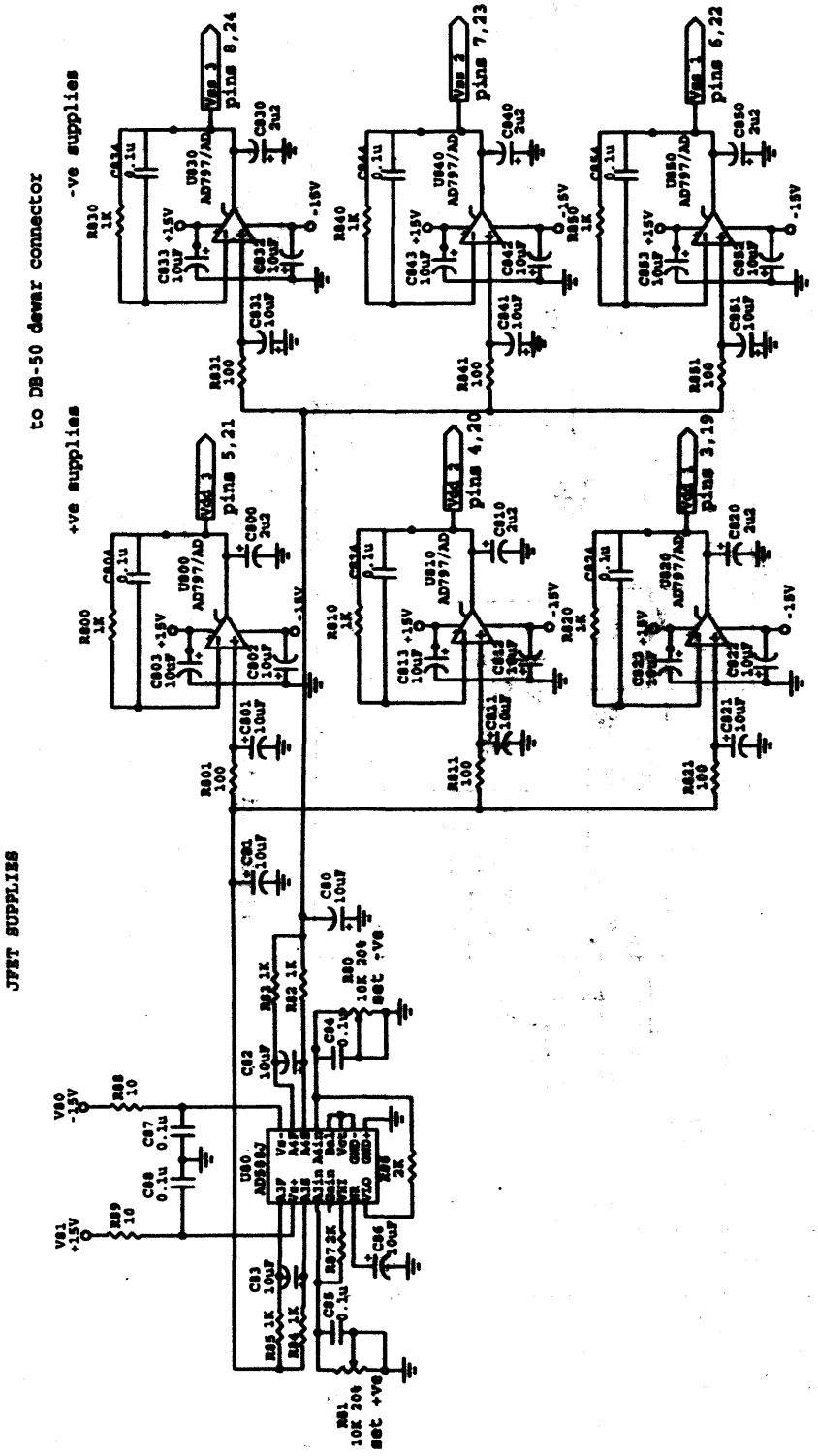
to DB-50 dewar connector
-ve supplies
+ve supplies
JFET SUPPLIES
pins 8,24
pins 7,23
pins 6,22
pins 5,21
pins 4,20
pins 3,19
AD797/AD
10K 20t
set +VG

REGULATORS

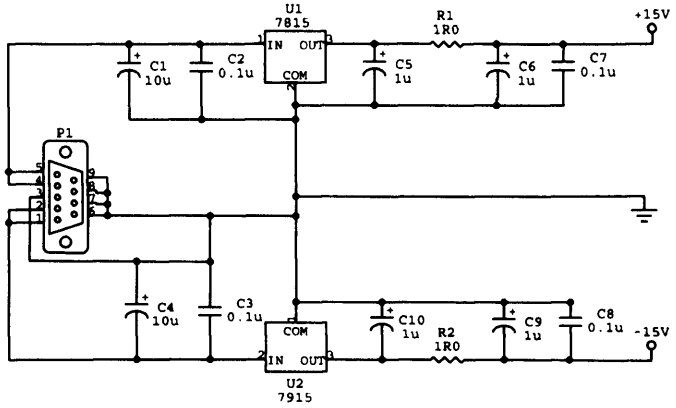

TRIANGLE WAVE
BIAS TEST GENERATOR

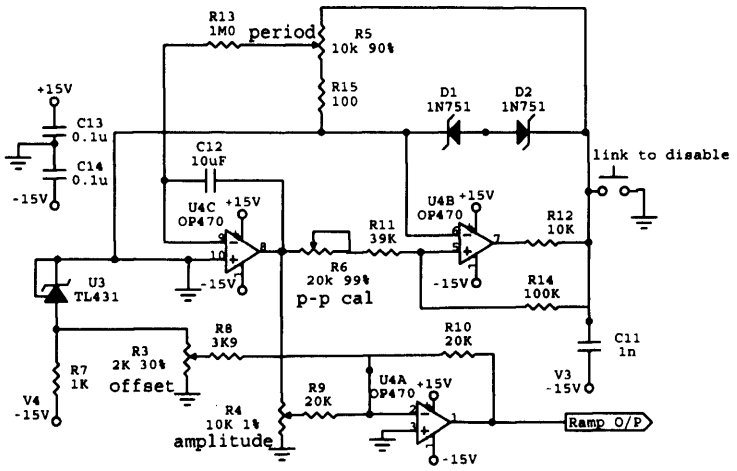

BIBLIOGRAPHY

[1] Angiola Orlando. *Optimisation and Realization of Bolometric Detectors for High Sensitivity Measurements of the Cosmic Microwave Background.* PhD thesis, University of Rome, "La Sapienza", 2004.

[2] C.K. Chan, Pamela Clancy, and John Godden. Pulse Tube Cooler for Flight Hyperspectral Imaging. *Cryogenics*, 39(12):1007–1014, 1999.

[3] Tim J. Phillips. High Performance Thermal Imaging Technology. *III-Vs Review*, 15(7):32–34, Sep 2002.

[4] J.B. Johnson. Thermal Agitation of Electricity in Conductors. *Phyiscal Review*, 32:97–109, 1928.

[5] H. Nyquist. Thermal Agitation of Electric Charge in Conductors. *Physical Review*, 32:110–113, 1928.

[6] R.G. Ross, D.L. Johnson, Collins S.A., K. Green, and H. Wickman. AIRS PFM Pule Tube Cooler System-Level Performance. *Cryocoolers*, 10, 1999.

[7] D. Ward-Thompson, R. Evans, S.J. Leeks, R.J. Walker, P.A.R. Ade, Griffin M.J., and Gear W.K. Thumper: A Two Hundred Micron Photometer. *JCMT Newsletter*, 18, 2002.

[8] R.S. Bhatia, S.T. Chase, S.M. Edgington, J.G. Glenn, W.C. Jones, A.E. Lange, B. Maffei, A.K. Mainzer, P.D. Mauskopf, B.J. Philhour, and B.K. Rownd. A Three-Stage Helium Sorption Refrigerator for Cooling of Infrared Detectors to 280 mK. *Cryogenics*, 40(11):685–691, 2000.

[9] J.G. Weisend II, editor. *Handbook of Cryogenic Engineering*, chapter 2, 7, 9. Taylor and Francis, London, 1998.

[10] M.T. Sprackling. *Thermal Physics.* American Institute of Physics, New York, 1991.

[11] P.V.E. McClintock. *Cryogenics.* Reinhold, New York, 1964.

[12] P.V.E. McClintock, D.J. Meredith, and J.K. Wigmore. *Matter at Low Temperatures.* Blackie, Glasgow, 1984.

[13] W.E. Gifford and R.C. Longsworth. Pulse-Tube Refrigeration. *J. Eng. Ind. - Trans. ASME*, (63):264–268, 1964.

[14] W.E. Gifford and R.C. Longsworth. Surface Heat Pumping. In *Advances in Cryogenic Engineering*, volume 11, pages 171–179. Plenum Press, New York, 1966.

[15] E.I. Mikulin, A.A. Tarasov, and M.P. Shkrebyonock. Low Temperature Expansion Pulse Tubes. In *Advances in Cryogenic Engineering*, volume 29, pages 629–637. Plenum Press, New York, 1984.

[16] P Kittel. Ideal Orifice Pulse Tube Refrigerator Performance. *Cryogenics*, 32, 1992.

[17] R Radebaugh. Pulse Tube Cryocoolers for Cooling Infrared Sensors. In *Infrared Technology and Applications XXVI. Edited by Bjørn F. Andresen, Gabor F. Fulop, Marija Strojnik. Proceedings of SPIE Vol. 4130*, pages 363–379, 2000.

[18] R. Radebaugh. A Review of Pulse Tube Refrigeration. In *Advances in Cryogenic Engineering.*, volume 35B - Proceedings of the 1989 Cryogenic Engineering Conference, Los Angeles, CA, July 24-28, 1989, pages 1191–1205, 1990.

[19] Shaowei Zhu, Peiyi Wu, and Zhongqi Chen. Double Inlet Pulse Tube Refrigerators: An Important Improvement. *Cryogenics*, 30:514–520, 1990.

[20] Shaowei Zhu, Peiyi Wu, and Zhongqi Chen. A Single Stage Double Inlet Pulse Tube Refrigerator Capable of Reaching 42 k. *Cryogenics*, 30:257–261, 1990.

[21] Jong Hoon Baik. *Design Methods in Active Valve Pulse Tube Refrigerator.* PhD thesis, University of Wisconsin, 2003.

[22] R. Radebaugh. Development of the Pulse Tube Refrigerator as an Efficient and Reliable Cryocooler. In *Proc. Inst. of Refrigeration*, Hall Medal Lecture, London, 1999. Institute of Refrigeration.

[23] O.V. Lounasmaa. *Experimental Principles and Methods Below 1K.* Academic Press, London, 1974.

[24] Frank Pobell. *Matter and Methods at Low Temperatures.* Springer-Verlag, Berlin and Heidelberg, 1996.

[25] Guy K. White and Philip J. Meeson. *Experimental Techniques in Low-Temperature Physics.* Oxford University Press, fourth edition, 2002.

[26] P.W. Atkins. *Atkins' Physical Chemistry.* Oxford University Press, Oxford, 7th edition, 2002.

[27] L. Duband. A Thermal Switch for Use at Liquid Helium Temperature in Spaceborne Cryogenic Systems. In R.G. Ross Jr., editor, *Proceedings of the 8th International Cryocooler Conference*, volume 8 of *Cryocoolers*, pages 731–741, New York, 1995. Plenum Press.

[28] R.C. Jones. The General Theory of Bolometer Performance. *Journal of the Optical Society of America*, 43(1):1–14, 1953.

[29] John C. Mather. Bolometer Noise: Nonequilibrium Theory. *Applied Optics*, 21(6):1125–1129, 1982.

[30] M.J. Griffin and W.S. Holland. The Influence of Background Power on the Performance of an Ideal Bolometer. *International Journal of Infrared and Millimeter Waves*, 9(10):861–875, 1988.

[31] P.L. Richards. Bolometers for Infrared and Millimeter Waves. *Journal of Applied Physics*, 76(1):1–24, 1994.

[32] M. Yun, J.W. Beeman, R. Bhatia, J.J. Bock, W. Holmes, L. Hustead, T. Koch, J.L. Mulder, A.E. Lange, A.D. Turner, and L. Wild. Bolometric Detectors for the Planck Surveyor. In *Millimeter and Submillimeter Detectors for Astronomy. Edited by Phillips, Thomas G.; Zmuidzinas, Jonas. Proceedings of the SPIE, Volume 4855*, pages 136–147, February 2003.

[33] R.V. Sudiwala, M.J. Griffin, and A.L. Woodcraft. Thermal Modelling and Characterisation of Semiconductor Bolometers. *International Journal of Infrared and Millimeter Waves*, 23:545–573, 2002.

[34] A.L. Woodcraft, R.V. Sudiwala, M.J. Griffin, E. Wakui, B. Maffei, C.E. Tucker, C.V. Haynes, F. Gannaway, P.A.R Ade, J.J. Bock, A.D. Turner, S. Sethuraman, and J.W. Beeman. High Precision Characterisation of Semiconductor Bolometers. *International Journal of Infrared and Millimeter Waves*, 23:575–595, 2002.

[35] D.A Naylor, B.G. Gom, P.A.R. Ade, and J.E. Davis. "design and performance of a dual polarizing detector system for broadband astronomical spectroscopy at submillimeter wavelengths". *Review of Scientific Instruments*, 70(10):4097–4109, 1999.

[36] M.D. Audley, W.S. Holland, W.D. Duncan, D. Atkinson, M. Cliffe, M. Ellis, X. Gao, D.C. Gostick, T. Hodson, D. Kelly, M.J. Macintosh, H. McGregor, T. Peacocke, I. Robson, I. Smith, K.D. Irwin, G.C. Hilton, J.N. Ullom, A. Walton, C. Dunare, W. Parkes, P.A.R. Ade, D. Bintley, F. Gannaway, M. Griffin, G. Pisano, R. V. Sudiwala, I. Walker, A. Woodcraft, M. Fich, M. Halpern, G. Mitchell, D. Naylor, and P. Bastien. SCUBA-2: A large-format TES array for submillimetre astronomy. *Nuclear Instruments and Methods in Physics Research A*, 520:479–482, 2004.

[37] Philippe Rossinot. *Experimental Techniques for the Study of the CMB Anisotropy and Polarisation, and the Sunyaev-Zel'dovich Effect.* PhD thesis, Cardiff University, 2004.

[38] Anthony Kent. *Experimental Low-Temperature Physics.* Macmillan Press Ltd., 1993.

[39] Ravinder Singh Bhatia. *The Effects of Closed Cycle Coolers on Infrared Detectors for Space Missions.* PhD thesis, Queen Mary and Westfield College, University of London, 1997.

[40] R.S. Bhatia, J.J. Bock, P.A.R. Ade, A. Benoît, T.W. Bradshaw, B.P. Crill, M.J. Griffin, I.D. Hepburn, V.V. Hristov, A.E. Lange, P.V. Mason, A.G. Murray, A.H. Orlowska, and A.D. Turner. The Susceptibility of Incoherent Detector Systems to Cryocooler Microphonics. *Cryogenics*, 39:701–715, 1999.

[41] R.S. Bhatia, P.A.R. Ade, T.W. Bradshaw, M.R. Crook, M.J. Griffin, and A.H. Orlowska. The Effects of Cryocooler Microphonics, EMI and Temperature Variations on Bolometric Detectors. *Cryogenics*, 41:851–863, 2002.

[42] M.J. Devlin, S.R. Dicker, J. Klein, and M.P. Supanich. A High Capacity Completely Closed-Cycle 250 mK ^{3}He Refrigeration System Based on a Pulse Tube Cooler. *Cryogenics*, 44:611–616, 2004.

[43] D.J. Haig, P.A.R. Ade, J.E. Aguirre, J.J. Bock, S.F. Edgington, M.L. Enoch, J. Glenn, A. Goldin, S. Golwala, K. Heng, G. Laurent, P.R. Maloney, P.D. Mauskopf, P. Rossinot, J. Sayers, P. Stover, and C. Tucker. Bolocam: status and observations. In C.M. Bradford, P.A.R. Ade, J.E. Aguirre, J.J. Bock, M. Dragovan, L. Duband, L. Earle, J. Glenn, H. Matsuhara, B.J. Naylor, H.T. Nguyen, M. Yun, and J. Zmuidzinas, editors, *Z-Spec: a broadband millimeter-wave grating*

spectrometer: design, construction, and first cryogenic measurements. Proceedings of the SPIE, Volume 5498, pp. 78–94 (2004)., pages 78–94, October 2004.

[44] J.J. Bock, H.M. Delcastillo, A.D. Turner, J.W. Beeman, A.E. Lange, and P.D. Mauskopf. Infrared Bolometers with Silicon Nitride Micromesh Absorbers. In E. J. Rolfe and G. Pilbratt, editors, *ESA SP-388: Submillimetre and Far-Infrared Space Instrumentation*, page 119, December 1996.

[45] A. Lee. Private communications, *APEX* telescope. 2005.